



저작자표시-비영리-변경금지 2.0 대한민국

이용자는 아래의 조건을 따르는 경우에 한하여 자유롭게

- 이 저작물을 복제, 배포, 전송, 전시, 공연 및 방송할 수 있습니다.

다음과 같은 조건을 따라야 합니다:



저작자표시. 귀하는 원저작자를 표시하여야 합니다.



비영리. 귀하는 이 저작물을 영리 목적으로 이용할 수 없습니다.



변경금지. 귀하는 이 저작물을 개작, 변형 또는 가공할 수 없습니다.

- 귀하는, 이 저작물의 재이용이나 배포의 경우, 이 저작물에 적용된 이용허락조건을 명확하게 나타내어야 합니다.
- 저작권자로부터 별도의 허가를 받으면 이러한 조건들은 적용되지 않습니다.

저작권법에 따른 이용자의 권리는 위의 내용에 의하여 영향을 받지 않습니다.

이것은 [이용허락규약\(Legal Code\)](#)을 이해하기 쉽게 요약한 것입니다.

[Disclaimer](#)

Thesis for the degree of Doctor of Philosophy

**Design of Graphene based Network in Epoxy
Polymer Nanocomposites and Their Multifunctional
Applications**

The Graduate School of the University of Ulsan

Department of Chemical Engineering

Yiming Meng

August 2022

**Design of Graphene based Network in Epoxy
Polymer Nanocomposites and Their Multifunctional
Applications**

Supervisor: Prof. Jin Suk Chung

A Dissertation

Submitted to
the Graduate School of the University of Ulsan
In Partial Fulfillment of the Requirements
for the Degree of

Doctor of Philosophy

by

Yiming Meng

Department of Chemical Engineering
University of Ulsan, Ulsan, South Korea

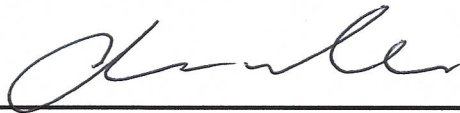
August 2022

**Design of Graphene based Network in Epoxy
Polymer Nanocomposites and Their Multifunctional
Applications**

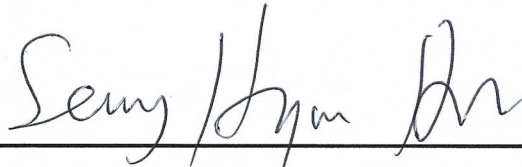
This certifies that the dissertation
of **Yiming Meng** is approved



Committee Chairman Prof. Won Mook Choi



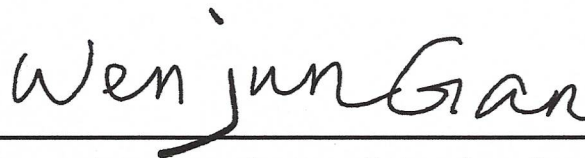
Committee Member Prof. Jin Suk Chung



Committee Member Prof. Seung Hyun Hur



Committee Member Prof. Sung Gu Kang



Committee Member Prof. Wenjun Gan

Department of Chemical Engineering

University of Ulsan, Korea

August 2022

*This Thesis is dedicated to my thesis
supervisor, mentor, role model, family, and
friends*

ACKNOWLEDGEMENTS

First and foremost, I am grateful to the University of Ulsan for accepting me and providing me with sufficient resources and opportunities to complete my Ph.D. My deepest gratitude is first to my supervisor *Prof. Jin Suk Chung*. I was fortunate to be tutored throughout by his availability, as he helped me in research, broadened my horizons, and provided financial support.

Second, I would like to thank my committee members including *Prof. Won Mook Choi*, *Prof. Seung Hyun Hur*, *Prof. Sung Gu Kang*, and *Prof. Wenjun Gan* for taking time out of their busy schedules to serve on my committee, review my dissertation and provide valuable comments and suggestions on the work. I would especially thank all my lab members including *Dr. Sushant Sharma*, *Dr. Yuanyuan Li*, *Dr. Chatchai Rodwihook*, *Thanh Truong Dang*, *Dr. Kanagaraj Naveen*, *Dr. Mahima Khandelwal*, *Dr. Aniruddha Molla*, and lab members in Shanghai for their direct or indirect support to my research.

Moreover, my sincere thanks go to *Prof. Wenjun Gan* and *Prof. Weizhen Li* for their support and help during my study at the Shanghai University of Engineering Science. They share their research experience, provide experimental equipment for me, and give warm hospitality and valuable suggestions to me. They provide me with a wonderful research environment where I study and grow up for their tireless instructions that exert a deep influence on my future life. Besides, *Prof. Wenjun Gan* give me the possible suggestions, motivations, and advice for research with extraordinary patience and consistent encouragement.

Finally, I deeply appreciate my beloved parents, my father *Prof. Yongbiao Meng* and my mother *Ms. Zhijuan Wu*, for their encouragement, understanding, and endless love during my life. They are not only my life mentors for my whole life but also always support, encourage, and help me to build strong self-confidence and accompany me to overcome the difficulties. Even though the period I study in Korea, they also provide me with the biggest warmth of family and the best conditions for my future life. At the same time, they always advise me to treat every experience as a treasure in my life and wish me to be a worthy person who can contribute to the field of expertise.

Last but not least, this dissertation is not a destination of my career. I am convinced that nothing can weaken my resolve to carry out my study. Although attempts do not always guarantee success, one's attitude might influence the course of events, I will keep striving hard to get more opportunities for success.

ABSTRACT

In this dissertation, the contents were involved five chapters that discussed the design and analysis of graphene based network (HRGO, RGO, and RFG-AlNWs) nanofillers in epoxy polymer nanocomposites, as well as their multifunctional applications such as electrical conductivity, thermomechanical properties, and electromagnetic interference shielding application, etc.

Firstly, epoxy resins owing to their high versatility from chemical and processing perspectives and hence their capability of being tailored for required properties that are used in a wide range of applications. However, the usage of electronic, electrical equipment and electronic packaging are still less. In this work, the structure of diglycidyl ether of bisphenol A (DGEBA) has a few drawbacks that lead to brittle failure, low impact resistance, and poor conductivity, which limit extensive application of DGEBA epoxy resin in various engineering applications. Modifier-polyetherimide (PEI) and graphene based nanofillers are incorporated to enhance the properties and energy dissipation mechanisms of the pristine DGEBA. These modifications result in appreciable improvement in the multifunctional DGEBA nanocomposites.

Secondly, this work discussed the selective localization of nanofillers by different interfacial tension in polyblends, the effectiveness of curing reaction-induced phase separation (CRIPS) in the polyblend, and the interface and interphase in the polyblends. Meanwhile, the simple self-assembly processing technology to incorporate graphene based network nanofillers in DGEBA/PEI by controlling its localization, the synergistic effect between nanofillers and the DGEBA/PEI polyblend and the technique of characterization have also been discussed.

Thirdly, this work focused on a feasible and effective approach to building an electrically conductive and double percolation network-like structure via incorporating highly reduced graphene oxide (HRGO) into DGEBA/PEI polyblend. The evolution of the phase structure of DGEBA/PEI/HRGO nanocomposites was investigated by varying content of PEI. The 0.5wt.% HRGO delivered a high electrical conductivity in DGEBA/PEI polyblends, wherein the value increased from 5.03×10^{-16} S/m (neat DGEBA) to 5.88 S/m (DP30H). Due to selective localization behavior, an interconnected network of HRGO is formed in the phase-separated

structure of the DGEBA/PEI polyblend using the CRIPS technique.

Then, the research focused on optimizing and analysis of DGEBA/PEI/RGO in various content of RGO. The selective interfacial localization of RGO was predicted numerically by the harmonic and geometric mean technique and further confirmed by field emission transmission electron microscopy (FETEM) analysis. Due to selective interfacial localization, the electrical conductivity was increased to 366 S/m with 3 wt.% RGO reinforcement (DP30R3). The thermomechanical properties of nanocomposites were determined by dynamic mechanical analysis (DMA). The storage modulus of 3 wt.% RGO-reinforced polyblend (DP30R3) exhibited an improvement of ~15%, and glass transition temperature (T_g) was 10.1 °C higher over neat DGEBA. Furthermore, the total shielding effectiveness (SET) was increased to 25.8 dB in the X-band region, with only 3 wt.% RGO, which represents ~99.9% shielding efficiency.

Furthermore, the research concentrated on fabricating an efficiently reduced hexylamine functionalized graphene oxide/ Aluminium nanowires (RFG-AINWs) conductive network nanofiller in the DGEBA/PEI polyblend system. The Al nanowires were synthesized on the hexylamine functionalized graphene oxide substrate by a simple high temperature treatment process without any catalyst. Meanwhile, the morphology, electrical, thermal, and EMI shielding properties of RFG-AINWs and its nanocomposites, as well as the selective localization of hybrid RFG-AINWs nanofiller in the DGEBA/PEI, were discussed.

Finally, the above results showed the graphene based network nanofillers (HRGO, RGO, and RFG-AINWs) in DGEBA/PEI nanocomposites might have great potential in various applications, such as electronic coatings, EMI shielding, aerospace structural materials, and microelectronics

TABLE OF CONTENTS

ACKNOWLEDGEMENTS	I
ABSTRACT	II
TABLE OF CONTENTS	IV
LIST OF FIGURES	VIII
LIST OF TABLES	XII
CHAPTER 1 INTRODUCTION	- 1 -
1.1. Development of Epoxy Based Composites.....	- 1 -
1.2. Polymer Blend Composites System.....	- 2 -
1.2.1. <i>Background and perspectives</i>	- 2 -
1.2.2. <i>The matrix and modifier</i>	- 5 -
1.2.3. <i>Curing reaction-induced phase separation (CRIPS)</i>	- 5 -
1.2.4. <i>Curing agent</i>	- 6 -
1.2.5. <i>Thermosetting-thermoplastic polyblend</i>	- 7 -
1.2.6. <i>The nanofiller</i>	- 9 -
REFERENCES	- 13 -
CHAPTER 2 BACKGROUND OF STUDY	- 18 -
2.1. The Interface and Interphase in the Polyblend.....	- 18 -
2.2. The Intrinsic Versus Extrinsic Interface/Interphase	- 19 -
2.3. The Role of the Interface/Interphase in Dispersion of Nanofillers	- 20 -
2.4. The Synergistic Effect of Ternary Polyblend Composites System	- 23 -
2.5. Techniques of Characterization.....	- 25 -
2.5.1. <i>Contact angle measurement</i>	- 25 -
2.5.2. <i>Thermogravimetric analysis (TGA)</i>	- 27 -
2.5.3. <i>Differential scanning calorimeter (DSC)</i>	- 28 -
2.5.4. <i>Dynamic mechanical analysis (DMA)</i>	- 29 -

2.5.5.	<i>Fourier Transform Infrared Spectroscopy (FT-IR)</i>	- 32 -
2.5.6.	<i>Four-point probe technique</i>	- 32 -
2.5.7.	<i>Electromagnetic interference (EMI) shielding</i>	- 34 -
2.5.8.	<i>X-ray photoelectron spectroscopy (XPS)</i>	- 36 -
REFERENCES		- 41 -
CHAPTER 3 OPTIMIZING AND ANALYSIS OF GRAPHENE BASED NETWORK		
NANOFILLER AT DIFFERENT CONTENT OF DGEBA/PEI POLYBLENDS		
- 45 -		
3.1.	Introduction.....	- 45 -
3.2.	Experimental Section.....	- 48 -
3.2.1.	<i>Synthesis of Highly Reduced Graphene Oxide (HRGO)</i>	- 48 -
3.2.2.	<i>Preparation of DGEBA/PEI/HRGO Composites</i>	- 48 -
3.2.3.	<i>Measurement and Characterization</i>	- 49 -
3.3.	Results and Discussion.....	- 51 -
3.3.1.	<i>Physical and Morphological Properties of HRGO</i>	- 51 -
3.3.2.	<i>Morphology of DGEBA/PEI/HRGO as Observed by Optical Microscopy (OM)</i> <i>Measurement</i>	- 53 -
3.3.3.	<i>Field Emission Transmission Electron Microscopy (FETEM) Analyses</i>	- 56 -
3.3.4.	<i>Electrical Properties of Nanocomposites</i>	- 57 -
3.3.5.	<i>Prediction for Selective Localization of HRGO</i>	- 59 -
3.3.6.	<i>Mechanism of HRGO Localization</i>	- 62 -
3.3.7.	<i>Dynamic Mechanical Analyses (DMA)</i>	- 63 -
3.4.	Conclusions.....	- 67 -
REFERENCES		- 67 -
CHAPTER 4 ENHANCED EMI SHIELDING AND ELECTRICAL CONDUCTIVITY		
PROPERTIES IN DGEBA/PEI/RGO TERNARY SYSTEM		
- 74 -		
4.1.	Introduction.....	- 74 -
4.2.	Experimental section.....	- 76 -

4.2.1. <i>Synthesis of RGO</i>	- 76 -
4.2.2. <i>Fabrication of DGEBA/RGO/PEI nanocomposites</i>	- 76 -
4.2.3. <i>Measurement and characterization</i>	- 77 -
4.3. Results and discussion	- 79 -
4.3.1. <i>Morphological properties of RGO</i>	- 79 -
4.3.2. <i>Physical and chemical properties of RGO</i>	- 79 -
4.3.3. <i>Morphologies and chemical properties of DGEBA/PEI/RGO nanocomposites</i>	- 82 -
4.3.4. <i>Prediction for selective localization of RGO</i>	- 84 -
4.3.5. <i>Electrical properties of nanocomposites</i>	- 86 -
4.3.6. <i>Thermal and thermomechanical properties of nanocomposites</i>	- 88 -
4.3.7. <i>EMI shielding properties of nanocomposites</i>	- 92 -
4.4. Mechanism.....	- 94 -
4.5. Conclusions.....	- 96 -
REFERENCES	- 97 -
 CHAPTER 5 CONSTRUCTION OF ONE-STEP, ALUMINIUM NANOWIRES ON HEXYLAMINE FUNCTIONALIZED GRAPHENE TEMPLATE CONDUCTIVE NETWORK IN DGEBA/PEI NANOCOMPOSITES	
5.1. Introduction.....	- 106 -
5.2. Experimental section.....	- 106 -
5.2.1. <i>Synthesis of RFG-AlNWs film</i>	- 106 -
5.2.2. <i>Fabrication of DGEBA/PEI/RFG-AlNWs nanocomposites</i>	- 107 -
5.2.3. <i>Measurement and characterization</i>	- 107 -
5.3. Results and discussion	- 108 -
5.3.1. <i>Morphological properties of RFG-AlNWs</i>	- 108 -
5.3.2. <i>Physical properties of RFG-AlNWs</i>	- 110 -
5.4. Future work.....	- 111 -
REFERENCES	- 111 -

SUMMARY AND FUTURE WORK.....- 114 -
LIST OF PUBLICATIONS.....- 116 -

LIST OF FIGURES

Figure 1.1. Polyblend phase diagram	- 4 -
Figure 1.2. The illustration of the chemical structure of DGEBA and PEI.	- 5 -
Figure 1.3. The illustration of chemical structures of Me-THPA, DMBA, and the cured DGEBA.	- 7 -
Figure 1.4. Penetration of small molecules in polymer interfaces, filling the voids space and causing the swelling phenomenon.....	- 8 -
Figure 1.5. The illustration of (a) initial step from a monomer, (b) stage of oligomers formation, (c) step of polymerization (reaching the gel point), and (d) vitrification stage (cure).	- 9 -
Figure 1.6. Illustration of the Current Preparation Methods for Graphene and Graphene-Related Materials[20]......	- 11 -
Figure 2.1. (a) The dielectric constant of barium titanate as a function of size [2],(b) The interfacial volume (for an interphase thickness of 10 nm) as a function of particle size assuming individual filler dispersion. (c) Nanocomposite transmittance as a function of particle size and particle index of refraction.	- 20 -
Figure 2.2. (a) Examples of the types of extrinsic interphase that can be added to the nanofiller surface to control both nanofiller dispersion and add functionality to the composite [10], (b) A schematic of the kinds of changes that can be observed in the intrinsic interphase including changes in crystalline morphology, crosslink density, and density or chain conformation.....	- 21 -
Figure 2.3 (a) The impact of interface volume as a measure of dispersion on glass transition temperature [11], (b) The impact of dispersion as measured via a skewness in the distribution of nanofillers on dielectric breakdown strength [12]......	- 21 -
Figure 2.4. The illustration of (a) a drop liquid on a solid substrate with the surface tension and contact angle and (b) an instrument of contact angle measurement (Phoenix 300, SEO Co.).	- 25 -
Figure 2.5. TGA instrument (Q50, TA Instruments, USA).....	- 28 -
Figure 2.6. The structure of (a) DSC measuring cell (heat-flow principle) disk tester system, (b)Tzero™ sensor, and (c) DSC instrument (Q20 V24.10, TA Instruments Co., USA).....	- 29 -
Figure 2.7. DMA instrument (DMA (Q800, TA Instruments, USA).....	- 31 -

Figure 2.8. (a) Configuration diagram of an FT-IR spectroscope and (b) FT-IR instrument (Nicolet™ iS™ 5, Thermo Fisher Scientific Inc., USA).	- 32 -
Figure 2.9. Schematic diagram of (a) A.I.T four-point probe system and (b) a four-point probe circuit.....	- 33 -
Figure 2.10. Equivalent circuit diagram of a four-point probe, showing the wire resistances (RW), contact resistances (RC), and sample resistances (RS). The green arrows represent current flow. -	34 -
Figure 2.11. (a) SE measurement setup of samples (b) schematic illustration of the scattering parameters from a two-port VNA[42], and (c) The vector network analyzer (E5071C Agilent Inc.).	- 36 -
Figure 2.12. Components of an XPS system. Reproduced with permission from Thermo Fisher Scientific.	- 37 -
Figure 2.13. Depth of surface chemical analysis techniques.....	- 37 -
Figure 2.14. Processes that result from x-ray bombardment of a surface include (a) emission of a photoelectron, (b) x-ray fluorescence, and (c) emission of an Auger electron.....	- 38 -
Figure 2.15. Energy level diagram illustrates schematically the basic XPS equation, including the x-ray source energy ($h\nu$), the binding energy of the electron (BE), the measured kinetic energy of the electron (KE_{measured}), and the work function of the spectrometer ($\Phi_{\text{spectrometer}}$).....	- 39 -
Figure 2.16. Schematic diagrams show the major components of an (a) XPS instrument and (b) monochromator.	- 40 -
Figure 3.1. Schematic illustration of preparation of DGEBA/PEI/HRGO polyblend nanocomposites and the phase structure during the process.	- 51 -
Figure 3.2. (a) SEM micrograph of HRGO flakes after drying, (b) TEM micrograph of HRGO and (c) Raman spectra of GO and HRGO flakes.	- 52 -
Figure 3.3. The FTIR spectra for HRGO and GO.	- 53 -
Figure 3.4. The final phase morphologies of DGEBA/PEI/HRGO nanocomposites are (a) DP5H, (b) DP10H, (c) DP15H, (d) DP20H, (e) DP25H, (f) DP30H, and (g) DP30, respectively.	- 55 -
Figure 3.5. FETEM micrographs of (a–c) DP25H polyblend from lower to higher magnification	

with inset in (c) represents HRTEM micrograph of localized HRGO at the interface of DGEBA and PEI, and (d–f) represents DP30H polyblend with phase inversion. - 57 -

Figure 3.6. The electrical properties of samples for various PEI contents: (a) DGEBA/PEI, (b) DGEBA/PEI/0.5 wt.% HRGO. - 58 -

Figure 3.7. The contact angle images of samples are given in Table 3.5. (a) DI on DGEBA, (b) DI on PEI, (c) DI on HRGO, (d) GL on DGEBA, (e) GL on PEI, (f) GL on HRGO, (g) FA on DGEBA, (h) FA on PEI, (i) FA on HRGO. - 60 -

Figure 3.8. Schematic illustration: (a) structural evolution of double percolation conductive DGEBA/PEI/HRGO nanocomposites via CRIPS and (b) FETEM image of nanocomposite.- 63 -

Figure 3.9. The storage modulus versus temperature of DGEBA/PEI polyblend (a) at 30–230 °C and (b) a magnified view of the beginning of the transition (80–130 °C). Storage modulus versus temperature curves for DGEBA/PEI/HRGO nanocomposites with 0.5 wt.% HRGO at (c) 30–230 °C and (d) 80–130 °C. - 65 -

Figure 3.10. Tan δ versus temperature curve for DGEBA/PEI polyblend: (a) 30–230 °C, (b) 100–150 °C for T_{g1} , (c) 150–230 °C for T_{g2} , and tan δ versus temperature curve for DGEBA/PEI/HRGO nanocomposites: (d) 30–230 °C, (e) 100–150 °C for T_{g1} , (f) 150–230 °C for T_{g2} - 66 -

Figure 3.11. The differential scanning calorimeter (DSC) curves of (a) DGEBA/PEI polyblends and (b) DGEBA/PEI/HRGO polyblends. - 67 -

Figure 4.1. Schematic of the fabrication of DGEBA/PEI/RGO nanocomposites. - 77 -

Figure 4.2. SEM micrographs of pristine GO at (a) low and (b) high magnification, (c) TEM micrograph of GO, SEM micrographs of RGO flakes at (d) low and (e) high magnification, (f) TEM micrograph of RGO. - 79 -

Figure 4.3. (a) Raman and (b) FT-IR spectra of RGO flakes and GO. (c) Wide-scan, and (d) C 1s high-resolution core-level of XPS spectra for GO and RGO flakes. - 80 -

Figure 4.4. XPS spectra of RGO flakes of N 1s high-resolution core-level. - 82 -

Figure 4.5. The FETEM micrographs of the DP25R3 nanocomposite at (a) lower and (b) higher magnification, (c) HRTEM micrograph of RGO in DP25R3, (d–e) DP30R3 nanocomposite with inversion morphology, and (f) HRTEM micrograph of RGO in DP30R3. - 82 -

Figure 4.6. FETEM images of (a) DP30 in low magnification and the histogram of the relative frequency verse the PEI thickness to exhibit the PEI thickness distribution in the figure(inset), (b) DP30 in high magnification in which the dark domains are PEI-rich phases and bright domains are DGEBA-rich phases, respectively.	- 83 -
Figure 4.7. The FT-IR spectra of DR3, DP30, DP30R3, and neat DGEBA.....	- 84 -
Figure 4.8. The contact angle images of samples: (a) DI on DGEBA, (b) DI on PEI, (c) DI on RGO, (d) GL on DGEBA, (e) GL on PEI, (f) GL on RGO, (g) FA on DGEBA, (h) FA on PEI, (i) FA on RGO.....	- 85 -
Figure 4.9. The volume resistivity and volume conductivity of (a) DR_{n_2} and (b) $DP30R_{n_2}$ nanocomposites with varying RGO content.....	- 87 -
Figure 4.10. The TGA spectra of (a) GO and RGO, and (b) neat DGEBA, DR3, DP5R3, DP25R3, and DP30R3 under N_2 atmosphere.....	- 90 -
Figure 4.11. The DSC curves of (a) DR_{n_2} and (b) $DP30R_{n_2}$. The DMA measurements of (c) storage modulus and (d) $\tan \delta$ of the nanocomposites as a function of temperature.....	- 91 -
Figure 4.12. The EMI shielding effectiveness of DR3, DP25R3, and DP30R3 in the 8.2–12.4 GHz frequency range, (a) SE_T , (b) SE_A , (c) SE_R , and (d) the average SE_T , SE_A , and SE_R in the X band.	- 93 -
Figure 4.13. Schematic of (a) morphological evolution of double percolation, conductive $DP_{n_1}R_{n_2}$ nanocomposites and (b) the EMI shielding mechanism of $DP_{n_1}R_{n_2}$ nanocomposites. ...	- 96 -
Figure 5.1. Schematic of the fabrication of DGEBA/PEI/RFG-AlNWs nanocomposites. ...	- 107 -
Figure 5.2 SEM micrographs of FG/Al micro-particles at (a) low and (b) high magnification, SEM micrographs of RFG-AlNWs at (c) low and (d) high magnification.	- 109 -
Figure 5.3. OM micrographs of (a) GO, (b) FG-Al (c) RFG-AlNWs, and (d) DGEBA/RFG-AlNWs.....	- 110 -
Figure 5.4. FT-IR spectra of samples	- 111 -

LIST OF TABLES

Table 2.1. Interaction laws for different particles	- 22 -
Table 3.1. Formulation of samples.	- 49 -
Table 3.2. The volume resistivity and volume conductivity of DGEBA/PEI polyblend with and without HRGO.	- 58 -
Table 3.3. Comparison of electrical properties with those of previously publications.	- 59 -
Table 3.4. Surface tensions and components (mJ/m^2).	- 59 -
Table 3.5. Surface tension components and parameters and static contact angles for the test liquids DGEBA, PEI, and HRGO.	- 60 -
Table 3.6. The surface tension parameters were obtained from Table 3.5.....	- 61 -
Table 3.7. The wetting coefficient (ω_a), interfacial tension (γ_{pair}), and predicted localization of HRGO in DGEBA/PEI/HRGO polyblends.....	- 62 -
Table 3.8. The storage, rubbery modulus, and T_g (from $\tan \delta$) of samples.	- 66 -
Table 4.1. Formulation of samples.	- 77 -
Table 4.2. The γ_{pair} and ω_a were obtained by different methods.	- 86 -
Table 4.3. Comparison of electrical properties of previously published filler ternary polyblend systems with those of the systems in the current work.	- 87 -
Table 4.4. The TGA spectra of samples under N_2 atmosphere.	- 89 -
Table 4.5. The glass transition temperature T_g (taken as the intersection of the extrapolation of baseline with the extrapolation of the inflexion) of samples.....	- 90 -
Table 4.6. The storage modulus and T_g of various samples.....	- 91 -
Table 4.7. Comparison of EMI shielding performance with other composites.	- 94 -

CHAPTER 1 Introduction

In this chapter, the introduction of epoxy based multifunctional nanocomposites, fabrication of thermosetting-thermoplastic nanostructured blends, curing reaction-induced phase separation (CRIPS), and research technique of characterization, where the thermosetting polymer is the matrix, will be discussed. The issues of CRIPS and morphology shall be treated together with the properties of the blends and conclusions will be drawn.

1.1. Development of Epoxy Based Composites

The epoxy resins as one of the thermosetting polymers own unique properties for structural application and are widely used in adhesives, matrices of composites, and electronic encapsulating materials. However, these materials are inherent of brittle and low impact resistance due to their high crosslinking density structure, a great effort has been made to improve the fracture toughness. A widely used method for this purpose is the addition of second-phase polymeric modifiers to form a fine phase-separated morphology, these polymeric modifiers can be either elastomers or thermoplastics. Generally, the modified thermosets are prepared from a homogenous solution composed of the precursors of thermosets and the modifiers and reaction-induced demixing occurs during the curing reaction. Over the past decades, great success has been achieved in this area. This chapter provides a comprehensive overview of the development in thermoplastic-toughened epoxy. First, we review the history of thermoplastic-toughened epoxy, Then, we summarize the factors affecting the toughening effect and mechanisms accounting for thermoplastic-toughened epoxy. Finally, we discuss some new trends in this field. Polymer-based nanocomposites have been extensively investigated as multifunctional and high-performance materials and their applications have been widely extended due to their tailored properties including damping capacity, thermal conductivity, flame retardancy, electrical conductivity and so forth [1-4].

With the addition of nanofillers, structural characteristics and fundamental physics involved can be distinguished from traditional polymer composites [5]. One significant difference is the predominant influence of interfaces in nanocomposites on the overall material properties. As interfaces become more spatially extensive and complex with reducing filler size[6],

characterizing and designing interfaces in nanocomposites have become a requisite for further optimizing materials performance. The preparation of rigid nanofiller foam which can withstand the hydrodynamic forces of resin infusion is not an easy task and further practical applicability for complex geometries is very difficult. Hence, a simple processing technology to develop epoxy resin-based effective EMI shielding materials with low loading of conducting nanofiller is extremely important.

1.2.Polymer Blend Composites System

1.2.1.Background and perspectives

Polymer blend (polyblend) is a mixture of at least two polymers or copolymers. Polyblends are physical mixtures of two or more polymers with or without any chemical bonding between them. Polymer blending is the process of mixing two or more different polymers to form a new class of material with different physical properties [7]. Polymer blending technology also provides attractive opportunities for reuse and recycling of polymer wastes. The various economic and property advantages accomplished by blending are:

The opportunity to develop or improve on properties to meet specific customer needs.

- The capability to reduce material cost with or without little sacrifice in properties.
- Permit the much more rapid development of modified polymeric materials to meet emerging needs by by-passing the polymerization step.
- Extended service temperature range.
- Light weight.
- The ability to improve the processability of materials which are otherwise limited in their ability to be transformed into finished products.
- Increased toughening.
- Enhanced ozone resistance.
- Improvement modulus and hardness.
- Improved barrier property and flame retardant property.
- Improved impact and environmental stress cracking resistance,etc.

The gradual depletion of economic ways of developing new monomers led to the development

of polymer blending, also because newly developed monomers gave increase to polymers with intermediate properties as compared with individual polymers [8].

Homologous Polyblend

This type of blend is a mixture of two or more fractions of the same polymer, each of which has a different molar mass distribution. Any polydispersed polymer is a homologous polyblend. These blends are miscible because of the closeness of molar mass distribution.

Miscible Polyblend

Miscible blends are homogeneous to the molecular level. For this type of blend, Gibbs free energy of mixing, $\Delta G_m \approx \Delta H_m \leq 0$ where ΔH_m is the enthalpy of mixing; and this is due to specific interactions. Homogeneity is observed at least on a nanometer scale, if not on the molecular level. This type of blends exhibits only one glass transition temperature (T_g), which is in between the glass transition temperatures of the blend components in a close relation to the blend composition. Due to their high molar mass, the entropy of mixing of polymers is relatively low and, consequently, specific interactions are needed to obtain blends, which are miscible or homogeneous on a molecular scale. Most thermoset/thermoset blends are miscible over a very wide temperature range and in all compositions [9, 10].

Immiscible Polyblend

Immiscible polyblends are phase separated with:

$$\Delta G_m \approx \Delta H_m \geq 0 \quad (1.1)$$

where ΔG_m is the Gibb's free energy and ΔH_m is the enthalpy heat of mixing.

The overall physico-mechanical behavior depends critically on two demanding structural parameters. The first one is a proper interfacial tension leading to a phase size small enough to allow the material to be considered as macroscopically homogeneous and an interphase adhesion strong enough to assimilate stresses. The other is strains without disruption of the established morphology. Fully immiscible blends have a coarse morphology, sharp interface, and poor adhesion between the blend phases. These kinds of blends show a two-phase morphology, so they are of no use without compatibilization. When blends are incompatible, the properties of the blend are inferior to those of pure polymers. However, most pairs of high-molecular-weight polymers

are immiscible or incompatible. Polymer-polymer miscibility depends on a variety of independent variables which include composition, molecular weight, temperature, and pressure. Components, which resist gross phase segregation and show desirable blend properties, are considered to have a good compatibility, even though they are immiscible in a thermodynamic sense. These blends will exhibit different T_{gs} corresponding to the T_g of the component polymers. Examples of fully immiscible blends are PA/ABS, PA/PPO, PA/EPDM, and PA/PP. Now these blends have become commercially successful, after being efficiently compatibilized using suitable compatibilizers (Figure 1.1).

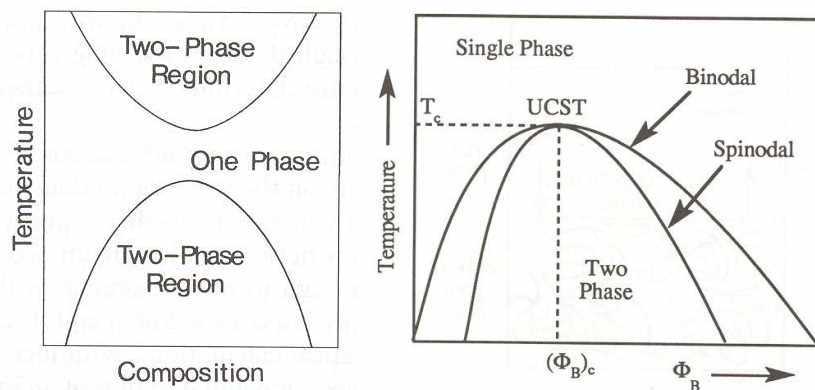


Figure 1.1. Polyblend phase diagram

Compatible Polyblend

In this type, a small part of one of the blend component is dissolved in the other part, so the blend exhibits fine phase morphology and satisfactory properties. Both blend phases are homogeneous and have their own T_g . Both T_g are shifted from the values for the pure blend components toward the T_g of the blend component. An example is the PC/ABS blends. In these blends, PC and the SAN phase of ABS partially dissolve in one another. In this case interface is wide and the interfacial adhesion is good.

Polymer Alloy

These are immiscible polyblends with modified interface. Although they are heterogeneous in nature, their properties and morphologies are controlled by compatibilization. Dawson [11] described the composition of a polymer alloy he patented in 1991 which was a blend of PP, ethylene copolymer ionomer resin, ethylene/glycidyl acrylate, or methacrylate copolymer. The polymer alloy was claimed to be useful in applications where a wide range of temperatures and

abrasive conditions are encountered. Another example is Neoloy which composed of polyolefin and thermoplastic engineering polymer developed specifically for use in high-strength geosynthetics.

1.2.2. The matrix and modifier

The epoxy oligomer used as the matrix was diglycidyl ether of bisphenol A, Dow 332 (epoxy equivalent 171-175 g/eq), and the modifier was chosen by polyetherimide (PEI, Ultem®1000, $T_g \approx 217 \text{ }^\circ\text{C}$) in this research.

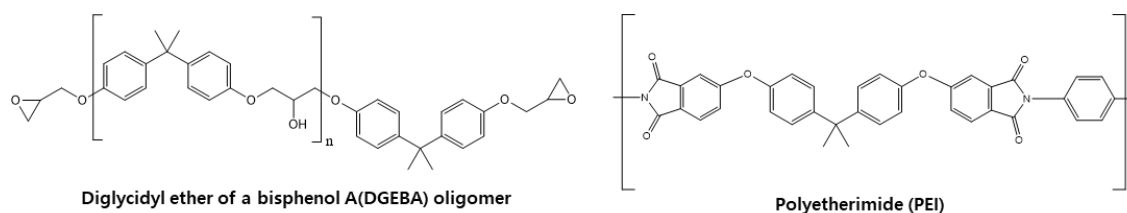


Figure 1.2. The illustration of the chemical structure of DGEBA and PEI.

1.2.3. Curing reaction-induced phase separation (CRIPS)

Many epoxy formulations include a particular modifier, such as a rubber, a thermoplastic, a liquid crystal, a foaming agent, and so on, that is miscible before reaction but becomes phase separated during polymerization (CRIPS). The origin of phase separation is the increase in the average molar mass of the reacting system during the pre-gel stage and the increase in crosslink density during the post-gel stage. An increase in molar mass produces a decrease in the contribution of the entropy of mixing while, after gelation, the presence of a cross-linked network generates an elastic contribution that limits the amount of modifier in the swollen network.

The CRIPS is employed to produce different morphologies in the final products that are appropriate to increase toughness (e.g., thermoplastic polymer-modified epoxies), to generate an optical response induced by an electric field (polymer-dispersed liquid crystals), or to produce a porous material (foam) after elimination of the phase-separated modifier. By varying the initial concentration of modifier and the reaction temperature (or the thermal cycle) a variety of morphologies may be developed in the final material. Conditions are usually selected to produce appropriate morphologies for the desired application but balancing a possible deleterious effect on other mechanical or thermal properties. A typical example of this balance is the case of thermoplastic polymer-modified epoxies. Thermoplastic polymer addition increases toughness

but decreases the elastic modulus and the glass transition temperature of the final product (through the fraction of rubber remaining dissolved in the epoxy matrix). The amount of rubber is selected to obtain a convenient balance of thermal and mechanical properties.

1.2.4.Curing agent

Epoxy curing agents, also referred as hardeners, play a crucial role in the final characteristics of the cured material. Indeed, all the characteristics that are strictly related to the cross-linking density of the polymeric network, such as hardness, chemical resistance, heat resistance, flexibility, and brittleness, can be controlled by the hardener. Curing agents can react either with the epoxy groups or the hydroxyl side groups. Curing agents cross-link epoxy resins either by a catalytic mechanism or by bridging across epoxy molecules. Some curing agents may involve both the catalytic and cross-linking mechanisms. Common classes of hardeners for epoxy resins include amines, acid anhydrides, phenols, and thiols. For details about different curing agents, the reader is referred to other reviews. In terms of reactivity, these can be ranked as phenol < anhydride < aromatic amine < cycloaliphatic amine < aliphatic amine < thiol. The most popular choices are amines and acid anhydrides[12].

Amines

Amines are an important class of curing agents. Aliphatic, cycloaliphatic, or aromatic amines can be used, which are mainly selected according to the application. In general, the order of reactivity is aliphatic amines > cycloaliphatic amines > aromatic amines. Lower reactivity allows longer working times for processors. Thermal stability of the cured resin also increases in the same order; aromatic amines form much more rigid structures than aliphatic amines, hence more thermally stable and/or less flammable materials. The primarily aliphatic amines provide fast-curing hardeners for use at room temperatures. Amines though are skin irritants.

Acid anhydrides

These are less skin irritant than amines and less reactive, hence the cure exotherm is lower[12]. Some examples include phthalic, hexahydrophthalic, chlorendic, and maleic anhydrides. Other cross-linkers of interest are amides (e.g., polyamides), and complexes of boron trifluoride and amines, such as monoethylamine. Phenols, such as novolacs, which have already been discussed

above under resin systems, also act as curing agents. Thiols, also known as mercaptans, contain a sulfur atom, which reacts very readily with the epoxide group owing to its nucleophilicity, even at room temperature. Owing to their very high reactivity, thiols are used where fast cure is required, for example, for domestic DIY adhesives. The epoxy curing reaction may be accelerated by addition of small quantities of accelerators: tertiary amines, carboxylic acids, and phenols (e.g., bisphenol A) are effective accelerators.

We used methyl tetrahydrophthalic anhydride (Me-THPA) as the curing agent and N,N-dimethylbenzylamine (DMBA) as the accelerator shown in Figure 1.3.

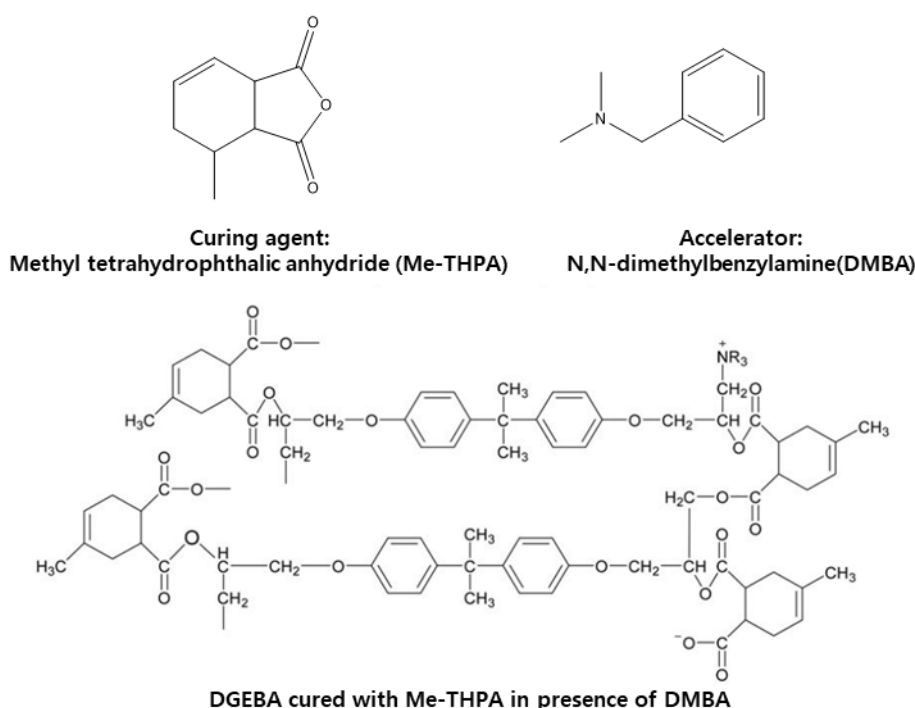


Figure 1.3. The illustration of chemical structures of Me-THPA, DMBA, and the cured DGEBA.

1.2.5. Thermosetting-thermoplastic polyblend

The thermoset polymers are those that after they have been cured by a chemical reaction, do not melt with increasing temperature, it means that once they are produced, they cannot be reprocessed or deformed, which makes recycling difficult. A continuous temperature rise in these polymers leads to degradation of the material. This can be easily understood when we visualize the primary chemical bonds (covalent) present between the chains. These connections require a high amount of energy to rupture, usually causing the breaking of the bonds of the polymer, leading to degradation of the polymer. Furthermore, these thermosetting polymers are usually

insoluble in most common solvents, since they cannot to break the cross-links present between chains. What happens when the solvent is chemically compatible with the polymer is a phenomenon known as swelling, where the polymer absorbs the solvent molecules. This process can occur by penetration of small molecules in the polymeric interfaces, filling the voids space or by changing the spatial arrangement of the polymer chains resulting in the compound mass and volume increase (Figure 1.6). The degree of swelling is proportional to the matrix and solvent affinity and the number of cross-links between the polymer chains. It should be in mind that the amount of crosslinking is inversely proportional to the degree of swelling [13].

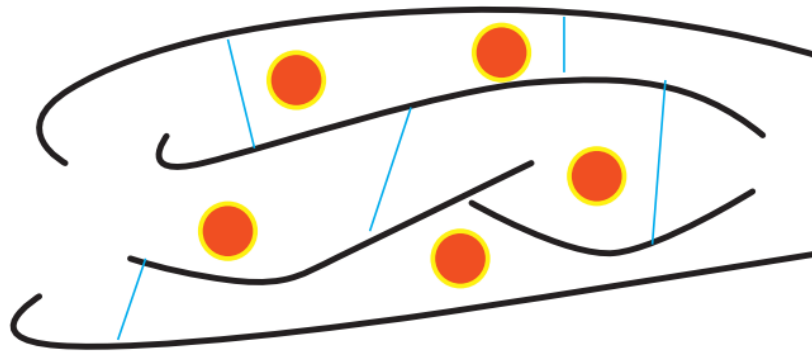


Figure 1.4. Penetration of small molecules in polymer interfaces, filling the voids space and causing the swelling phenomenon.

The process of hardening the thermosetting polymer or the curing process, as it is commonly known, is often complex and may involve several steps, as we shall see later; however, unlike thermoplastics, the curing reaction is involved in obtaining the final piece to be used. Several factors can influence the quality of the final piece obtained. They were molds with good stability during the temperature changes of the curing process, as well as cure speed and cure time, which are key parameters for obtaining good-quality and low-cost composites. The curing process can be divided into four parts as follow:

- (1) In the first stage the resin, in solid or liquid state, has a low degree of conversion. In this step, when necessary, curing agents, catalysts and/or fillers are added to the process. This process begins, usually by thermal activation, light or radiation. From then on, it becomes more fluid (Figure 1.5a)
- (2) The subsequent step involves the formation of oligomers with the linear polymer preparation,

having a low molecular weight (Figure 1.5b).

- (3) With the rise of the temperature, networks are formed in a stage where there is a three-dimensional evolution. This change is a reflection of molecular mass increase, the appearance of gelled structures and entanglements between polymer chains (Figure 1.5c).
- (4) Subsequently, the formation of cross-links (11-50% of total links) between adjacent chains occurs with a consequent increase of molecular mass (Figure 1.5d).

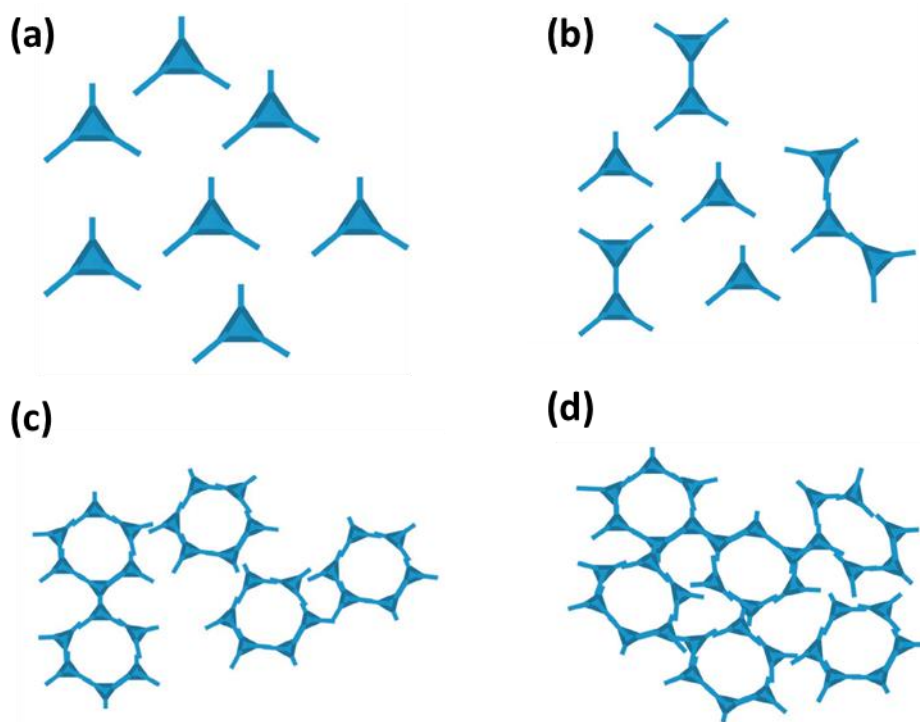


Figure 1.5. The illustration of (a) initial step from a monomer, (b) stage of oligomers formation, (c) step of polymerization (reaching the gel point), and (d) vitrification stage (cure).

When cure is complete, the primary chemical bonds (covalent) present between the chains which restrict the rotational and vibrational motions. To be broken, these links require a high amount of energy, resulting usually with the polymeric chain bonds breaking with subsequent degradation.

1.2.6. The nanofiller

Graphene is an allotrope of carbon that has sp^2 hybridization forming planar structure. Each layer of planar structure of carbon is called graphene and these graphene sheets are connected with each other by Van der Waals force of attraction known as graphite. Graphene is also known as “wonder material” as it shows several exceptional properties due to high current density,

ballistic transport, chemical inertness, high thermal conductivity, optical transmittance, and super hydrophobicity at nanometer scale [14]. The monoatomic single layer of graphene which has the sp^2 hybridized C atom provides great importance in developing several material properties critically far higher than similar conventional materials. The 2p orbitals of C atom form the π state bands that delocalize all over the single layer sheet of individual graphene. It is the reason why graphene exhibits exceptionally high strength like Young's modulus ~ 1100 GPa, fracture strength ~ 125 GPa, excellent electrical conductivity ~ 106 S/cm, thermal conductivity ~ 5000 W/m K, very high charge mobility of nearly $200,000$ $\text{cm}^2/\text{V s}$, nearly zero effective mass, impermeable to several gases, optically transparent, and a very large specific area of ~ 2630 m^2/g as per a theoretical calculation [15-17].

Owing to graphene's high electrical, thermal, and mechanical properties, it can be used as the nanofiller for the development of high-performance epoxy matrix based nanocomposites and hold potential for a variety of possible applications [18, 19]. Due to the high electric conductivity and mechanical flexibility, it can find the substitution of metal conductors. The nanofillers can be dispersed into polymers using techniques such as solution mixing, melt blending, or in situ polymerization. In these methods, in situ polymerization might offer superior dispersion of nanofiller. Graphene has these outstanding properties due to its high aspect ratio and single thin layer. It is known that graphene agglomerates due to its high surface area when coming in contact with the polymer. Therefore, for the reduction of this agglomeration functionalization of graphene is required which can be performed by oxidizing or by reducing agents.

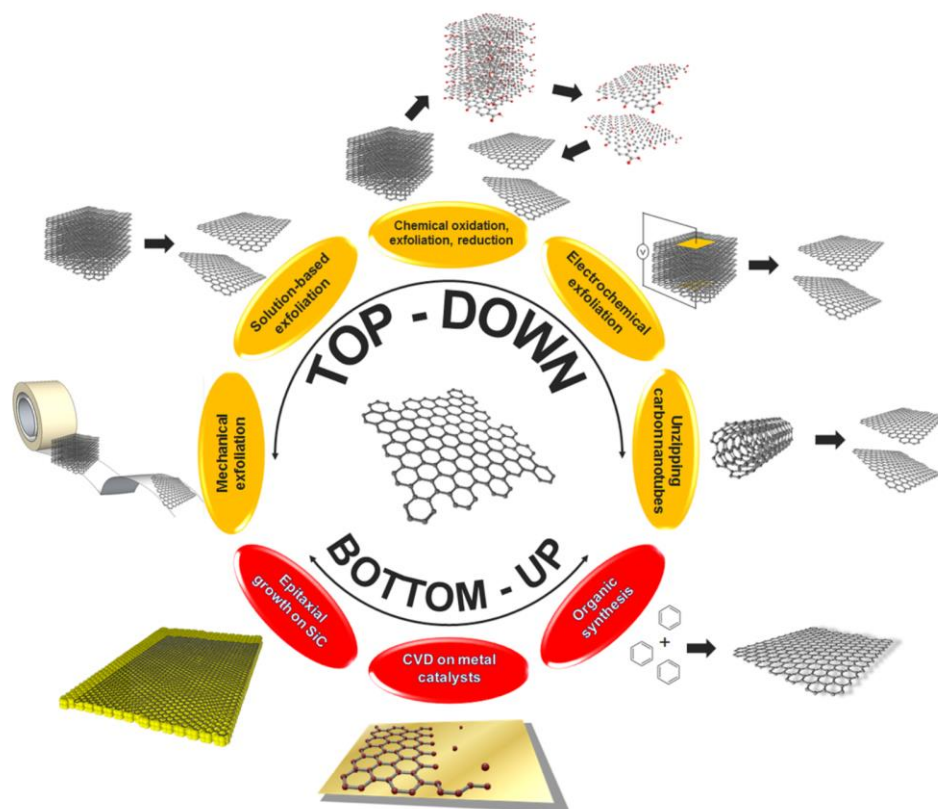


Figure 1.6. Illustration of the Current Preparation Methods for Graphene and Graphene-Related Materials[20].

1.2.6.1. Graphene

There are now four primary ways to produce ‘pristine’ graphene as follow:

- (a) Epitaxial graphene. This method involves chemical vapor deposition (CVD) growth on epitaxially matched metal surfaces[21-24]. In this technique graphene is fabricated by graphite target or catalytic decomposition of hydrocarbon on the surface of metal catalyst. In this, the metal debris is very low that is the major advantage of this technique [25]. This fabrication is best for the preparation of single- layer graphene and can also be used for heteroatoms doped graphene nanostructure in which graphene can be doped with sulphur, nitrogen, phosphorus, fluorine, or bromine, etc. which will improve the catalytic activity enzymatic application, energy conversion [26].
- (b) Micromechanical Exfoliation. Ruoff and coauthors laid the foundation for micromechanical exfoliation as well as outlined the potential importance for graphene for a wide variety of fundamental studies and applications, in several papers published in 1999[27, 28]. In this method, the graphene is to be peeled from the bulk of graphite

layer by layer. To overcome the resistance offered by the Van der Waal attraction in between the adjacent flakes of graphene. There are two paths for mechanical exfoliation one is normal and the other one is lateral force. In normal force the Van der Waal force can be overcome by Scotch tape [29, 30]. Graphite has ability of self-lubricating in lateral direction so lateral force can also use to for peeling the two layers of graphene

- (c) Exfoliation of graphite in solvents. Obtaining dispersions of GO to yield individual layers of graphene oxide (i.e., colloidal dispersions) is to make dispersions of graphite in various solvents [31].
- (d) Other methods. Substrate-free gas-phase synthesis of graphene platelets in a microwave plasma reactor [32] and arc discharge synthesis of multi-layered graphene [33] have also recently been reported.

1.2.6.2. Graphene oxide (GO)

Comprehensive reviews on the preparation of dispersions of graphene oxide platelets and reduced graphene oxide platelets, made from GO, have recently appeared [34, 35]. In general, GO is synthesized by either the Brodie [36], Staudenmaier [37], or Hummers method [38], or some variation of these methods. All three methods involve oxidation of graphite to various levels. Brodie and Staudenmaier used a combination of potassium chlorate (KClO_3) with nitric acid (HNO_3) to oxidize graphite, and the Hummers method involves treatment of graphite with potassium permanganate (KMnO_4) and sulfuric acid (H_2SO_4).

The polar oxygen functional groups of GO render it hydrophilic; GO can be exfoliated in many solvents and disperses particularly well in water [39]. Dispersions of graphene oxide platelets can be obtained by stirring and more typically by sonication of GO in solvents; chemical reduction of the colloidal dispersions obtained has been performed with several reducing agents, such as them hydrazine [40], hydroquinone [41], sodium borohydride (NaBH_4), [42, 43] and ascorbic acid [44]. Reduction via thermal treatment [45, 46] has been reported to be an efficient and low cost method, producing themally-expanded GO material with a BET surface area of 600–900 m^2/g . Electrochemical reduction has been presented as an effective way to remove oxygen functional groups from GO [47].

1.2.6.3.Reduced graphene oxide (RGO)

RGO is the reduced form of GO in which different oxygen groups are reduced. Different approaches have been used for the reduction process like chemical reduction, thermal reduction, microwave-assisted reduction, solvothermal reduction, and photo-reduction. GO is reduced to enhance the honeycomb hexagonal lattice which has been distorted due to the oxidation of graphene and the electric properties enhanced [48, 49]. GO is an insulator but after reduction, the conductivity can be increased. Several agents have been reported which can reduce GO chemically which are hydrazine, sodium borohydride, alcohol, hydroxides, metals, redox active sulfur species, reductive acids, or even enzymatic reduction.

Another fabricating method of RGO is thermal reduction of GO. In this method, GO can be heated in different atmosphere like Argon (Ar), hydrogen (H₂), Ammonia (NH₃), and high vacuum or different heating methods like electric heating, heated AFM tip, laser heating, plasma heating, etc. [48]. RGO obtained by heating has high electrical conductivity. Although the reduction level of RGO can be controlled by duration, atmosphere of gas and heating temperature. GO can also be reduced thermally at the temperature of 1000 °C, while researchers have also opted for the less temperature process.

1.2.6.4.RGO/metallic nanowires

Metallic nanowires synthesized on RGO automatically form a conductive composite with an extremely high conductivity [50, 51]. Compared with the most widely used nanowires, such as Ag and Si nanowires, Al nanowires are highly electronically conductive, extremely low in cost, and resistant to harsh environments due to the naturally compacted oxide layer on the surface. Such an architecture matches the need of designing advanced electronic devices[52], but it is challenging for current scalable synthesis methods as carbon is not a typical catalyst material. Therefore, a facile and scalable synthesis strategy for Al nanowires and advanced structures is highly desired to broaden the applications of Al nanowires.

References

[1] Han Z, Fina A. Thermal conductivity of carbon nanotubes and their polymer nanocomposites: A review. *Progress in Polymer Science*. 2011;36:914-44.

- [2] Ajayan PM, Schadler LS, Braun PV. Nanocomposite science and technology: John Wiley & Sons, 2006.
- [3] Terrones M, Martín O, González M, Pozuelo J, Serrano B, Cabanelas JC, et al. Interphases in graphene polymer - based nanocomposites: achievements and challenges. Wiley Online Library; 2011.
- [4] Thostenson ET, Chou T-W. Processing-structure-multi-functional property relationship in carbon nanotube/epoxy composites. Carbon. 2006;44:3022-9.
- [5] Koo JH. Polymer Nanocomposites: Processing, Characterization, and Applications. McGraw-Hill Education; 2006.
- [6] Nelson JK. Dielectric polymer nanocomposites: Springer, 2010.
- [7] Eitouni H, Balsara N. Physical Properties of Polymers Handbook. Springer New York; 2007.
- [8] Baker WE, Scott CE, Hu G-H, Akkapeddi M. Reactive polymer blending: Hanser Munich, 2001.
- [9] Barral L, Cano J, López J, López-Bueno I, Nogueira P, Abad M, et al. Blends of an epoxy/cycloaliphatic amine resin with poly (ether imide). Polymer. 2000;41:2657-66.
- [10] Norbert V. Characterization of thermoplastic elastomers by means of temperature scanning stress relaxation measurements. Thermoplastic elastomers Rijeka, Croatia: InTech. 2012:347-70.
- [11] Dawson RL. Thermoplastic polymer alloy composition. Google Patents; 1993.
- [12] Gilbert M. Brydson's plastics materials: William Andrew, 2016.
- [13] Fourquet_Bandeira C, Montoro SR, Brocks T. Chapter 1 - Thermoset-Thermoplastic Nanostructured Blends. In: Thomas S, Shanks R, Chandrasekharakurup S, editors. Design and Applications of Nanostructured Polymer Blends and Nanocomposite Systems. Boston: William Andrew Publishing; 2016. p. 1-13.
- [14] Chen J-H, Jang C, Xiao S, Ishigami M, Fuhrer MS. Intrinsic and extrinsic performance limits of graphene devices on SiO₂. Nature nanotechnology. 2008;3:206-9.
- [15] Pan Y, Sahoo NG, Li L. The application of graphene oxide in drug delivery. Expert Opinion on Drug Delivery. 2012;9:1365-76.
- [16] Service RF. Carbon sheets an atom thick give rise to graphene dreams. American Association

for the Advancement of Science; 2009.

[17] Sheehy DE, Schmalian J. Optical transparency of graphene as determined by the fine-structure constant. *Physical Review B*. 2009;80:193411.

[18] Sato S, Kakushima K, Ahmet P, Ohmori K, Natori K, Yamada K, et al. Structural advantages of rectangular-like channel cross-section on electrical characteristics of silicon nanowire field-effect transistors. *Microelectronics Reliability*. 2011;51:879-84.

[19] Jang BZ, Zhamu A. Processing of nanographene platelets (NGPs) and NGP nanocomposites: a review. *Journal of materials science*. 2008;43:5092-101.

[20] Ambrosi A, Chua CK, Bonanni A, Pumera M. Electrochemistry of Graphene and Related Materials. *Chemical reviews*. 2014;114:7150-88.

[21] May JW. Platinum surface LEED rings. *Surface Science*. 1969;17:267-70.

[22] Shelton J, Patil H, Blakely J. Equilibrium segregation of carbon to a nickel (111) surface: A surface phase transition. *Surface Science*. 1974;43:493-520.

[23] Eizenberg M, Blakely J. Carbon interaction with nickel surfaces: Monolayer formation and structural stability. *The Journal of Chemical Physics*. 1979;71:3467-77.

[24] Hamilton JC, Blakely JM. Carbon segregation to single crystal surfaces of Pt, Pd and Co. *Surface Science*. 1980;91:199-217.

[25] Dong Z, Jiang C, Cheng H, Zhao Y, Shi G, Jiang L, et al. Facile fabrication of light, flexible and multifunctional graphene fibers. *Advanced materials*. 2012;24:1856-61.

[26] Higginbotham AL, Lomeda JR, Morgan AB, Tour JM. Graphite oxide flame-retardant polymer nanocomposites. *ACS applied materials & interfaces*. 2009;1:2256-61.

[27] Lu X, Yu M, Huang H, Ruoff RS. Tailoring graphite with the goal of achieving single sheets. *Nanotechnology*. 1999;10:269.

[28] Lu X, Huang H, Nemchuk N, Ruoff RS. Patterning of highly oriented pyrolytic graphite by oxygen plasma etching. *Applied Physics Letters*. 1999;75:193-5.

[29] William S, Hummers J, Offeman RE. Preparation of graphitic oxide. *J Am Chem Soc*. 1958;80:1339-.

[30] Lerf A, He H, Forster M, Klinowski J. Structure of graphite oxide revisited. *The Journal of*

Physical Chemistry B. 1998;102:4477-82.

[31] Hernandez Y, Nicolosi V, Lotya M, Blighe FM, Sun Z, De S, et al. High-yield production of graphene by liquid-phase exfoliation of graphite. *Nature nanotechnology*. 2008;3:563-8.

[32] Dato A, Radmilovic V, Lee Z, Phillips J, Frenklach M. Substrate-Free Gas-Phase Synthesis of Graphene Sheets. *Nano letters*. 2008;8:2012-6.

[33] Li N, Wang Z, Zhao K, Shi Z, Gu Z, Xu S. Large scale synthesis of N-doped multi-layered graphene sheets by simple arc-discharge method. *Carbon*. 2010;48:255-9.

[34] Dreyer DR, Park S, Bielawski CW, Ruoff RS. The chemistry of graphene oxide. *Chemical Society Reviews*. 2010;39:228-40.

[35] Park S, Ruoff RS. Chemical methods for the production of graphenes. *Nature nanotechnology*. 2009;4:217-24.

[36] Brodie BC. XIII. On the atomic weight of graphite. *Philosophical transactions of the Royal Society of London*. 1859:249-59.

[37] Staudenmaier L. Verfahren zur darstellung der graphitsäure. *Berichte der deutschen chemischen Gesellschaft*. 1898;31:1481-7.

[38] Hummers Jr WS, Offeman RE. Preparation of graphitic oxide. *Journal of the american chemical society*. 1958;80:1339-.

[39] Paredes J, Villar-Rodil S, Martínez-Alonso A, Tascon J. Graphene oxide dispersions in organic solvents. *Langmuir*. 2008;24:10560-4.

[40] Stankovich S, Dikin DA, Piner RD, Kohlhaas KA, Kleinhammes A, Jia Y, et al. Synthesis of graphene-based nanosheets via chemical reduction of exfoliated graphite oxide. *Carbon*. 2007;45:1558-65.

[41] Wang G, Yang J, Park J, Gou X, Wang B, Liu H, et al. Facile synthesis and characterization of graphene nanosheets. *The Journal of Physical Chemistry C*. 2008;112:8192-5.

[42] Si Y, Samulski ET. Synthesis of water soluble graphene. *Nano letters*. 2008;8:1679-82.

[43] Shin HJ, Kim KK, Benayad A, Yoon SM, Park HK, Jung IS, et al. Efficient reduction of graphite oxide by sodium borohydride and its effect on electrical conductance. *Advanced Functional Materials*. 2009;19:1987-92.

- [44] Dua V, Surwade SP, Ammu S, Agnihotra SR, Jain S, Roberts KE, et al. All - organic vapor sensor using inkjet - printed reduced graphene oxide. *Angewandte Chemie International Edition*. 2010;49:2154-7.
- [45] McAllister MJ, Li J-L, Adamson DH, Schniepp HC, Abdala AA, Liu J, et al. Single sheet functionalized graphene by oxidation and thermal expansion of graphite. *Chemistry of materials*. 2007;19:4396-404.
- [46] Schniepp H, Li J, McAllister M, Sai H, Herrera-Alonso M, Adamson D. RK Prud homme, R. Car, DA Saville, IA Aksay. *J Phys Chem B*. 2006;110:8535.
- [47] Zhou M. J: Zhai, W. Ren, F. Wang, S. Dong. *Chem Eur J*. 2009;15:6116-20.
- [48] Mao S, Pu H, Chen J. Graphene oxide and its reduction: modeling and experimental progress. *RSC Advances*. 2012;2:2643-62.
- [49] Priyadarsini S, Mohanty S, Mukherjee S, Basu S, Mishra M. Graphene and graphene oxide as nanomaterials for medicine and biology application. *Journal of Nanostructure in Chemistry*. 2018;8:123-37.
- [50] Balandin AA. Thermal properties of graphene and nanostructured carbon materials. *Nature Materials*. 2011;10:569-81.
- [51] Fang R, He Y, Zhang K, Li H. Melting behavior of aluminum nanowires in carbon nanotubes. *The Journal of Physical Chemistry C*. 2014;118:7622-9.
- [52] Javey A, Nam S, Friedman RS, Yan H, Lieber CM. Layer-by-layer assembly of nanowires for three-dimensional, multifunctional electronics. *Nano letters*. 2007;7:773-7.

CHAPTER 2 Background of Study

In this chapter, we focus on discussing the effects of nanofiller on the morphology of immiscible polyblends and the interface and interphase in the polyblends. Interfaces remain one of the major issues in limiting the understanding and designing of polymer nanocomposites due to their complexity and pivotal role in determining the ultimate composites' properties. And the interfacial energies of fillers and polymer are a key role to estimate the wetting coefficient which is a method to predict the localization of filler in the polyblend. The synergistic effect of ternary polymer composites system also be discussed.

2.1.The Interface and Interphase in the Polyblend

Three key points make polymer nanocomposites unique:

1. As the size of a filler decreases, its properties can change including color, catalytic activity, index of refraction, dielectric constant, and surface energy[1-4]. Figure 2.1(a) shows an example of the dielectric constant of barium titanate as a function of size[2].

2. As the surface area to volume ratio changes due to decreasing filler size, the amount of interfacial area or volume of the interphase increases as $1/r$. Figure 2.2(b) shows this quantitatively for a 10 nm-thick interfacial region. This increase in interphase volume, however, is only achieved if the dispersion of the nanofiller is maintained. Agglomeration decreases the interphase volume.

3. The small size of the filler minimizes its impact as a defect compared to micron scale fillers. For example, as the filler diameter increases above ~ 25 nm (as determined by the Rayleigh scattering equation), light scattering from the fillers increases. Below ~ 25 nm the transparency of the composite can be maintained while changing other properties[5, 6] in Figure. 1(c). A second example is the observed simultaneous increases in modulus, strength, and ductility, not observed in traditional composites[7].

Thus, the ability to incorporate small-scale fillers into polymers leads to significant changes in properties due to the properties of the filler (which can be a unique function of size), the large volume of interphase (with typically unknown properties), and the ability to introduce changes in properties without introducing detrimental defects.

This chapter focuses primarily on our current understanding of the structure and properties

of the interface region and the impact of the interfacial region on both the dispersion of the fillers and the bulk properties. It is also important to note that this chapter is limited to composites for which there is a polymer matrix without the addition of small molecules. Such mediation with small molecules can lead to dramatically different and organized structures that are fascinating, but not the focus of this chapter[8].

2.2.The Intrinsic Versus Extrinsic Interface/Interphase

Two key definitions of a polymer nanocomposite interface/interphase are critical to a clear discussion. First, the interface is a two-dimensional (2D) region at the boundary between the filler and the matrix. Depending on the length scale of interest, however, there is no clear 2D boundary, and instead a three-dimensional (3D) interphase exists with properties that can vary continuously from the filler surface to some distance into the bulk matrix. For purposes of discussion, interfacial region or interphase will be used and will encompass both the 2D and 3D regions.

Second, there are both intrinsic and extrinsic interfacial regions. The intrinsic interphase develops as a result of the polymer matrix interacting with the nanofiller surface. The extrinsic interphase is the result of carefully placed molecules on the nanofiller surface. While the intrinsic interphase is strongly impacted by the nanofiller surface or extrinsic interphase, its structure and properties are only indirectly designed or tailored, while the extrinsic interphase can be designed to control dispersion, matrix/filler interaction, or local properties directly. For example, surface treatment of fillers with small molecules is often done to improve thermodynamic compatibility with the matrix and stabilize nanofiller dispersion. This addition of the small molecule is an extrinsic interphase (Figure. 2(a)). As the matrix/filler enthalpic compatibility changes, the structure and mobility of the intrinsic interphase will change due to this small molecule addition (Figure. 2(b)). This could include changes in crosslink density, crystallinity, density, and conformation. A second example is surface ligand engineering of nanofillers[9] with a range of molecules (up to molecular weight of 4100 kg/mol) that can lead excellent thermodynamic compatibility with the matrix and/or add functionality to the composite. This kind of extrinsic interphase can be extensive. But the matrix structure and properties near this extrinsic interphase are also altered forming an intrinsic interphase as well. Thus, the relative volume of the extrinsic

and intrinsic interphase can vary, but it is important to distinguish between the two.

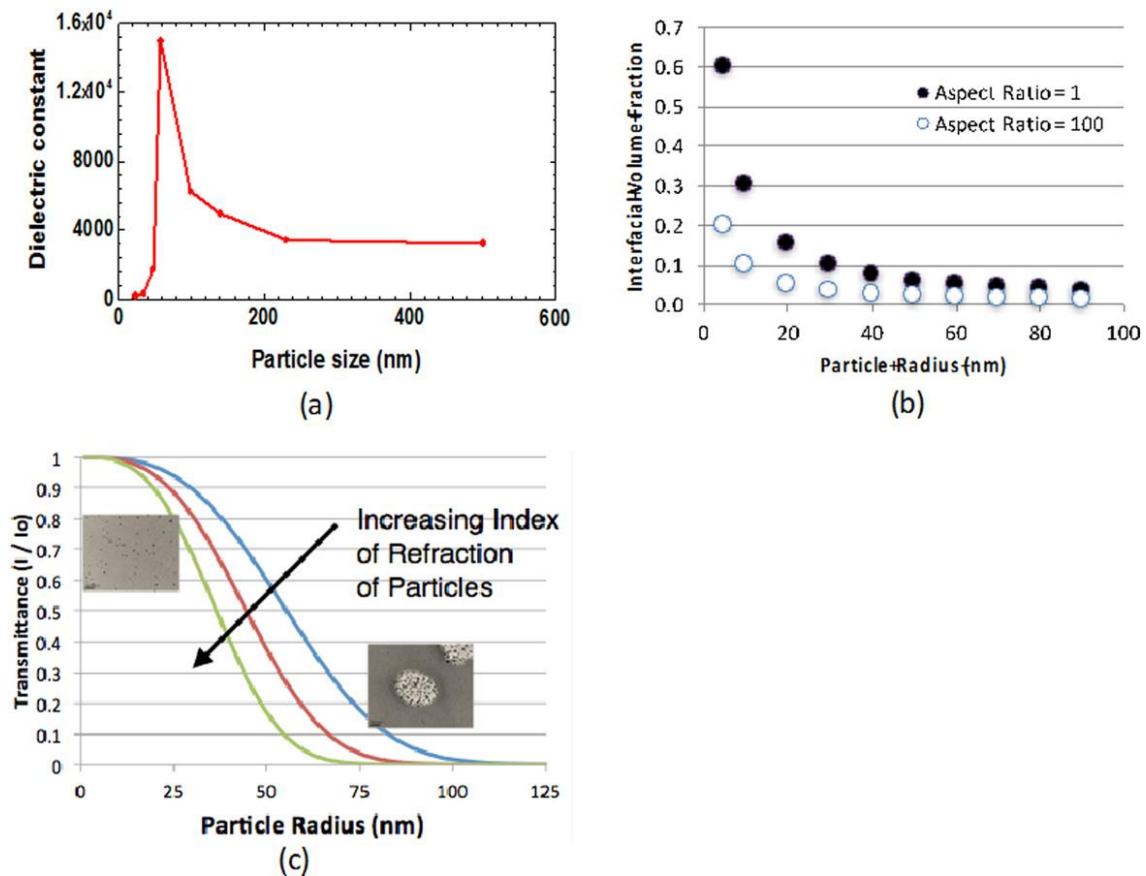


Figure 2.1. (a) The dielectric constant of barium titanate as a function of size [2], (b) The interfacial volume (for an interphase thickness of 10 nm) as a function of particle size assuming individual filler dispersion. (c) Nanocomposite transmittance as a function of particle size and particle index of refraction.

2.3. The Role of the Interface/Interphase in Dispersion of Nanofillers

In order to take advantage of the large interphase volume, it is critical to have “good” dispersion of the nanofillers. Good dispersion includes two things: separation of primary particles and homogeneous distribution of those fillers throughout the full volume of the material. As particles agglomerate, the volume of the interphase decreases linearly with cluster size. This reduction in interphase volume can impact properties, such as the glass transition temperature as shown in Figure. 3(a). The dispersion is also important because agglomerates begin to mimic micron scale fillers and thus create defects that can be detrimental to the bulk properties. Figure. 3(b) shows the impact of agglomeration (as measured by the skewness in the spatial distribution of fillers) on the dielectric breakdown strength. Even small degrees of agglomeration can dramatically change the property

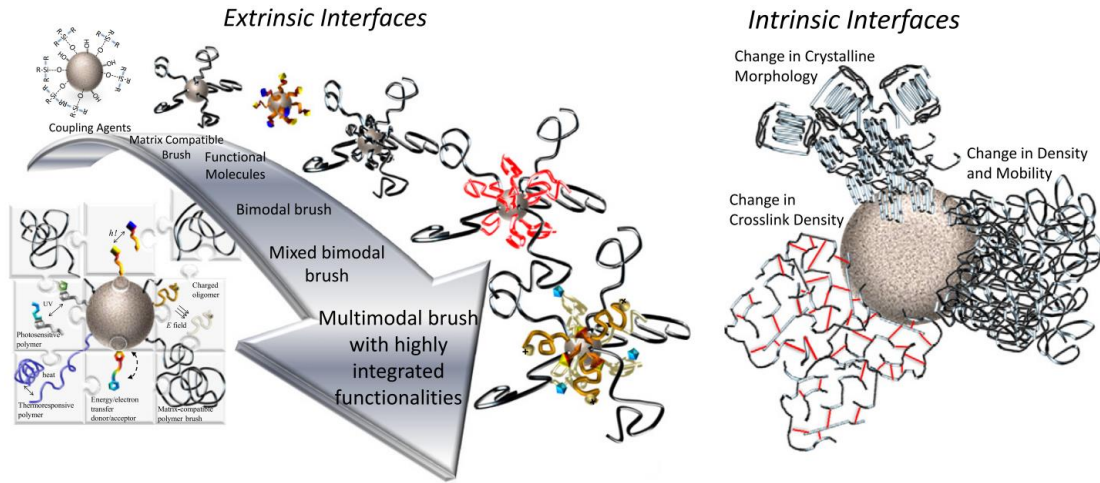


Figure 2.2. (a) Examples of the types of extrinsic interphase that can be added to the nanofiller surface to control both nanofiller dispersion and add functionality to the composite [10], (b) A schematic of the kinds of changes that can be observed in the intrinsic interphase including changes in crystalline morphology, crosslink density, and density or chain conformation.

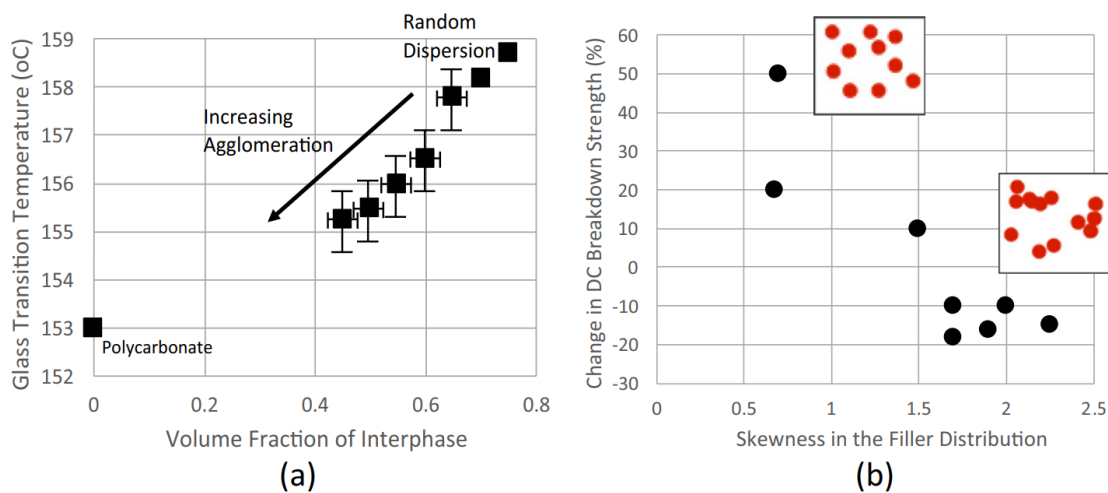


Figure 2.3 (a) The impact of interface volume as a measure of dispersion on glass transition temperature [11], (b) The impact of dispersion as measured via a skewness in the distribution of nanofillers on dielectric breakdown strength [12].

Controlling dispersion to optimize properties is one of the key challenges for nanocomposites particularly at low loadings. The dispersion is controlled by four key factors.

- (1) How tightly the initial agglomerates are bound. For example, spherical nanofillers will be less tightly bound than one-dimensional (1D) rods or 2D sheets because of the contact surface area. Israelachvili [11] quantifies this interaction for two fillers of different aspect ratio in a vacuum (see Table 1). If larger clusters, particularly crystalline clusters form, the binding is even higher.
- (2) The enthalpic and entropic compatibility of the filler, once dispersed, with the matrix. If the

fillers, once dispersed, are thermodynamically compatible with the matrix, then they are likely to remain dispersed.

- (3) The mechanism used to separate the agglomerates (clusters, bundles, or stacks). For example, solvent dispersions have the advantage of the high mobility and small size of the solvent molecules to penetrate agglomerates but have the disadvantage of low viscosity limiting the shear stress that can be applied to break up agglomerates. Sonication can be used to create the forces needed to separate the agglomerates, but can damage some nanofillers[13]. Polymer melts, on the other hand, have higher viscosity leading to large shear stresses to break up the agglomerates, but diffusion of the chains into the agglomerates is slow.
- (4) The thermomechanical history. Composites that have been frozen into a specific dispersion via either quenching from the melt or from a solvent may have a dispersion controlled in part by the kinetics of the processing.

Table 2.1. Interaction laws for different particles

<i>Type of nanoparticle</i>	<i>van der Waals interaction energies</i>
Two spheres (radii, R_1 and R_2) separated by distance D	$W = -\frac{A}{6D} \left(\frac{R_1 R_2}{R_1 + R_2} \right)$
Two parallel cylinders (radii, R_1 and R_2) separated by a distance D and of length L	$W = -\frac{AL}{12\sqrt{2D^{3/2}}} \left(\frac{R_1 R_2}{R_1 + R_2} \right)^{1/2}$
Two crossed cylinders (radii, R_1 and R_2) separated by a distance D	$W = \frac{A}{6D} (R_1 R_2)^{1/2}$
Two parallel plates separated by a distance D	$W = -\frac{A}{12\pi D^2}$

Notes: A (Hamaker constant) $= \pi^2 C \rho_1 \rho_2$, where C is the coefficient in the atom–atom pair potential, and ρ_1 and ρ_2 are the number of atoms per unit volume.

Source: Reproduced from Krishnamoorti, R., 2007. Strategies for dispersing nanoparticles in polymers. MRS Bulletin 32 (4), 341–347.

For a given starting state of the particles, tubes, or plates, one key technique for controlling dispersion is to alter the extrinsic interface to improve compatibility. Consider first a composite in thermodynamic equilibrium, with spherical fillers that are unmodified or modified with small molecules. Both the entropic and enthalpic interactions are important in determining dispersion.

The entropic interactions are complicated. For spherical fillers significantly smaller than the polymer matrix radius of gyration R_g , dispersion is encouraged because the entropy of mixing is substantial. On the other hand, for spherical fillers with a diameter on the order of R_g , there is an entropic depletion driving force for particle agglomeration which is quite strong in the a thermal limit (no filler/matrix enthalpic attraction or repulsion). In essence, this is due to the reduction in entropy for the matrix chains in between fillers that are close together. If, however, there is even

a small enthalpic attraction of the matrix for the filler, the entropic penalty is overcome and the driving force is for filler dispersion[14]. This is because when the particles agglomerate, there is a significant surface area that is not in contact with another particle (or a matrix) and is thus of high energy. This drives dispersion. For larger spherical fillers and for higher aspect ratio fillers, entropy alone cannot drive dispersion[15]. For nanotubes and nano-platelets, the entropy loss for polymers to diffuse into the agglomerates is regained if the fillers separate, but the enthalpic attraction required to drive the diffusion is the overwhelming parameter controlling dispersion. The intercalated ions or organic molecules in clay can be modified to reduce this entropic barrier[16].

The enthalpic driving force for dispersion is a balance between the polymer–filler attraction and filler–filler attraction. For spherical fillers and many nanotube fillers, the filler–filler attraction is a van der Waals attraction[17]. For clays, there are strong Lewis acid/base polar interactions in the gallery between the layers[16]. Surface modification of the fillers to create enthalpic compatibility with the matrix is the primary method for insuring dispersion. There are many wonderful reviews of methods for surface modification[15, 18-23]. As the filler/matrix attraction increases, it has been found through both computation and experiment that the propensity for dispersion increases nonlinearly.[24-30] Computationally it has been shown that for small filler/matrix attraction, the polymer matrix adsorbs on the filler and prevents aggregation, but at even higher attraction, the chains can create bridging between particles[31]. Experimentally, several papers have shown that the ratio of the work of adhesion between the matrix and filler (W_{PF}) and the work of adhesion between nanoparticles (W_{FF}) can be used to predict the dispersion of spherical nanofillers. For example, the contact angle, $\cos\theta$, can be calculated from the work of adhesion, or more fundamentally the polar, γ^p , and dispersive, γ^d , components of the surface energy.

2.4. The Synergistic Effect of Ternary Polyblend Composites System

Graphene reinforced polymer has lately empowered the dramatic enhancement of portable electronics and electric vehicles by proffering better means for storing electricity. To fulfill the consistently expanding demand for lightweight, compact electronic items, electric vehicles, and

brilliant lattices with sustainable power source combinations, the hybridization of graphene with several functions have been manifested. Being versatile and powerful procedure to essentially upgrade the performance of different energy frameworks because such hybridization can bring about synergistic impacts that consolidate the finest qualities of incorporated segments and profer new capacities and properties.

Now we will report the effect of graphene in more complex epoxy systems, with three phases in the final state. Numerous systems have been studied for a better reinforcement (synergy) with two kinds of fillers or separated phases. Two main cases will be discussed.

The first case is the mixture of two additives, at least one organo-modified lamellar silicate s (OLS), not miscible in the epoxy precursors, incorporated to an epoxy matrix. The introduction of OLS into the matrix or between the plies improved the toughness but did not improve the interlaminar shear strength.

In a second case, an initially miscible additive (rubber, thermoplastic, or precursors for sol-gel chemistry) was introduced in the initial mixture and phase separation appeared during CRIPS, leading to a ternary phase system. In most cases, stiffness was the result of balancing the ratio of soft and hard fillers and toughness was improved via multiple cracks and crack bifurcation mechanisms. Thermoplastics undergoing CRIPS, such as PEI and PMMA, were also used, leading to significant improvements in toughness.

In general, the effect of graphene on the curing reaction of epoxy can be categorized into two scenarios: (i) Graphene themselves are not involved in curing reactions, but changes the physical properties of the epoxy, which in turn alters the curing kinetics; (ii) the functional groups on the surface of graphene participate in the curing reaction. In some cases, functionalized graphene may have multiple effects on epoxy curing. Various degrees of graphene functionalization and graphene concentrations may also influence curing reactions to a different degree or sometimes with the opposite effect, which might account for some inconsistent findings reported in the literature.

As discussed above, the direct or indirect effects of graphene on the curing reaction can lead to significant thermal and mechanical property changes of epoxy/graphene nanocomposites,

which would complicate their property evaluation. This issue has attracted more and more attention recently, but only limited progress has been made. This is likely due to the difficulty in the quantitative assessment of the above effect.

It may be possible to observe synergistic properties of the composites that depend upon the type of graphene chemical structure, morphology, base polymer matrix and its physiochemical characteristics, interaction with the added graphene based nanofiller, and also largely on the composite processing conditions

2.5. Techniques of Characterization

2.5.1. Contact angle measurement

Contact angle, θ (theta), is a quantitative measure of wetting of a solid by a liquid shown in Figure 2.4. The contact angle is geometrically defined as the angle formed by a liquid at the three-phase boundary where a liquid, gas, and solid intersect. There are three different forces acting on this three-phase contact point between solid, liquid and vapor, or in some cases solid, liquid and liquid. Contact angles can be divided into static, dynamic and roughness corrected contact angle.

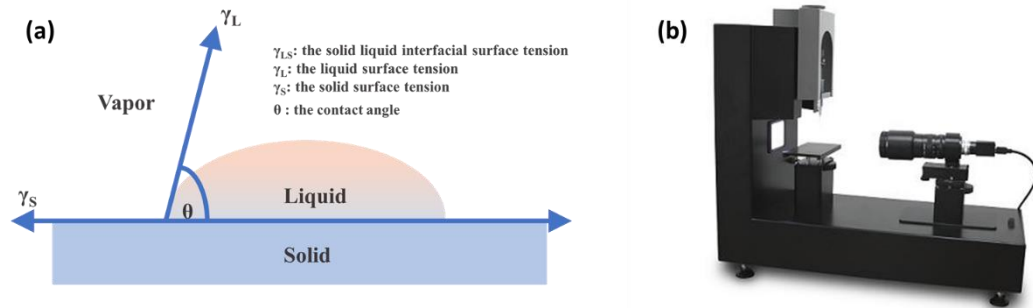


Figure 2.4. The illustration of (a) a drop liquid on a solid substrate with the surface tension and contact angle and (b) an instrument of contact angle measurement (Phoenix 300, SEO Co.).

The contact angle (CA) measurement on a surface is considered the most practical way to obtain the Surface Free Energy (SFE). The theory of the contact angle of pure liquids on a solid was developed nearly 200 years ago in terms of the Young equation:

$$\gamma_L(1 + \cos \theta) = \gamma_S - \gamma_{SL}$$

where γ_L is the experimentally determined surface energy (surface tension) of the liquid, θ is the contact angle, γ_S is the surface energy of the solid, and γ_{SL} is the solid/liquid interfacial energy.

The results of five methods based in the models are compared: the method of Zisman, the geometric mean (GM), the harmonic mean (HM), the Lifshitz-van der Waals / Acid-Base (LW/AB) and the equation of state. The SFE calculated with GM, HM and LW/AB methods change with the amount and type of liquid used, however, when water, glycerol and dimethyl sulfoxide are used together the SFE and its dispersive and polar components are similar in value for the three methods. In the case of the equation of state model the values of SFE change with the liquid used; finally using the Zisman method the SFE values are 20% lower than the values of SFE obtained with the other methods[32].

The Zisman Method

The Zisman method introduces the concept of critical surface energy (γ_c) which is defined as the surface free energy of a liquid that completely wets a surface, that is, the contact angle is zero a $\cos \theta = 1$. The value of γ_c is obtained by measuring the contact angle of a number of different liquids on the same surface, plotting the points in $\cos \theta_L$ vs γ_L axes, extrapolating the fitted curve to the value of $\cos \theta = 1$ and obtaining the value γ_c from the abscissa. The value of γ_c is related through empirical relations developed by Zisman [33] with the surface free energy of the film.

Methods of GM and HM

The HM and GM models are based on the assumption that the intermolecular interactions between two substances have two main components: the dispersive or London component and the polar component due to the contributions given by the Keesom and the Debye forces. Therefore, the SFE (γ) arises from these interactions contributions as the sum of two components, the dispersive (γ^d) and the polar components (γ^p) [34-36]:

$$\gamma_i = \gamma_i^d + \gamma_i^p \quad (2.1)$$

where i stands for the i-substance or material, in our case liquid or solid. According to the GM method the interfacial solid/liquid energy can be evaluated using the following equation[37]:

$$\gamma_{SL} = \gamma_s + \gamma_L - 2(\sqrt{\gamma_s^d \cdot \gamma_L^d} + \sqrt{\gamma_s^p \cdot \gamma_L^p}) \quad (2.2)$$

which combined with the Young's equation results in:

$$\gamma_L(1 + \cos \theta) = 2\sqrt{\gamma_s^d \cdot \gamma_L^d} + \sqrt{\gamma_s^p \cdot \gamma_L^p} \quad (2.3)$$

On the other hand, the solid/liquid interfacial energy by the HM method is given by[36]:

$$\gamma_{SL} = \gamma_s + \gamma_L - 2\left(\frac{4\gamma_s^d\gamma_L^d}{\gamma_s^d + \gamma_L^d} - \frac{4\gamma_s^p\gamma_L^p}{\gamma_s^p + \gamma_L^p}\right) \quad (2.4)$$

which again, combined with the Young's equation results in the following equation:

$$\gamma_L(1 + \cos \theta) = \frac{4\gamma_s^d\gamma_L^d}{\gamma_s^d + \gamma_L^d} - \frac{4\gamma_s^p\gamma_L^p}{\gamma_s^p + \gamma_L^p} \quad (2.5)$$

The method of LW/AB

In the LW/AB method [38] the SFE is assumed to be composed of two main contributions, a non-polar component γ_i^{LW} due to Lifshitz-van der Waals, similar to the dispersive component defined above, γ_i^d ; and an acid-base component due to Lewis, γ_i^{AB} , similar to the polar component mentioned before, γ_i^p ; therefore, for substrate *i*, the SFE is written as:

$$\gamma_i = \gamma_i^{LW} + \gamma_i^{AB} \quad (2.6)$$

the acid-base component is in turn composed of two contributions: one from electron donors γ_i^- and another from electron acceptors γ_i^+ . In this particular case this component is calculated as:

$$\gamma_i^{AB} = 2\sqrt{\gamma_i^- \cdot \gamma_i^+} \quad (2.7)$$

The solid-liquid interface energy is obtained as:

$$\gamma_{SL} = \gamma_s + \gamma_L - 2\left(\sqrt{\gamma_s^{LW} \cdot \gamma_L^{LW}} + \sqrt{\gamma_s^+ \cdot \gamma_L^-} + \sqrt{\gamma_s^- \cdot \gamma_L^+}\right) \quad (2.8)$$

combining equations above with the Young's equation it is obtained that:

$$\gamma_L(1 + \cos \theta) = 2\left(\sqrt{\gamma_s^{LW} \cdot \gamma_L^{LW}} + \sqrt{\gamma_s^+ \cdot \gamma_L^-} + \sqrt{\gamma_s^- \cdot \gamma_L^+}\right) \quad (2.9)$$

Equation of State method

Neuman and Kwok [39, 40] propose the following equation for the interfacial solid-liquid energy:

$$\gamma_{SL} = \gamma_s + \gamma_L - 2\sqrt{\gamma_s\gamma_L} e^{-\beta(\gamma_L - \gamma_s)^2} \quad (2.10)$$

which combined with the Young's equation gives:

$$\gamma_L(1 + \cos \theta) = 2\sqrt{\gamma_s\gamma_L} e^{-\beta(\gamma_L - \gamma_s)^2} \quad (2.11)$$

where $\beta=0.0001057$ (m/mN)².

2.5.2. Thermogravimetric analysis (TGA)

TGA provides a tool for measuring mass changes in a sample as a function of time and/or temperature. Mass changes are the result of evaporation and decomposition, also of chemical

reactions and magnetic or electrical transitions. Measurable mass changes also occur when gases are absorbed (oxygen, humidity, etc.) This method is standardized in ISO 11358. Coupling it with FTIR or mass spectroscopy (MS) (Figure 2.5) provides a tool to detect materials that contribute to a particular loss of mass; this can be helpful in finding solutions for polymer analytical problems.



Figure 2.5. TGA instrument (Q50, TA Instruments, USA).

Depending on the measurement task, various purge gases are used for recording mass change as a function of temperature and/or time. Often, the differential measuring signal TG/dt , also termed the DTG curve, is introduced for the interpretation and separation of effects. The DTG signal provides additional information on degradation kinetics.

2.5.3. Differential scanning calorimeter (DSC)

DSC devices are designed according to two basic measuring principles: heat-flux calorimetry and power compensation calorimetry. Two bean-size pans (trays, dishes) holding a sample and an inert reference are heated simultaneously, according to a selected linear temperature program. Air is often used as the reference. In heat-flux calorimetry, sample and reference lie in a cylindrical oven. Given thermal symmetry of the arrangement, no temperature difference occurs between pans when the oven is heated. However, if the specific heat capacity of the sample changes with elevated temperature, a temperature difference arises, which theoretically is proportional to the specific heat capacity. This arrangement (Figure 2.6a) can be

calibrated and used for measuring specific heat capacity. An improvement in the resolving power of heat-flux calorimetry has been achieved by the so-called Tzero™ technology. Compared to conventional heat-flux calorimetry by disk measuring systems (Figure 2.6a), in which sample and reference temperatures are measured, a sensor is utilized containing, among other things, an additional thermocouple (Figure 2.6b). This additional temperature sensor measures the so-called base line temperature, enabling enhanced correction of thermal asymmetries in the oven. In power compensation calorimetry, sample and reference are completely separated. Sample and reference trays have their own heaters and temperature sensors. Sample and references are heated up at the same rate with the aid of a control unit in such a way that no temperature difference arises between them. When the specific heat capacity of the sample changes, more (in endothermic processes) or less (in exothermic processes) heating power is transferred to the sample to avoid a temperature difference.

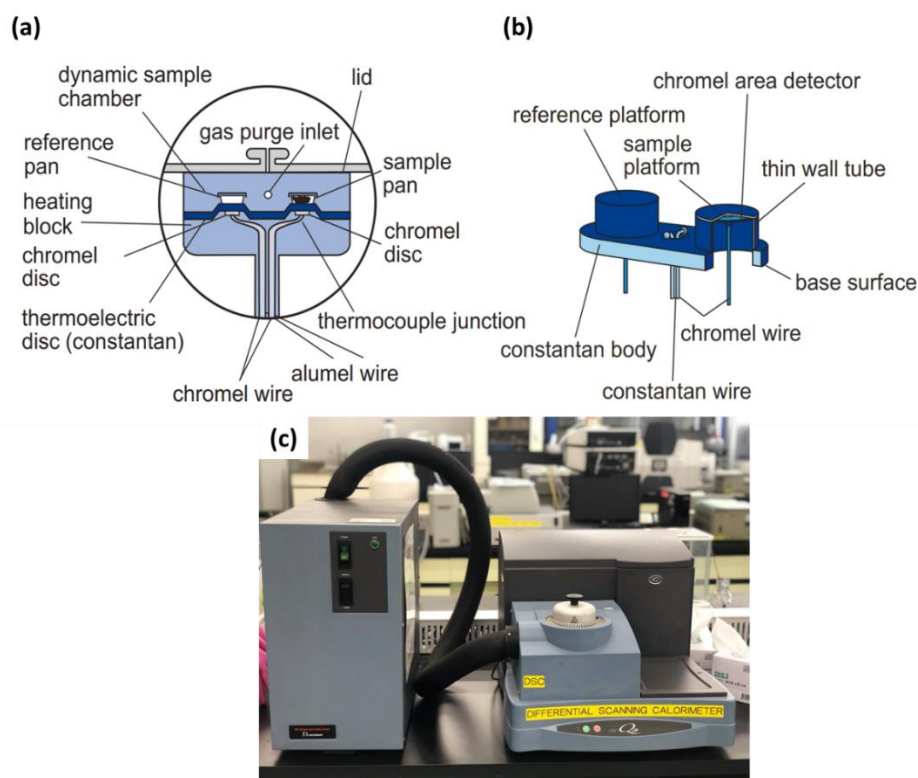


Figure 2.6. The structure of (a) DSC measuring cell (heat-flow principle) disk tester system, (b) Tzero™ sensor, and (c) DSC instrument (Q20 V24.10, TA Instruments Co., USA).

2.5.4. Dynamic mechanical analysis (DMA)

Dynamic mechanical analysis (DMA) is the technique of applying a stress or strain to a

sample and analyzing the response to obtain phase angle and deformation data. The data collected allow the calculation of dynamic mechanical properties like the damping or tan delta (δ) as well as complex modulus and viscosity data. Modulus data in the form of the storage modulus is conceptually equivalent to that collected from traditional mechanical tests and gives a measurement of the strength and stiffness of the materials. Viscosity information on how the material flows under stress can be obtained from the complex viscosity. The ratio of the storage modulus to loss modulus is called damping or $\tan\delta$ and is calculated directly from the phase angle δ . Damping is a measure of the internal friction of the material and indicates the amount of energy loss in the material as dissipated heat. This allows DMA to be used to predict how good a material is at acoustical or vibrational damping. Normally, DMA data for solids is displayed as storage modulus and damping versus temperature, with multicurve used to show frequency effects. Melt data is often shown against frequency like classical rheological data.

Two approaches are used: (1) forced frequency, where the signal is applied at a set frequency and (2) free resonance, where the material is perturbed and allowed to exhibit free resonance decay. Most DMAs are of the former type while the torsional braid analyzer (TBA) is of the latter. In both approaches, the technique is very sensitive to the motions of the polymer chains and it is a powerful tool for measuring transitions in polymers. It is estimated to be 100 times more sensitive to the glass transition than differential scanning calorimetry (DSC) and it resolves other more localized transitions not detected in DSC.[41]



Figure 2.7. DMA instrument (DMA (Q800, TA Instruments, USA)

As the free volume continues to increase with increasing temperature, the glass transition occurs where large segments of the chain start moving. This transition is also called the α -transition. The glass transition is very dependent on the degree of polymerization up to a value known as the critical glass transition or the critical molecular weight. Above this value, the glass transition typically becomes independent of molecular weight. The glass transition represents a major transition for many polymers, as physical properties change drastically as the material goes from a hard glassy to a rubbery state. It defines one end of the temperature range over which the polymer can be used, often called the operating range of the polymer. For where strength and stiffness are needed, it is normally the upper limit for use. In rubbers and some semicrystalline materials like polyethylene and polypropylene, it is the lower operating temperature. Changes in the temperature of the glass transition temperature are commonly used to monitor changes in the polymer such as plasticizing by environmental solvents and increased cross-linking from thermal or UV aging.

The glass transition temperature (T_g) of cured materials or thin coatings is often difficult to measure by other methods, and more often than not the initial cost justification for a DMA is measuring a hard-to-find T_g . While estimates of the relative sensitivity of DMA to DSC or DTA (differential thermal analysis) vary, it appears that DMA is 10-100 times more sensitive to the changes occurring at the T_g . The T_g in highly cross-linked materials can easily be seen long after the T_g has become too flat and broad to be seen in DSC. This is also a problem with certain materials like medical grade urethanes and very highly crystalline polyethylenes.

The method of determining the T_g in DMA can be a manner for disagreement as at least five ways are in current use. Depending on the industry standards or background of the operator, the peak or onset of the $\tan\delta$ curve, the onset of the E' drop, or the onset or peak of the E'' curve may be used. The values obtained from these methods can differ up to 25 °C from each other on the same run. In addition, a 10-20 °C difference from the DSC is also seen in many materials. In practice, it is important to specify exactly how the T_g should be determined. For DMA, this means defining the heating rate, applied stresses (or strains), the frequency used, and the method of determining the T_g . For example, the sample will be run at 10 °C/min under 0.05% strain at 1Hz

in nitrogen purge (20 cc/min) and the T_g determined from the peak of the $\tan\delta$ curve.

2.5.5. Fourier Transform Infrared Spectroscopy (FT-IR)

The main area of application for infrared spectroscopy (IR spectroscopy) is in the identification of polymers. IR spectroscopy is an absorption-spectroscopic method operating at wavelengths ranging from approx. 780 nm to 1 mm. The most important spectral range for analyzing polymers is that of mid-range infrared wavelengths from 2.5 to 25 μm . Spectral range is often expressed as reciprocal wavelength in cm^{-1} , termed wave number ν , i.e., median IR corresponds to wave numbers of approx. 4000 to 400 cm^{-1} . The absorption bands occurring in the IR spectra can be associated with the oscillation of particular valences within polymer molecules or entire groups of atoms (functional groups). These bands are identified using IR spectrum databases. Thus, IR spectroscopy is a suitable method for analyzing polymers and their additives. Qualitative and quantitative analysis using IR spectroscopy are based on wavelength-dependent interaction between IR rays and molecules or groups of molecules. Due to this interaction, absorption spectra are generated with characteristic bands. Various instrumented methods are used for obtaining IR spectra. In practice, IR spectrometers are classified according to their principle of wavelength selection. The most frequently used are dispersive IR spectrometers and Fourier transform infrared spectrometers (FT-IR). Figure 2.8a illustrates the working principle of an FT-IR spectrometer.

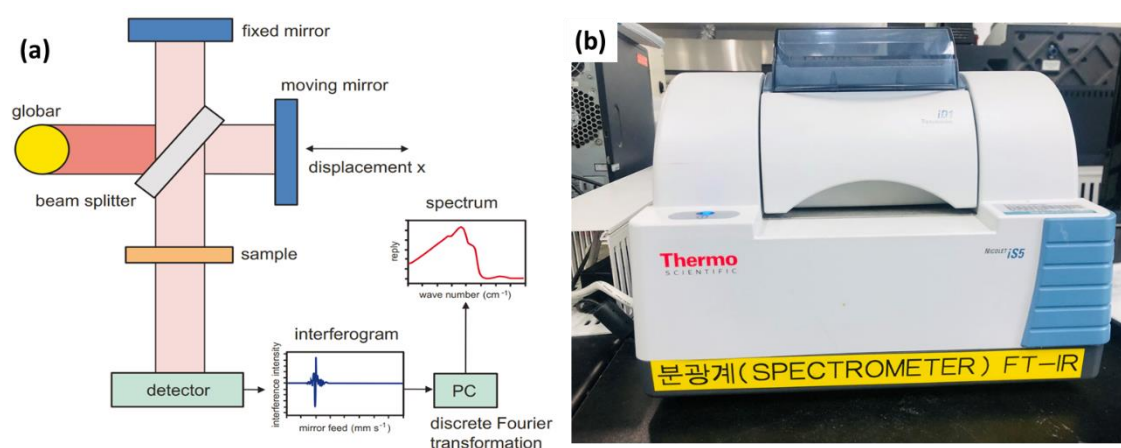


Figure 2.8. (a) Configuration diagram of an FT-IR spectrometer and (b) FT-IR instrument (Nicolet™ iS™ 5, Thermo Fisher Scientific Inc., USA).

2.5.6. Four-point probe technique

The four-probe method works by contacting four equally-spaced, co-linear probes to the

material. This is known as a four-point probe, and a schematic is shown in Figure 2.9.

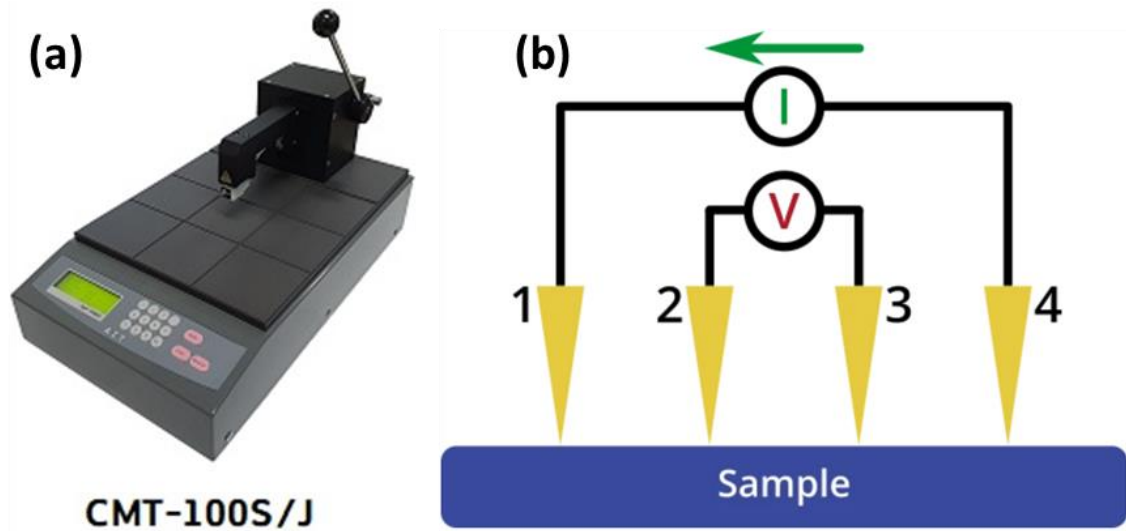


Figure 2.9. Schematic diagram of (a) A.I.T four-point probe system and (b) a four-point probe circuit.

A DC current is applied between the outer two probes (1 and 4) and a voltage drop is measured between the inner two probes (2 and 3). The sheet resistance can then be calculated using the following equation:

$$R_s = \frac{\pi}{\ln(2)} \frac{\Delta V}{I} = 4.53236 \frac{\Delta V}{I} \quad (2.12)$$

Here, R_s is the sheet resistance, ΔV is the change in voltage measured between the inner probes, and I is the current applied between the outer probes. The sheet resistance (R_s) is expressed with the units Ω/sq , or “ohms per square”, to differentiate it from bulk resistance.

In addition to the factor of $\pi/\ln(2)$, a geometric correction factor is often required. The correction factor is based upon the size and shape of the sample, as well as the positioning of the probes, and accounts for the limitation of current pathways through it. If the thickness of the measured material is known, then the sheet resistance can be used to calculate its resistivity:

$$\rho = R_s \cdot t = \frac{1}{\sigma \cdot t} \quad (2.13)$$

Here, ρ is the resistivity with the units $\Omega \text{ cm}$, or “ohms centimeter”, σ is the electrical conductivity, and t is the thickness of the material. This technique is also known as the Kelvin technique, a method of eliminating wire and contact resistances from a resistance measurement.

Figure 2.10 shows the circuit resistances of a four-point probe measurement.

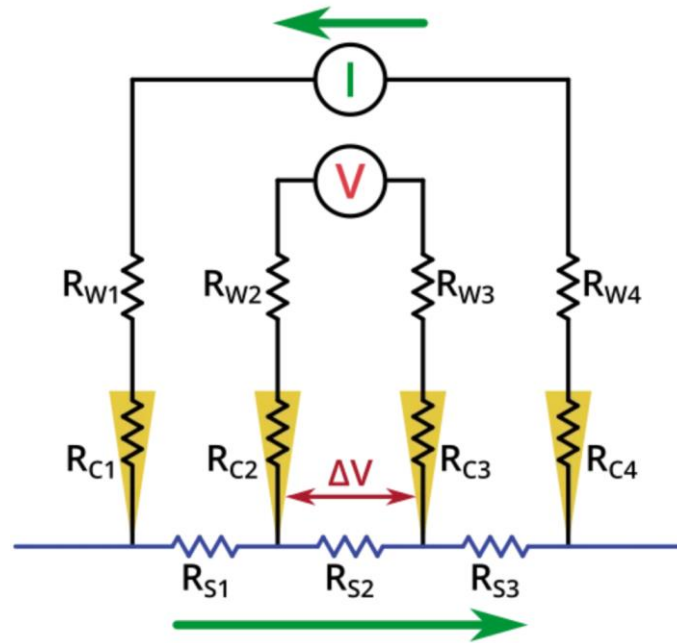


Figure 2.10. Equivalent circuit diagram of a four-point probe, showing the wire resistances (R_W), contact resistances (R_C), and sample resistances (R_S). The green arrows represent current flow.

As no current flows through the inner two probes, the wire resistances of R_{W2} and R_{W3} and the contact resistances of R_{C2} and R_{C3} do not affect the voltage measured at the voltmeter. This means that the measured decrease in voltage (ΔV) between the inner two probes arises entirely from R_{S2} . Therefore, ΔV can be used along with the applied current in the sheet resistance equation to calculate the value of R_{S2} (i.e., the sheet resistance).

2.5.7. Electromagnetic interference (EMI) shielding

Electromagnetic interference (EMI) shielding refers to the reflection and/or adsorption of electromagnetic radiation by a material, which thereby acts as shielding against the penetration of the radiation through the shield. As electromagnetic radiation, particularly that at high frequencies (e.g., radio waves, such as those emanating from cellular phones) tend to interfere with electronics (e.g., computers), EMI shielding relates to the high demand of today's society on the reliability of electronics and the rapid growth of radio frequency radiation sources.

Experimental determination of the EMI shielding efficiency

Experimental instruments called network analyzers are introduced for the evaluation of EMI SE. Two types of network analyzers, which operate on the principle of the waveguide technique, can be applied: a scalar network analyzer (SNA) and vector network analyzer (VNA). The scalar network analyzer (SNA) determines the amplitude of signals, while the network analyzer VNA

detects the signal magnitude response, as well as phases of various signals. As SNA cannot be used for the determination of complex signals (complex permeability or permittivity), VNA is the more preferred instrument, despite its higher price. VNA containing two ports emits electromagnetic radiation in the examined frequency range from both ports and records the reflected radiation, as well as the transmitted radiation obtained from the tested shielding material (Figure 2.11a). According to the EMI shielding theory, when the electromagnetic propagating wave reaches the surface of the shielding material, the incident power is divided into the reflected, absorbed and transmitted power, and the corresponding power coefficients of absorbance (A), reflectance (R), and transmittance (T). Their sum is always equal to 1, and this means that $R + T + A = 1$. VNA detects the complex scattering parameters (S parameters). Based on these parameters, information about the permittivity, permeability, as well as EMI SE can be obtained using suitable algorithms and models, such as Nicolson–Ross–Weir (NRW), NIST iterative, new non-iterative, short circuit line (SCL) techniques. Among them, the Nicolson–Ross–Weir technique is the most widely used regressive/iterative analysis, as it provides the direct calculation of both permittivity and permeability from the S -parameters. There are experimentally measured real and imaginary parameters S_{11} (or S_{22}) and S_{21} (or S_{12}), which correlate with the reflection coefficient (R) and transmission coefficient (T), $R = |S_{11}|^2 = |S_{22}|^2$ and $T = |S_{12}|^2 = |S_{21}|^2$, respectively. The absorption coefficient can be calculated as $A = 1 - R - T$. Figure 2.11b illustrates the S -parameters from the two-port vector network analyzer (VNA), which represent the incident and transmitted EM waves. The S parameters are designated as the forward reflection coefficient (S_{11}), reverse reflection coefficient (S_{22}), forward transmission coefficient (S_{12}) and backward transmission coefficient (S_{21}). The corresponding parameters Z (Ω), RL (dB), SE_A (dB), SE_R (dB), and SE_T (dB) can be calculated as follows:

$$Z = Z_0 \left| \frac{1 + S_{11}}{1 - S_{11}} \right| \quad (2.14)$$

$$RL = 20 \log |S_{11}| \quad (2.15)$$

$$SE_T = 10 \log \left(\frac{1}{|S_{12}|^2} \right) = 10 \log \left(\frac{1}{|S_{21}|^2} \right) = 10 \log \left(\frac{1}{T} \right) \quad (2.16)$$

$$SE_R = 10 \log \left(\frac{1}{1 - |S_{11}|^2} \right) = 10 \log \left(\frac{1}{1 - |S_{22}|^2} \right) = 10 \log \left(\frac{1}{1 - R} \right) \quad (2.17)$$

$$SE_A = 10 \log \left(\frac{1 - |S_{11}|^2}{|S_{12}|^2} \right) = 10 \log \left(\frac{1 - |S_{22}|^2}{|S_{21}|^2} \right) = 10 \log \left(\frac{1 - R}{T} \right) \quad (2.18)$$

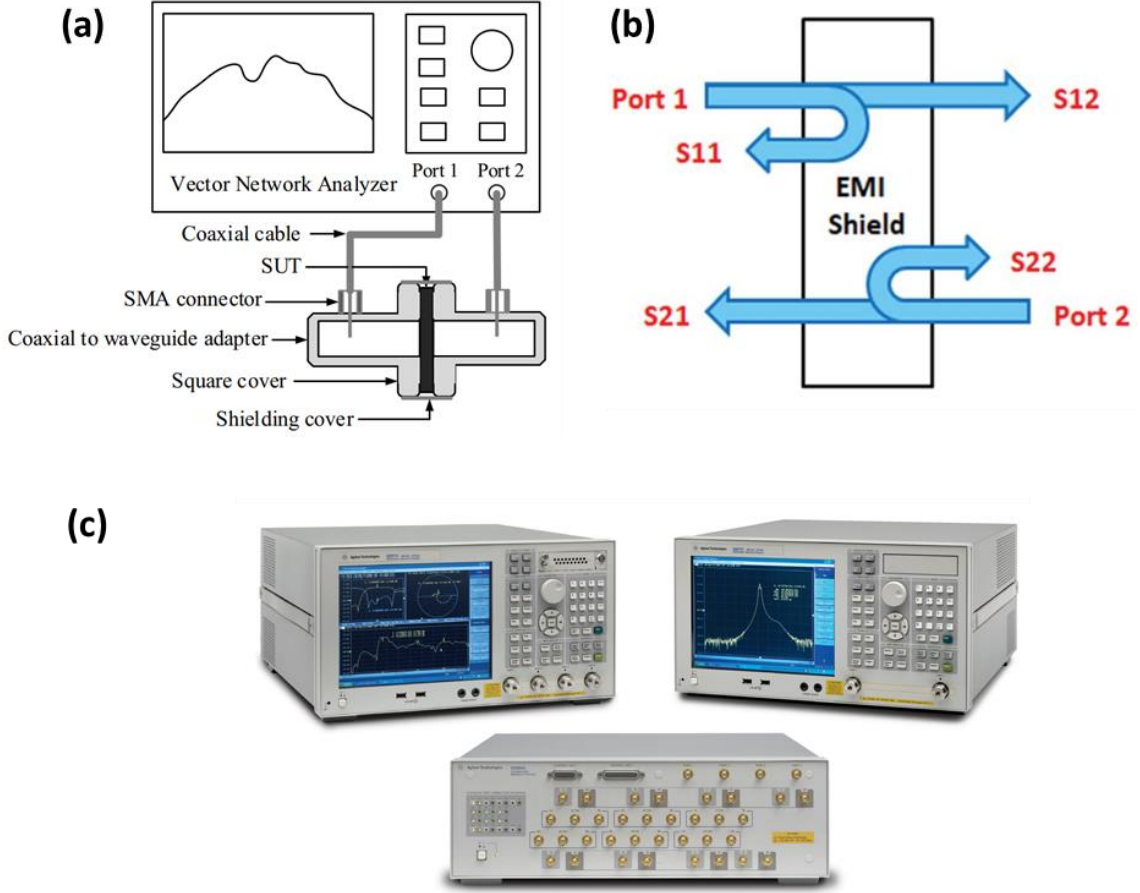


Figure 2.11. (a) SE measurement setup of samples (b) schematic illustration of the scattering parameters from a two-port VNA[42], and (c) The vector network analyzer (E5071C Agilent Inc.).

A better understanding of the absorption by the EMI shield can be achieved by calculating its effective absorption (A_{eff}) percentage using the equation[43]:

$$A_{\text{eff}} = \left(\frac{1 - R - T}{1 - R} \right) \times 100\% \quad (2.19)$$

where A_{eff} represents the amount of power absorbed by the shield, and we conducted the SE by E5071C vector network analysis shown in Figure 2.11c.

2.5.8.X-ray photoelectron spectroscopy (XPS)

XPS is a quantitative spectroscopic technique that measures the elemental composition, empirical formula, chemical state, and electronic state of the elements that exist within a material. XPS spectra are obtained by irradiating a material with a beam of aluminum or magnesium X-rays while simultaneously measuring the kinetic energy (KE) and the number of electrons that

escape from the top 1 to 10 nm of the material being analyzed. Figure 2.12 shows the components of XPS system and Figure 2.12 shows the depth of XPS technique.

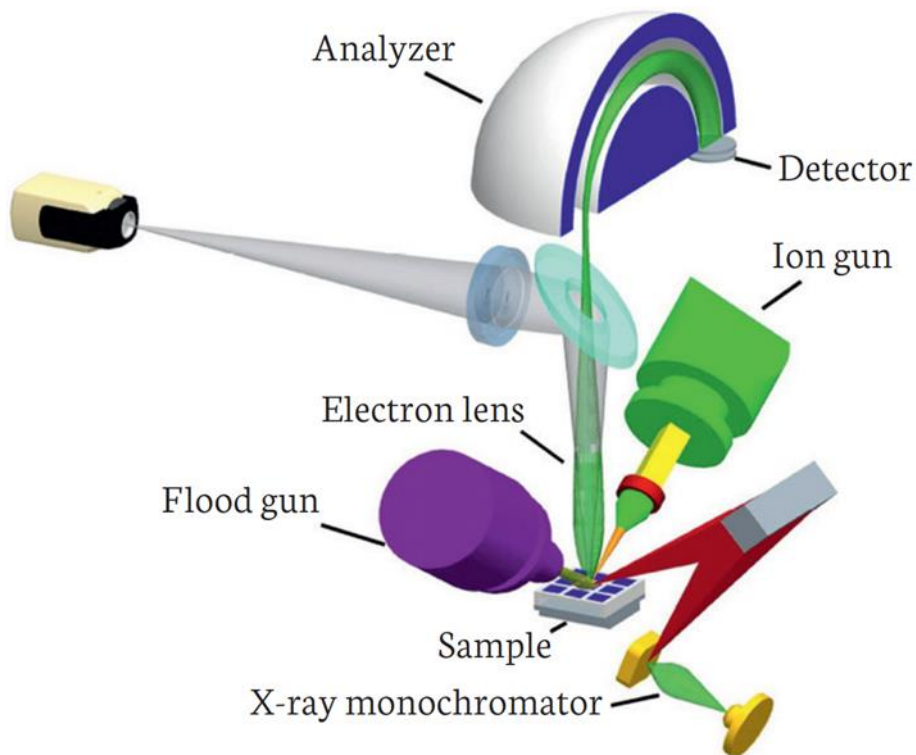


Figure 2.12. Components of an XPS system. Reproduced with permission from Thermo Fisher Scientific.

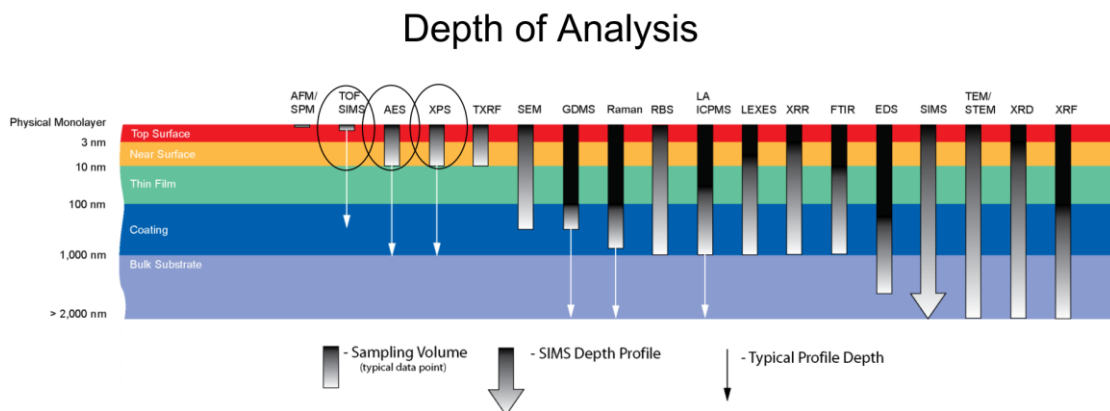


Figure 2.13. Depth of surface chemical analysis techniques.

a) The principle of the technique.

In XPS, the sample is irradiated with soft x-rays (energies lower than ~ 6 keV) and the kinetic energy of the emitted electrons is analyzed [Figure 2.14(a)]. The emitted photoelectron is the result of the complete transfer of the x-ray energy to a core level electron. This is expressed mathematically in Eq. (2.20). It simply states that the energy of the x-ray ($h\nu$) is equal to the

binding energy (BE) of the electron (how tightly it is bound to the atom/orbital to which it is attached), plus the kinetic energy (KE) of the electron that is emitted, plus the spectrometer work function (Φ_{spec}), a constant value,

$$h\nu = BE + KE + \Phi_{\text{spec}} \quad (2.20)$$

To determine the binding energy of an electron, Eq. (2.20) can be rearranged to obtain Eq. (2.21), where the terms on the right are either known ($h\nu$ and Φ_{spec}) or measured in the XPS experiment (KE),

$$BE = h\nu - KE - \Phi_{\text{spec}} \quad (2.21)$$

This concept is also demonstrated diagrammatically in Figure 2.14. Note that the photoelectron binding energy is measured with respect to the sample Fermi level (not the vacuum level) which is the reason that Φ_{spec} is included.

Photoelectron peaks are notated by the element and orbital from which they were ejected. For example, “O 1s” describes electrons emitted from the 1s orbital of an oxygen atom. Any electron with a binding energy less than the x-ray source energy should be emitted from the sample and observed with the XPS technique. The binding energy of an electron is a material property and is independent of the x-ray source used to eject it. When experiments are performed with different x-ray sources, the binding energy of photoelectrons will not change; however, the kinetic energy of the photoelectrons emitted will vary as described by Eq. (2).

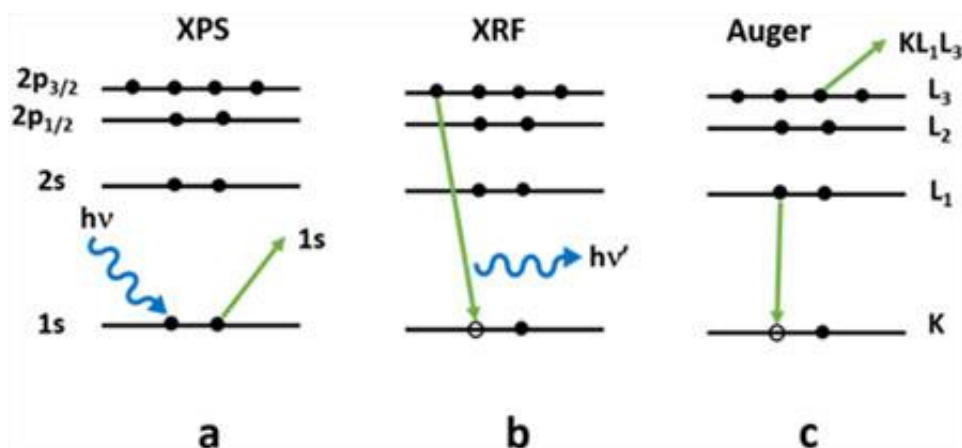


Figure 2.14. Processes that result from x-ray bombardment of a surface include (a) emission of a photoelectron, (b) x-ray fluorescence, and (c) emission of an Auger electron.

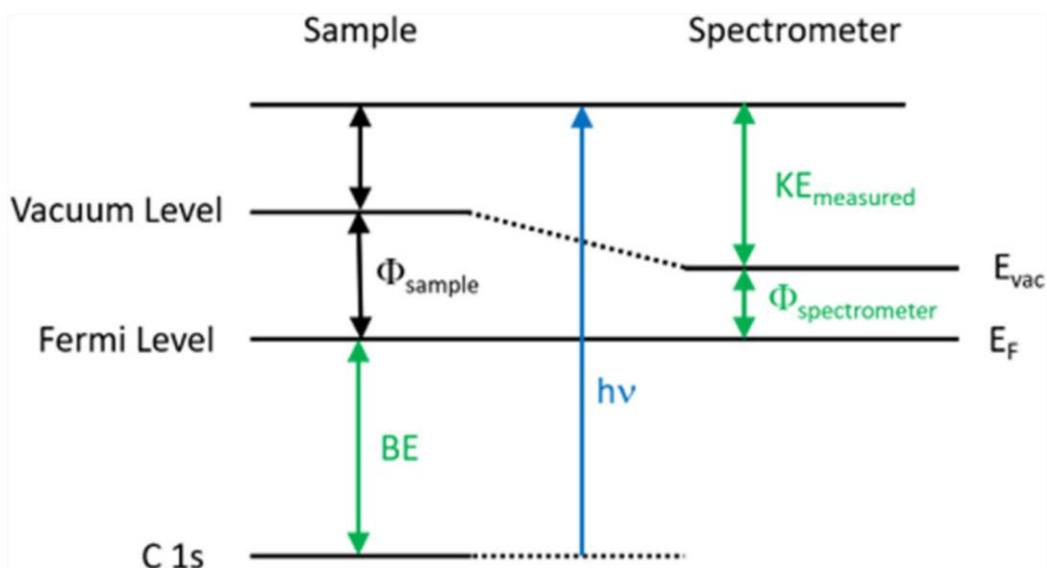


Figure 2.15. Energy level diagram illustrates schematically the basic XPS equation, including the x-ray source energy ($h\nu$), the binding energy of the electron (BE), the measured kinetic energy of the electron (KE_{measured}), and the work function of the spectrometer ($\Phi_{\text{spectrometer}}$).

b) Instrument of XPS

An XPS instrument contains an x-ray source, sample stage, extraction lenses, analyzer, and detector housed in an ultra-high vacuum environment. A schematic diagram of an XPS system is shown in Figure 2.15.

XPS instruments are housed within ultra-high vacuum (UHV) environments for two reasons. First, the emitted electrons must not scatter off air molecules while traveling to the analyzer, and this requires vacuum levels on the order of 10^{-5} – 10^{-6} mbar. In practice, XPS systems typically have much lower base pressures that are closer to 10^{-9} – 10^{-10} mbar. Because XPS is a surface sensitive technique, it is very sensitive to surface contamination. At a pressure of 1×10^{-6} mbar and a sticking coefficient of 1 (every molecule that strikes the surface sticks to that surface), there would be one monolayer of contamination in 2 s! As a result, XPS instruments utilize the UHV environment to reduce the surface contamination that occurs within the chamber.

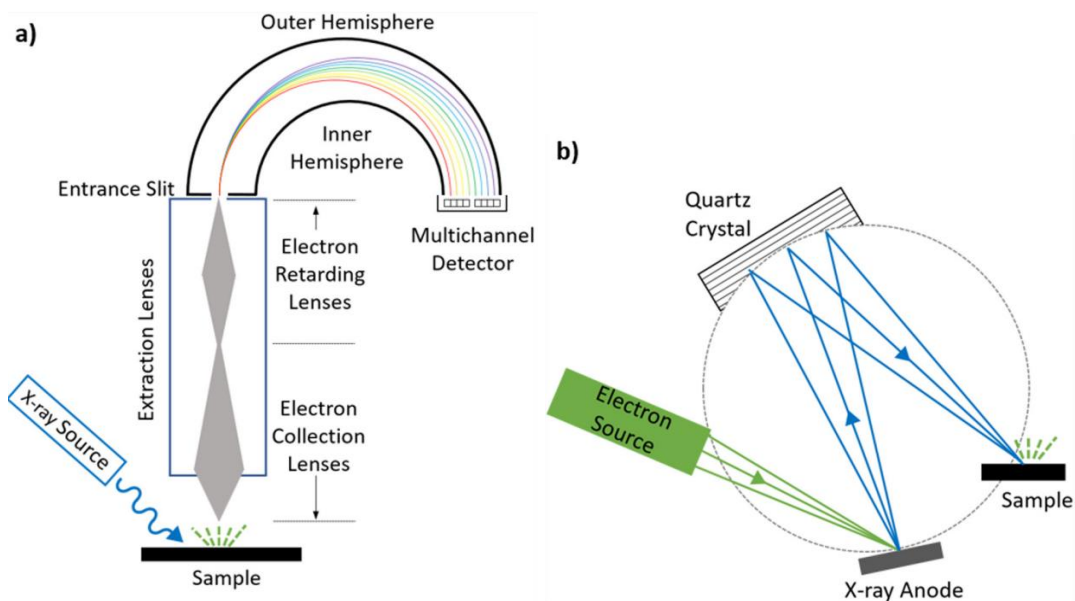


Figure 2.16. Schematic diagrams show the major components of an (a) XPS instrument and (b) monochromator.

- (1) Energy: The energy of the source will determine the transitions that can be measured.
- (2) Linewidth: For non-monochromatic sources, the natural linewidth will limit the resolution of the measurement. (Monochromatic sources offer much narrower linewidths.)
- (3) Analysis depth: Higher energy sources will probe deeper in the sample.
- (4) Ionization cross section: This measure of the probability that an atom will lose an electron due to x-ray irradiation decreases for higher kinetic energy electrons produced by higher energy sources.

XPS systems require were originally equipped with Al and/or Mg sources, often in the form of a dual anode source that contains both Al and Mg anodes which can be individually selected. Many instruments incorporate a monochromator, typically for an aluminum source. As shown in Figure 2.16(b), aluminum x-ray monochromators utilize a quartz crystal positioned at a specific angle to allow only Al $K\alpha$ x-rays to diffract, filtering out other Al x-ray lines and Bremsstrahlung radiation (continuous energy x-ray radiation produced by x-ray sources). Repositioning the quartz crystal can also allow monochromatization of Ag $L\alpha$ x-rays, and dual anode monochromatic Al/Ag sources are now available. Other monochromatic sources, such as chromium, can also be obtained.

There are several advantages to monochromatic sources and some manufacturers are moving toward instruments exclusively equipped with monochromatic sources. The first advantage is that

the monochromator eliminates any excitation by x-ray lines other than the most intense main line. For example, a nonmonochromatic Mg x-ray source will irradiate the samples with the most intense Mg $K\alpha_{1,2}$ line but also with other less intense lines. The most intense of these other lines is the Mg $K\alpha_3$ with an energy that is 8.4 eV lower than the Mg $K\alpha_{1,2}$ line and an intensity that is 9.2% of the main line. As a result, additional peaks due to excitation with multiple x-ray energies will appear in the XPS spectrum, and they are called satellite peaks.

References

- [1] Rao C, Kulkarni G, Thomas PJ, Edwards PP. Size-dependent chemistry: properties of nanocrystals. *Advances In Chemistry: A Selection of CNR Rao's Publications (1994–2003)*: World Scientific; 2003. p. 227-33.
- [2] Wada S, Yasuno H, Hoshina T, Kakemoto H, Kameshima Y, Tsurumi T. Size dependence of THz region dielectric properties for barium titanate fine particles. *Journal of electroceramics*. 2008;21:198-201.
- [3] Yao Y, Wei Y, Chen S. Size effect of the surface energy density of nanoparticles. *Surface Science*. 2015;636:19-24.
- [4] Fischer FD, Waitz T, Vollath D, Simha NK. On the role of surface energy and surface stress in phase-transforming nanoparticles. *Progress in Materials Science*. 2008;53:481-527.
- [5] Mont MA, Schmalzried TP, Seyler TM. Selected papers from the First Annual United States Comprehensive Course on Resurfacing Hip Arthroplasty-Introduction. *JOURNAL BONE JOINT SURGERY INC 20 PICKERING ST, NEEDHAM, MA 02192 USA*; 2008. p. 1-2.
- [6] Caseri W. Nanocomposites of polymers and metals or semiconductors: historical background and optical properties. *Macromolecular Rapid Communications*. 2000;21:705-22.
- [7] Maillard D, Kumar SK, Fragneaud B, Kysar JW, Rungta A, Benicewicz BC, et al. Mechanical Properties of Thin Glassy Polymer Films Filled with Spherical Polymer-Grafted Nanoparticles. *Nano letters*. 2012;12:3909-14.
- [8] Zhao Y, Thorkelsson K, Mastroianni AJ, Schilling T, Luther JM, Rancatore BJ, et al. Small-molecule-directed nanoparticle assembly towards stimuli-responsive nanocomposites. *Nature Materials*. 2009;8:979-85.

- [9] Li Y, Krentz TM, Wang L, Benicewicz BC, Schadler LS. Ligand engineering of polymer nanocomposites: from the simple to the complex. *ACS applied materials & interfaces*. 2014;6:6005-21.
- [10] Li Y, Krentz TM, Wang L, Benicewicz BC, Schadler LS. Ligand engineering of polymer nanocomposites: from the simple to the complex. *ACS applied materials & interfaces*. 2014;6:9:6005-21.
- [11] Qiao R, Deng H, Putz KW, Brinson LC. Effect of particle agglomeration and interphase on the glass transition temperature of polymer nanocomposites. *Journal of Polymer Science Part B: Polymer Physics*. 2011;49:740-8.
- [12] Calebrese C, Hui L, Schadler LS, Nelson JK. A review on the importance of nanocomposite processing to enhance electrical insulation. *IEEE Transactions on Dielectrics and Electrical Insulation*. 2011;18:938-45.
- [13] Lu K, Lago R, Chen Y, Green MH, Harris PF. Mechanical damage of carbon nanotubes by ultrasound. *Carbon (New York, NY)*. 1996;34:814-6.
- [14] Mackay ME, Tuteja A, Duxbury PM, Hawker CJ, Van Horn B, Guan Z, et al. General strategies for nanoparticle dispersion. *Science*. 2006;311:1740-3.
- [15] Kumar SK, Krishnamoorti R. Nanocomposites: structure, phase behavior, and properties. *Annual Review of Chemical and Biomolecular Engineering*. 2010;1:37-58.
- [16] Vaia RA, Giannelis EP. Polymer melt intercalation in organically-modified layered silicates: model predictions and experiment. *Macromolecules*. 1997;30:8000-9.
- [17] Green PF. The structure of chain end-grafted nanoparticle/homopolymer nanocomposites. *Soft Matter*. 2011;7:7914-26.
- [18] Neouze M-A, Schubert U. Surface modification and functionalization of metal and metal oxide nanoparticles by organic ligands. *Monatshefte für Chemie-Chemical Monthly*. 2008;139:183-95.
- [19] Moniruzzaman M, Winey KI. Polymer nanocomposites containing carbon nanotubes. *Macromolecules*. 2006;39:5194-205.
- [20] Barbey R, Lavanant L, Paripovic D, Schuwer N, Sugnaux C, Tugulu S, et al. Polymer brushes

via surface-initiated controlled radical polymerization: synthesis, characterization, properties, and applications. *Chemical reviews*. 2009;109:5437-527.

[21] Kim SW, Kim T, Kim YS, Choi HS, Lim HJ, Yang SJ, et al. Surface modifications for the effective dispersion of carbon nanotubes in solvents and polymers. *Carbon*. 2012;50:3-33.

[22] Li Y, Schadler LS, Benicewicz BC. Surface and particle modification via the RAFT process: approach and properties. *Handbook of RAFT polymerization*. 2008.

[23] Mehra NK, Mishra V, Jain N. A review of ligand tethered surface engineered carbon nanotubes. *Biomaterials*. 2014;35:1267-83.

[24] Starr FW, Douglas JF, Glotzer SC. Origin of particle clustering in a simulated polymer nanocomposite and its impact on rheology. *The Journal of Chemical Physics*. 2003;119:1777-88.

[25] Liu J, Gao Y, Cao D, Zhang L, Guo Z. Nanoparticle dispersion and aggregation in polymer nanocomposites: insights from molecular dynamics simulation. *Langmuir*. 2011;27:7926-33.

[26] Stöckelhuber KW, Das A, Jurk R, Heinrich G. Contribution of physico-chemical properties of interfaces on dispersibility, adhesion and flocculation of filler particles in rubber. *Polymer*. 2010;51:1954-63.

[27] Stockelhuber K, Svistkov A, Pelevin A, Heinrich G. Impact of filler surface modification on large scale mechanics of styrene butadiene/silica rubber composites. *Macromolecules*. 2011;44:4366-81.

[28] Hassinger I, Li X, Zhao H, Xu H, Huang Y, Prasad A, et al. Toward the development of a quantitative tool for predicting dispersion of nanocomposites under non-equilibrium processing conditions. *Journal of materials science*. 2016;51:4238-49.

[29] Natarajan B, Li Y, Deng H, Brinson LC, Schadler LS. Effect of interfacial energetics on dispersion and glass transition temperature in polymer nanocomposites. *Macromolecules*. 2013;46:2833-41.

[30] Natarajan B, Neely T, Rungta A, Benicewicz BC, Schadler LS. Thermomechanical properties of bimodal brush modified nanoparticle composites. *Macromolecules*. 2013;46:4909-18.

[31] Hooper JB, Schweizer KS. Contact aggregation, bridging, and steric stabilization in dense polymer–particle mixtures. *Macromolecules*. 2005;38:8858-69.

- [32] Schuster JM, Schvezov CE, Rosenberger MR. Analysis of the results of surface free energy measurement of Ti6Al4V by different methods. *Procedia Materials Science*. 2015;8:732-41.
- [33] Shafrin EG, Zisman WA. Upper limits for the contact angles of liquids on solids. *NAVAL RESEARCH LAB WASHINGTON DC*; 1963.
- [34] Gindl M, Sinn G, Gindl W, Reiterer A, Tschegg S. A comparison of different methods to calculate the surface free energy of wood using contact angle measurements. *Colloids and Surfaces A: Physicochemical and Engineering Aspects*. 2001;181:279-87.
- [35] Zhao Q, Liu Y, Abel E. Effect of temperature on the surface free energy of amorphous carbon films. *Journal of colloid and Interface Science*. 2004;280:174-83.
- [36] Wu S. Calculation of interfacial tension in polymer systems. *Journal of Polymer Science Part C: Polymer Symposia: Wiley Online Library*; 1971. p. 19-30.
- [37] Owens DK, Wendt R. Estimation of the surface free energy of polymers. *Journal of Applied Polymer Science*. 1969;13:1741-7.
- [38] Kwok D, Li D, Neumann A. Evaluation of the Lifshitz-van der Waals/acid-base approach to determine interfacial tensions. *Langmuir*. 1994;10:1323-8.
- [39] Neumann A, Good R, Hope C, Sejpal M. An equation-of-state approach to determine surface tensions of low-energy solids from contact angles. *Journal of colloid and Interface Science*. 1974;49:291-304.
- [40] Kwok D, Neumann AW. Contact angle interpretation in terms of solid surface tension. *Colloids and Surfaces A: Physicochemical and Engineering Aspects*. 2000;161:31-48.
- [41] Seidel A. *Characterization analysis of polymers: Wiley-Interscience*, 2008.
- [42] Kruželák J, Kvasničáková A, Hložeková K, Hudec I. Progress in polymers and polymer composites used as efficient materials for EMI shielding. *Nanoscale Advances*. 2021;3:123-72.
- [43] Jiang D, Murugadoss V, Wang Y, Lin J, Ding T, Wang Z, et al. Electromagnetic interference shielding polymers and nanocomposites-a review. *Polymer Reviews*. 2019;59:280-337.

CHAPTER 3 Optimizing and Analysis of Graphene Based Network nanofiller at Different Content of DGEBA/PEI Polyblends

3.1.Introduction

In the 21st century, considering the global environment, energy efficiency and renewable energy technologies, the core elements for many such fields are polymer reinforced composites and their derived products. With the rapid growth in development and usage of electronic and electrical equipment, electronic packaging of polymers has become critical. Therefore, the need for affordable multifunctional polymer materials has increased significantly.

Epoxies are highly cross-linked thermosetting polymers. One common epoxy is diglycidyl ether of bisphenol A (DGEBA), which possesses excellent corrosion resistance, outstanding adhesion strength, low curing shrinkage, and excellent mechanical properties. DGEBA is durable in harsh environments and dimensionally stable. Hence, it is widely used in coatings [1, 2] adhesives [3], supporting structural materials [4], automotive electron devices [5], and Electromagnetic interference shielding [6], several other engineering applications [7, 8]. However, this kind of structure has a few drawbacks that lead to brittle failure, low impact resistance, and poor conductivity, which limit extensive use of DGEBA epoxy resin in various engineering applications. To enhance the properties of the pristine epoxy resin, researchers generally blend it with thermoplastic polymers [9], rubber [10], or polysiloxane [11] as a modifier that can enhance energy dissipation mechanisms in the matrix. These modifications result in appreciable improvement in the toughness of the epoxy resin. However, this often causes a significant decrease in epoxy resin tensile strength, modulus, and maximum performance temperature by lowering the glass transition temperature (T_g) and does not contribute to electrical conductivity [12]. Higher energy absorption at a maximum working temperature along with electrical conductivity are important for a broad range of engineering applications.

Therefore, many nanofillers such as carbon nanotubes [13], graphene and derivatives [14], carbides [15], nitrides [16], and hybrids [17-19] have been extensively used to introduce electrical

properties in polymers due to their inherited electrical conductivity and high aspect ratios [20, 21]. Several parameters affect the electrical conductivity of polymer nanocomposites, such as interfacial resistance between filler and matrix, size and type of filler, processing conditions, and localization of filler in the matrix system. It is quite challenging to maintain a well distributed network of nanofillers in a polymer matrix, which is necessary for improving electrical conductivity. Generally, these nanofillers experience strong van der Waals forces at loadings of 1–5 wt.% reinforcement, which reduce their dispersion. Various strategies have been adopted in recent years to establish a uniform network of nanofillers in polymer composites, such as segregating the structures of polymer nanocomposites by compression molding [22-24] and reinforcing macroscopic scaffolds of nanofillers network in a polymer matrix [25-27]. However, these polymer composites are not categorized as economical multi-functional as their processing involves multiple time-consuming steps.

Another technique is selective localization of nanofillers in an immiscible polyblend with a dispersed network using a curing reaction-induced phase separation technique [28-30]. Double percolation was initially observed by Sumita et al. [31] in carbon black (CB)-filled immiscible polyblends. Thereafter, the double percolation concept was extensively applied in carbon-based materials such as graphene nanoplatelets (GNPs) [32], functional graphene oxide, carbon nanotubes (CNTs) [33], and carbon fiber (CFs) [34]. Physical mixing of polyblends can be divided into the following methods [35]: (i) mechanical mixing in rubber mills or extruders, (ii) polymerization of one monomer in the presence of another, (iii) evaporation or precipitation from a mixture of polymer solutions, and (iv) coagulation of a mixture of polymer lattices. However, polymerization in the presence of another polymer is an economical and easily controllable technique to form a low-percolation conductive network of carbon nanofillers in a multiphase polyblend. For example, Zhang et al. [36] formed a co-continuous network of epoxy (EP)/polyether sulfone (PES)/ multiwalled carbon nanotubes (MWCNTs) and selectively localized the MWCNTs in an epoxy-rich area using reaction-induced phase separation and filler localization. In the experimental study, it was found that after 20 wt.% of PES mechanical properties of polyblend increases along with high glass transition temperature (T_g). With the selective

localization of MWCNTs network (4.8 wt.%) in polyblend, the electrical conductivity increased by 450% compared to that without a PES polyblend. Luna et al. [37] studied the effects of nanoparticles on the morphologies of various immiscible polyblends and analyzed their effect of electrical properties of polyblend nanocomposites. The analytical study confirmed that reinforcement of nanofillers ensure a low thermal expansion coefficient, high thermomechanical resistance, and superior electrical conductivity if the blend exhibited a co-continuous microstructure in the fillers [38]. Huang et al. [28] used the double percolation technique to control selective localization of CNTs. They prepared a co-continuous immiscible polyblend of poly (lactic acid)/poly(ϵ -caprolactone) (PLA/PCL) at a weight ratio of 50/50 and controlled the migration of MWCNTs from unfavorable PLA to favorable PCL phase. As a result, percolation of PLA/PCL/MWCNT composites (0.97 wt.%) decreased by two orders of magnitude in PLA/MWCNT/PCL composites (0.025 wt.%) for similar electrical conductivities. Hence, development of a conductive composite is recommended with low conductive filler weight ratios and a combination of dissimilar polyblends [39-41]. When the polyblend system contains a thermosetting component, it is very difficult to control selective localization of conducting nanofillers at the interface. Generally, the fillers become concentrated in a particular phase depending on the effect of the curing reaction on miscibility, which ultimately increases the percolation threshold via dominance of a particular phase.

In this chapter, a facile approach was developed in this study to construct a conductive double percolation network of highly reduced graphene oxide (HRGO) in a polyblend of diglycidyl ether of bisphenol A/polyetherimide (DGEBA/PEI). In this technique, conductive HRGO filler was introduced into DGEBA/PEI two-phase immiscible polyblend and was selectively localized at the interface or in the co-continuous phase. The DGEBA/PEI/HRGO nanocomposite showed high electrical conductivity with a low concentration of nanofiller (i.e., 0.5 wt.%) because of its double percolation structure. Furthermore, the structural and morphological analyses of DGEBA/PEI/HRGO nanocomposites were conducted using a field emission scanning electron microscope (FESEM) and an inverted optical microscope (OM) to characterize the conductive network. The electrical conductivity of the nanocomposites was measured by using a four-point

probe technique. The effects of HRGO on the CRIPS behavior of the composites were analyzed by dynamic mechanical analysis (DMA), and the influence of HRGO on the storage modulus and T_g of the DGEBA/PEI/HRGO was analyzed in detail. This ergonomic approach and the ability to control the localization of a nanofiller network are helpful in developing an economical multifunctional polyblend of DGEBA/PEI/HRGO that can be used in various engineering applications such as electronic coatings, packaging, and electromagnetic shielding.

3.2.Experimental Section

3.2.1.Synthesis of Highly Reduced Graphene Oxide (HRGO)

The HRGO was prepared according to the method of Dang et al. [42], with some adjustments. For this, 2000 mg graphene oxide (GO, Standard Graphene, Korea) was added into a mixed solution of 800 mL N, N-dimethylformamide (DMF) and 200 mL deionized water (DIW). The mixture was sonicated in an ultrasonic bath (Jeiotech UC-10, 200 W, Seoul, Korea) for 3 h to form a homogenous suspension of GO (2 mg/mL). Hydrazine reduction was achieved by adding 5 mL of hydrazine monohydrate (98%) per 100 mL of GO suspension and stirring at 60 °C in an oil bath for 24 h. The HRGO suspensions were filtered and washed with large amounts of ethanol to remove excess hydrazine monohydrate. The HRGO filter cakes were re-dispersed in ethanol by sonication for 3 h (the temperature of the sonication bath was maintained below 30 °C).

To determine the dispersibility of HRGO in ethanol, 50 mL of HRGO suspension was centrifuged at 3000 RPM for 15 min. Then, 20 mL of the upper supernatant was collected, coagulated by adding a few drops of HCl (1 M), and filtered. The filter cakes were washed with ethanol three times, dried in vacuum at 100 °C, and weighed to calculate the dispersibility of the HRGO.

3.2.2.Preparation of DGEBA/PEI/HRGO Composites

Composites with and without HRGO were prepared by using following process. First, DGEBA, PEI, and HRGO were weighed according to the formulations in Table 3.1 and DGEBA/PEI/HRGO composites were denoted by DPxH. Where D, P, x, and H were representing the DGEBA, the PEI, PEI parts per hundred in the DGEBA (phr), and 0.5 wt.% of HRGO, respectively. PEI was dissolved in methylene dichloride (CH_2Cl_2) with strong magnetic stirring

and was introduced into the HRGO solution via magnetic stirring at room temperature. After that, the DGEBA was added to the PEI/HRGO blends with high-speed magnetic stirring at 80 °C for 2 h to remove the solvent from the mixture. Then, the blends of DGEBA/PEI/HRGO were placed in a vacuum oven at 120 °C for 12 h to degas the mixtures and to remove the solvents. The mixture of curing agent Me-THPA and accelerator DMBA at 400:1 ratio by weight (C-A solution) was added into the vacuum-removed blends and stirred at 550 RPM and 120 °C. The homogeneous blend was achieved by mixing, and the few air bubbles caused by these processes were removed through vacuum treatment at 120 °C for 10 min. Finally, the polyblends were pre-curing at 150 °C for 5 h and continued by post-curing at 200 °C for 2 h after pouring into the pre-prepared mold (Figure 3.1). The residual samples in the beaker were stored in a refrigerator for OM measurement. For comparison, neat DGEBA, DP5, DP10, DP15, DP20, DP25, and DP30 were prepared by the same process.

Table 3.1. Formulation of samples.

Sample	DGEBA (phr) ¹	PEI (phr) ¹	HRGO (wt.%)	C–A solution
DGEBA	100	0	0	80
DP0H	100	0	$x/(100 + 0+x)= 0.5\%$	80
DP5H	100	5	$x/(100 + 5+x)= 0.5\%$	80
DP10H	100	10	$x/(100 + 10+x)= 0.5\%$	80
DP15H	100	15	$x/(100 + 15+x)= 0.5\%$	80
DP20H	100	20	$x/(100 + 20+x)= 0.5\%$	80
DP25H	100	25	$x/(100 + 25+x)= 0.5\%$	80
DP30H	100	30	$x/(100 + 30) \times 0.5\%$	80

¹phr: parts per hundred in the DGEBA, x: HRGO (phr), C-A solution: a solution of Me-THPA and DMBA.

3.2.3.Measurement and Characterization

Optical microscopy (OM) measurements were performed on an inverted metallurgical microscope (DMI3000B, Leica, Seoul, Korea) to observe the phase separation behavior and double percolation structure. Scanning electron microscope (SEM) (S-3400N, Hitachi High-Technologies, Chicago, USA) analyses were conducted to observe the morphology of the HRGO. Transmission electron microscopy (TEM) measurements were performed on a field emission transmission electron microscope (Tecnai G2 F20 X-Twin, FEI Co., Hillsboro, USA) operated at an acceleration voltage of 200 kV. The ultrathin film (thickness:100–200 nm) composite samples were prepared at room temperature using an ultramicrotome (RMC CR-X, Boeckeler Instruments, Arizona, USA) equipped with a glass knife. The volume resistivity and volume conductivity of

nanocomposites were measured at room temperature using a four-point probe technique with (CMT-100, AIT Co., Gyeonggi, Korea). Nanocomposites were prepared in a disk shape (approximately 40 mm diameter and 2 mm thickness) for conductivity measurements (Figure 3.1). The thermomechanical properties of the nanocomposites were performed by dynamic mechanical analysis (DMA) (TA Q800, TA instrument, New Castle, USA) in single cantilever mode at a frequency of 1 Hz and oscillation strain of 0.2. The temperature ranges were 30–180 °C and 30–230 °C at a heating rate of 3 °C/min for the neat DGEBA and other nanocomposites, respectively. The samples were cast in square aluminum molds, yielding a specimen geometry of 45 mm × 10 mm × 3 mm (Figure 3.1). The contact angle (CA) measurements of DGEBA, PEI, and HRGO films with various liquids were measured using a (Phoenix 300, SEO, Komachine Co., Seoul, Korea). The CA measurements were conducted using the sessile drop method at room temperature with 15–17 μ L volume drops of liquids that were prepared with a microsyringe. The surface tension and polarity of deionized water, glycerol, and formamide are shown in Table 3.1. The Raman spectra were characterized using a confocal Raman microscope (Thermo Fisher Scientific, Seoul, Korea) with a 532 nm wavelength monochromatic excitation laser with 2 mW laser power and a 5 s exposure time. Furthermore, Fourier transform infrared (FT-IR) spectra were recorded using (FT-IR, Thermo Fisher Electron Co., Waltham, MA, USA). Differential scanning calorimeter (DSC) measurements were performed by (TA Q20 V24.10, TA instrument, New Castle, USA).

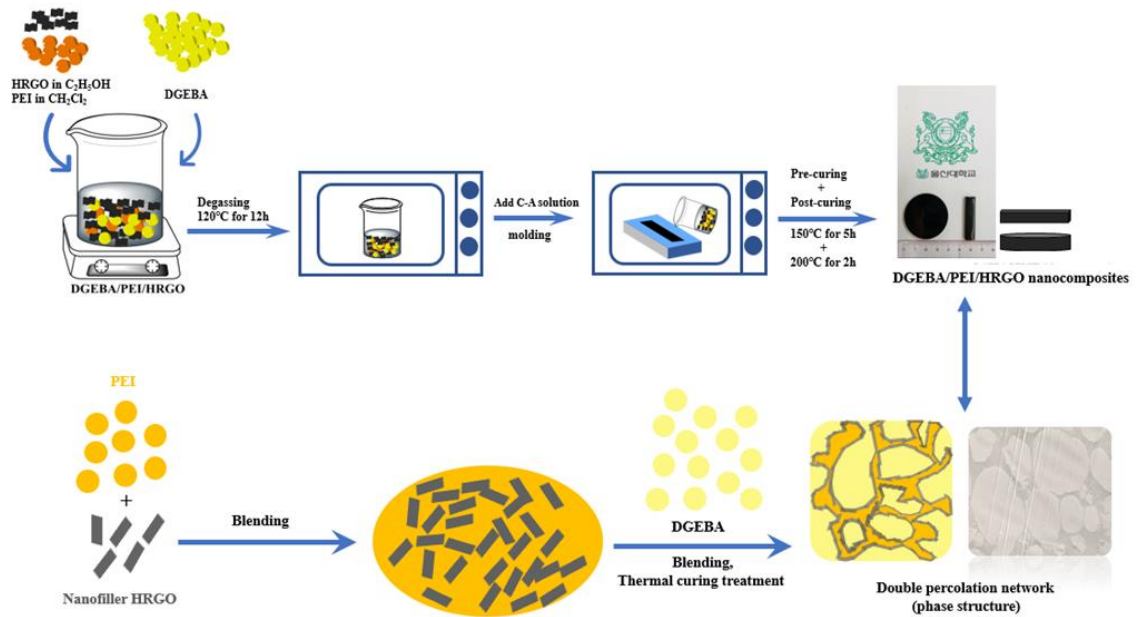


Figure 3.1. Schematic illustration of preparation of DGEBA/PEI/HRGO polyblend nanocomposites and the phase structure during the process.

3.3. Results and Discussion

3.3.1. Physical and Morphological Properties of HRGO

A low-magnification SEM micrograph of an HRGO flake is shown in Figure 3.2a. GO is a 2D sheet-like structure and contains multiple lamellar layers that open into a few layers with improved graphitic structure after reduction. Figure 3.2a represents the opened flakes of graphene layers with irregular and folding which is caused due to acid treatment. They are entangled with each other and helpful in creating a dispersed network by selective localization while reinforcing the polyblend. Figure 3.2b shows a TEM image of single- or few-layer HRGO nanosheets with many wrinkles. These kinds of 2D wrinkled structures are useful in improving the reinforcement efficiency of HRGO. However, it is very difficult to predict the actual changes in structure after reduction from these SEM and TEM analyses. Therefore, Raman analysis was also conducted on these before reinforcement.

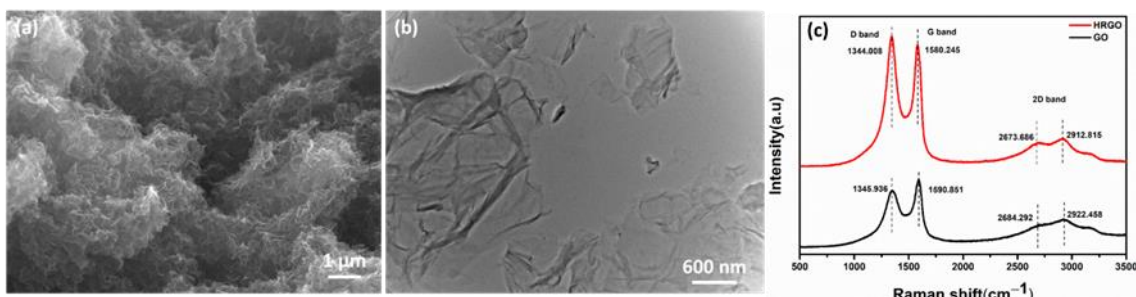


Figure 3.2. (a) SEM micrograph of HRGO flakes after drying, (b) TEM micrograph of HRGO and (c) Raman spectra of GO and HRGO flakes.

Raman spectroscopy provides information based on inelastic scattering of a molecule irradiated by a monochromatic light, where laser is normally used. Figure 3.2c shows Raman spectra for GO and HRGO, with two fundamental vibrations observed in the range of 1100–1700 cm^{-1} . The D vibration band (D-band) was observed at 1345.9 cm^{-1} and 1344.008 cm^{-1} for GO and HRGO, respectively. On the other hand, the G vibration band (G-band) appeared at 1590.8 cm^{-1} and 1586.5 cm^{-1} for GO and HRGO, respectively. Furthermore, the G vibration band is affected by the presence of the stretching C–C bond, which is common in all sp^2 carbon systems. The D band and G band in the Raman spectra symbolize disorder bands and tangential bands, respectively. Besides, a broadening and shift to higher wavenumbers of the 2D band were observed at 2684.2 cm^{-1} and 2673.6 cm^{-1} for GO and HRGO, respectively. The 2D band can be used to determine number of layers of graphene (monolayer, double layer, or multilayer) as it is highly sensitive to the stacking of graphene layers. In addition, the shifted location of the 2D band is due to the presence of oxygen-containing functional groups and prevents graphene layer stacking of HRGO. Thus, fewer oxygen-containing functional groups remained, allowing the HRGO to stack. The ID/IG ratio for GO was 0.847. After reduction, the ratio for HRGO increased to 1.063 due to restoration of sp^2 carbon and decrease in the average size of sp^2 domains upon reduction [43,44]. The higher intensity in the D band also suggested that more isolated graphene domains were present in HRGO compared to GO due to removal of oxygen moieties from GO after hydrazine reduction [45,46]. Further, to observe the reduction state of HRGO, FT-IR analysis was also conducted. Figure 3.3 represents the FT-IR spectra of GO and HRGO, which confirms the reduction of GO after hydrazine treatment. After reduction of GO, a new amino group from hydrazine was found in HRGO which helped accelerating the curing reaction process.

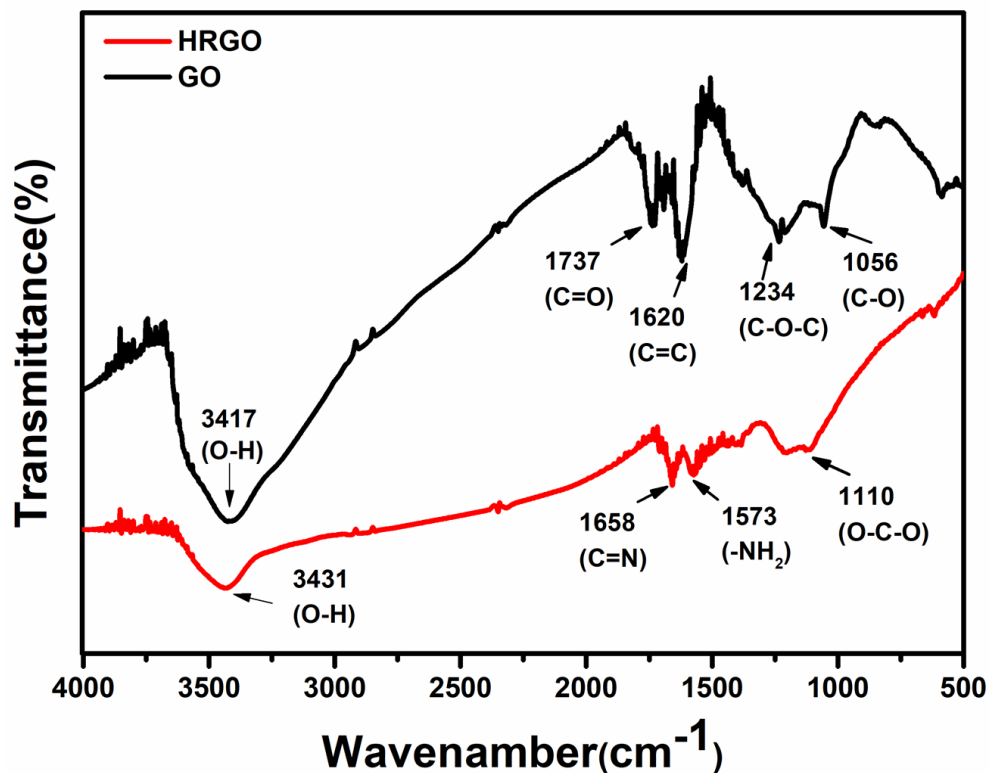


Figure 3.3. The FTIR spectra for HRGO and GO.

3.3.2. Morphology of DGEBA/PEI/HRGO as Observed by Optical Microscopy (OM) Measurement

Curing reaction-induced phase separation (CRIPS) is commonly described as the separation of a homogeneous polyblend into two immiscible phases during curing. The morphologies of the fabricated DGEBA/PEI/HRGO nanocomposites with different contents of PEI were characterized by OM measurement (Figure 3.4). During the CRIPS process, the polyblend followed a spinodal decomposition mechanism [42]. The DGEBA/PEI polyblend is a dynamic asymmetric system that initially is homogeneous. The molar mass of the DGEBA increases as the isothermal curing reaction proceeds, resulting in an increase in cross-linking density of DGEBA. Because large differences in mobility occur between DGEBA molecular and PEI, the PEI is no longer miscible in the matrix, and PEI begins to separate out, causing phase separation. The viscoelastic effect become more prominent after primary phase separation, and this reduces the mobility of polymer chains of each polymer as they diffuse into each other. When the diffusion is too slow to achieve geometrical coarsening, the local concentration equilibrium is disrupted, and secondary phase

separation will occur in both DGEBA-rich and PEI-rich domains [43].

Figure 3.4a–g shows the final phase of the DGEBA/PEI/HRGO nanocomposites with various PEI contents. The final phase structure changed from a Figure 3.4a-like insulated island dispersed phase structure to a Figure 3.4e micro-size co-continuous phase structure, with a PEI concentration from 5 to 25 phr of DGEBA, respectively. Furthermore, an inversion phase structure (PEI-rich phase as matrix) appeared in the polyblend with increased concentration of PEI, as depicted in Figure 3.4f.

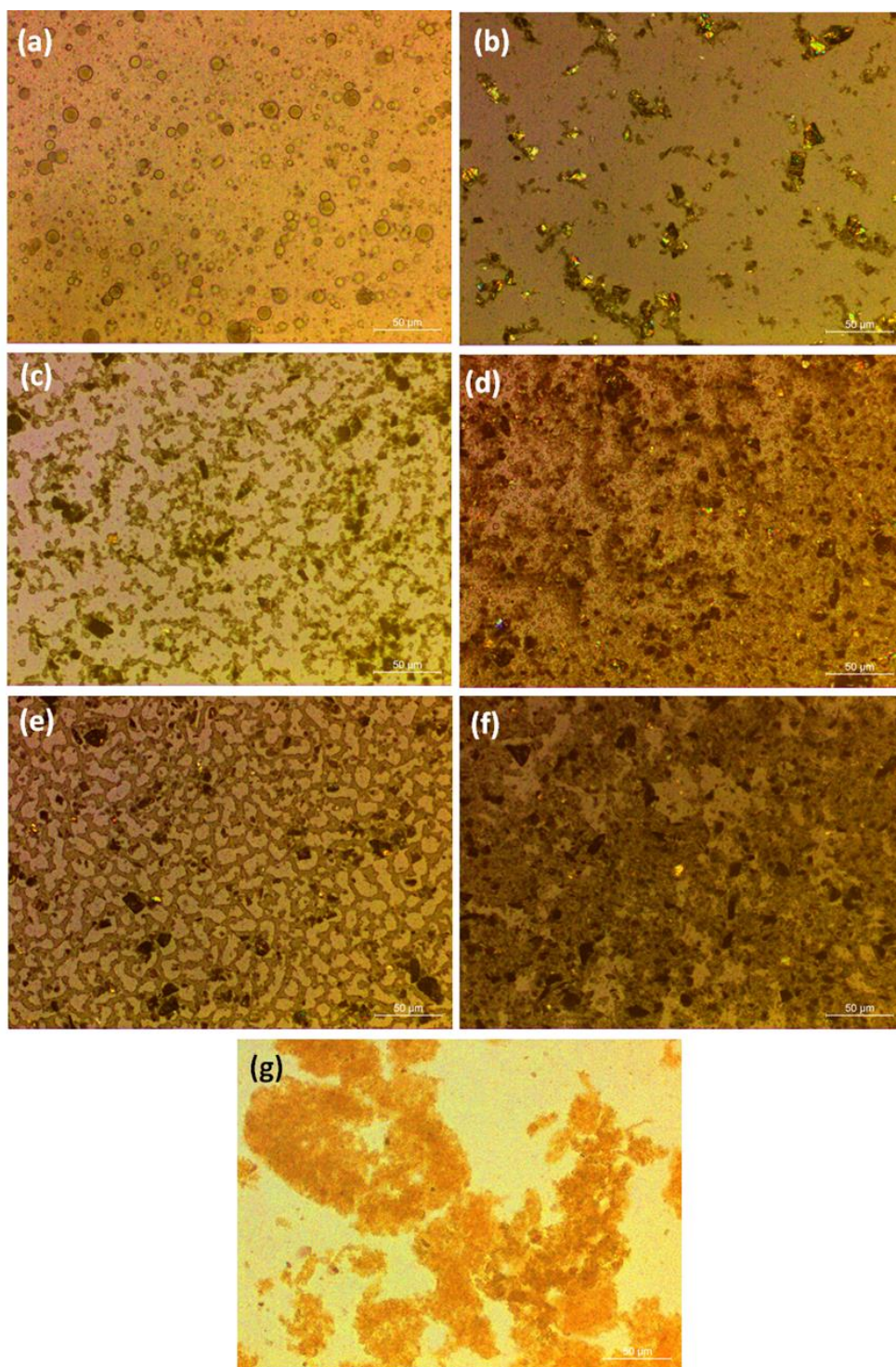


Figure 3.4. The final phase morphologies of DGEBA/PEI/HRGO nanocomposites are (a) DP5H, (b) DP10H, (c) DP15H, (d) DP20H, (e) DP25H, (f) DP30H, and (g) DP30, respectively.

The PEI-rich phase is represented as darker domains, and the DGEBA-rich phase as brighter domains (Figure 3.4f). further, these separated phases were confirmed by FETEM analyses in the upcoming section. Occurrence of secondary phase separation, which shows many small droplets in both domains at the final stage of phase separation, as in Figure 3.4e–g, concur well with the

state of viscoelastic phase separation reported by Tanaka et al. [44].

Compared with the non-HRGO-filled polyblend in Figure 3.4g, introduction of the HRGO (Figure 3.4f) both suppressed the extent of coarsening (i.e., the sizes of the DGEBA-rich phases became smaller) and accelerated the curing process due to interactions between -NH₂ functional groups on the HRGO and DGEBA oligomer [45]. HRGO served as a crosslinking accelerator as a chemical crosslinking point.

3.3.3. Field Emission Transmission Electron Microscopy (FETEM) Analyses

The distribution of HRGO in DGEBA/PEI polyblend system and the phase structure of polyblend were analyzed by the FETEM technique as well. Figure 3.5 represents the FETEM micrographs of the DP25H and DP30H polyblends, in which dark and white domains represent PEI and DGEBA phase, respectively. Figure 3.5a shows a co-continuous phase morphology in low magnification which is consistent with the optical micrographs and Figure 3.5b shows the crumpled surfaces (with some wrinkles) of sheets of HRGO at the interface (between DGEBA and PEI phase). It is implied that the HRGO sheets were selectively localized at the interface in DP25H. Then, the high-resolution transmission electron microscopy (HRTEM) image of DP25H exhibits fringes from which the d-spacing value of the HRGO was calculated to be 0.376 nm as depicted in Figure 3.5c. Figure 3.5d–f represents a typical phase inversion structure of DP30H polyblend from lower to higher magnifications. The secondary phase separation structure showed in Figure 3.5e, involved many dark insulated islands (PEI phase) and numerous crumpled HRGO sheets distributed at the interface that between DGEBA and PEI phase.

Comparing Figure 3.5a with Figure 3.5d, we observe the formation of different phase structures by increasing the content of PEI from 25 to 30 phr. Meanwhile, the FETEM analysis is coherent with the OM micrographs and represents localization of HRGO at the interface between DGEBA and PEI successfully.

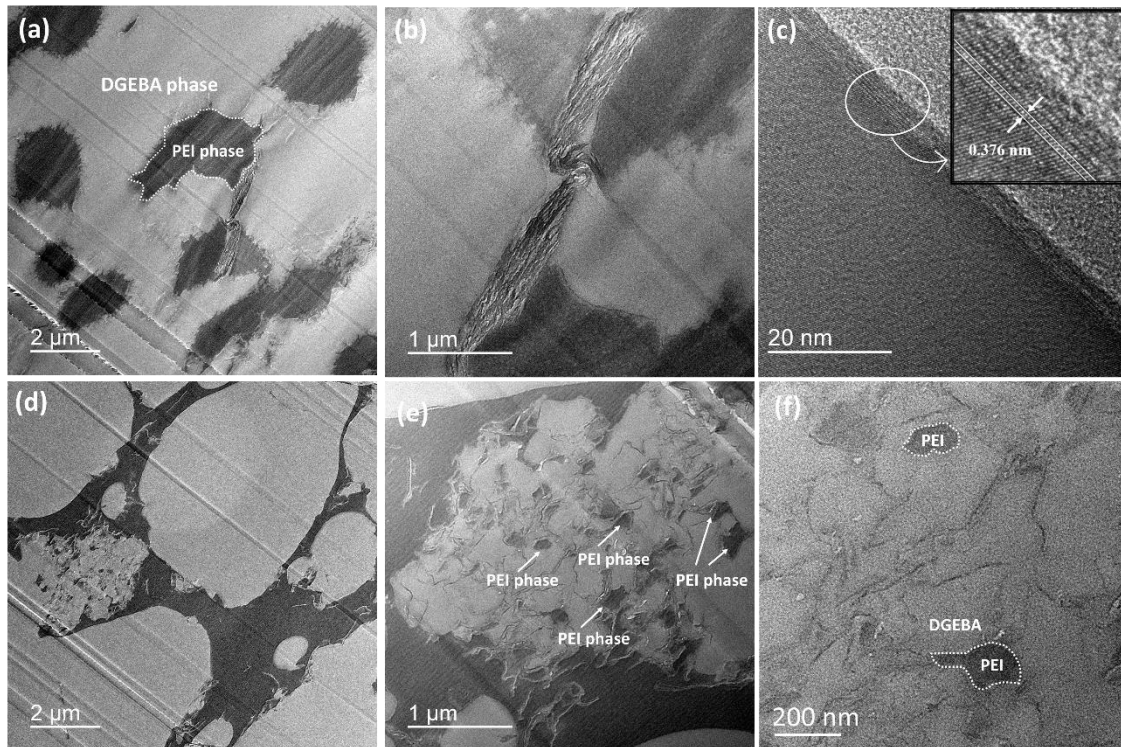


Figure 3.5. FETEM micrographs of (a–c) DP25H polyblend from lower to higher magnification with inset in (c) represents HRTEM micrograph of localized HRGO at the interface of DGEBA and PEI, and (d–f) represents DP30H polyblend with phase inversion.

3.3.4. Electrical Properties of Nanocomposites

Morphologic analyses of DP25H and DP30H demonstrated the existence of a co-continuous phase and an inversion phase, respectively. HRGO was selectively located at the interface between DGEBA and the PEI phase and formed a double-percolation conductive network structure. This dispersed network in polyblend is useful in introducing conductivity to a composite system. Figure 3.6 illustrates the effects of PEI content and PEI/HRGO content on the in-plane conductivity of polyblend and HRGO-reinforced polyblend composites, respectively. Figure 3.6b shows that the electrical conductivities gradually increased by increasing the PEI content when HRGO was introduced into the DGEBA/PEI polyblend system. On the other hand, there was little change in the electrical conductivity of polyblend without HRGO, as represented in Figure 3.6a.

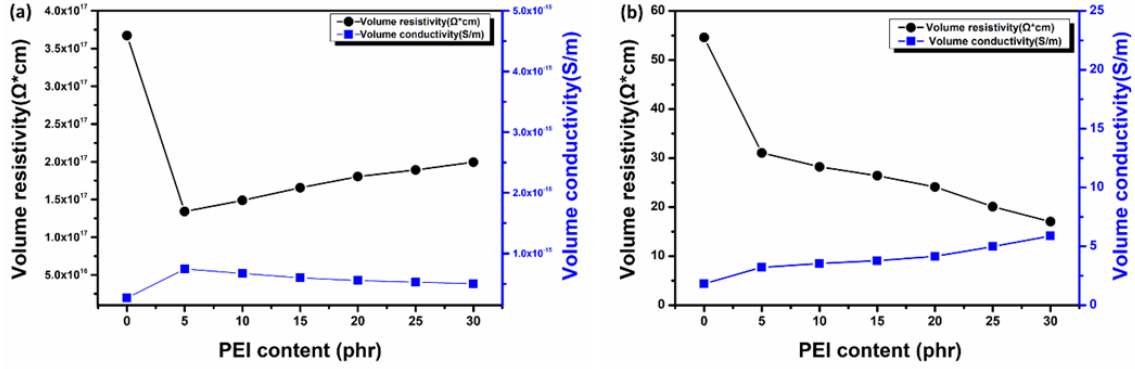


Figure 3.6. The electrical properties of samples for various PEI contents: (a) DGEBA/PEI, (b) DGEBA/PEI/0.5 wt.% HRGO.

However, the phase morphologies of the nanocomposites, especially phase continuity, play an important role in establishing a conductive network of filler in polymer composites. The volume resistivity and conductivity of DGEBA with similar concentrations of PEI and 0.5 wt.% HRGO are presented in Figure 3.6b and Table 3.2. With HRGO reinforcement in DGEBA, the conductivity reached 1.83 S/m, and it increased with respect to PEI concentration increases. In the DP25H, the conductivity reached ~ 5 S/m, an overall improvement of 173% compared to that without PEI. After reaching 25 phr of PEI, the conductivity remained nearly constant, but an inversion phase structure affected the thermomechanical properties of the overall polyblend system. Furthermore, the comparison of electrical properties with other previous reports are shown in Table 3.3.

Table 3.2. The volume resistivity and volume conductivity of DGEBA/PEI polyblend with and without HRGO.

Materials	Volume Resistivity ($\Omega \text{ cm}$)	Volume Conductivity (S/m)
Neat DGEBA	3.67×10^{17}	2.67×10^{-16}
DP0H	54.60	1.83
DP5H	31.06	3.22
DP10H	28.23	3.54
DP15H	26.41	3.78
DP20H	24.11	4.15
DP25H	20.09	4.98
DP30H	17.02	5.88

The simultaneous blending of PEI with the curing reaction causes phase separation due to a spinodal shift, allowing formation of a co-continuous network structure. This network improves the dispersion state of HRGO and improves the conductivity. This conducting property of nanocomposites is determined by selective localization of filler particles in the polyblend. There

are various thermodynamic strategies to control the selective localization of nanofiller. The most widely used thermodynamic parameters for localization are the wetting parameters, which are described in an upcoming section [36].

Table 3.3. Comparison of electrical properties with those of previously publications.

Samples	Polymer A	Polymer B	Filler Loading (wt. %)	Volume Resistivity ($\Omega \cdot \text{cm}$)	Volume Conductivity (S/m)	[Ref]
EP/35PEI/GnPs	DGEBA	PEI	2	$\approx 10^7$	$\approx 10^{-5}$	[46]
EP/PES/MWCNT	DGEBA	PES	4.8	—	10^{-1}	[36]
EP/PEI/CB	DGEBA	PEI	1	$\approx 10^3$	—	[47]
DGEBA/PEI/MWCNTs	DGEBA	PEI	2	3.86×10^6 $9.6 \times 10^5 \Omega$	—	[48]
DGEBA/PEI/AgNWs	DGEBA	PEI	3	(surface resistivity)	—	[49]
EP/AlN/MWCNTs	DGEBA	AlN	6	—	10^{-10}	[50]
EP/PA/MWCNT	DGEBA	PA	1	—	10^{-3}	[51]
DGEBA/PEI/HRGO	DGEBA	PEI	0.5	1.7×10^1	5.88	This work

3.3.5. Prediction for Selective Localization of HRGO

Various studies of different complex parameters have been conducted for localization of a filler in an immiscible polyblend. Accurate analysis of localization is difficult because, in addition to thermodynamics, the fluid dynamics, surface tension, and polarity of constituent blends during reaction are very important [56–61]. However, still wettability parameter is a useful technique as it considers the surface tension of each component in the blend. To precisely evaluate the surface tension of DGEBA, PEI, and HRGO, we conducted contact angle measurements in conjunction with the Lifshitz–van der Waals/acid-base approaches (Equations (1) and (2)) [56,57]. The values of these surface tension components and parameters of the test liquids used in this work are shown in Table 3.4. Digital images of the contact angles and values of three components are shown in Figure 3.7 and Table 3.5.

Table 3.4. Surface tensions and components (mJ/m^2).

Liquid	γ_L	$\gamma_L^{\text{LW}}(\gamma_L^{\text{d}})$	$\gamma_L^{\text{AB}}(\gamma_L^{\text{p}})$	γ_L^+	γ_L^-	Polarity [$\gamma_L^{\text{p}}/\gamma_L^{\text{d}}$]
Deionized water (DI)	72.8	21.8	51	25.5	25.5	2.3
Glycerol (GL)	64.0	34.0	30	3.9	57.4	0.9
Formamide (FA)	58.0	39.0	19	2.28	39.6	0.5

$$\gamma_L(1 + \cos \theta) = 2\left(\sqrt{\gamma_s^{\text{LW}} \gamma_L^{\text{LW}}} + \sqrt{\gamma_s^+ \cdot \gamma_L^-} + \sqrt{\gamma_s^- \cdot \gamma_L^+}\right) \quad (3.1)$$

$$\gamma_L^{AB} = 2\sqrt{\gamma_L^- \cdot \gamma_L^+} \quad (3.2)$$

The Lifshitz–van der Waals/acid-base approaches proposed by Van Oss et al. [52, 53] combine dispersion (γ^d), polar (γ^p), and γ^i components into a single component, called the nonpolar or Lifshitz–van der Waals component (γ^{LW}). Also, the electron acceptor–electron donor (Lewis acid/base) interactions of polar composites are expressed as γ^{AB} , and the surface tension of compound i (L: liquid, S: solid) is expressed as γ_i^+ (acidic component) γ_i^- (basic component) according to Equation (2). Eventually, the total surface tension is obtained by addition of the nonpolar and polar components ($\gamma^{\text{tot}} = \gamma^{LW} + \gamma^{AB}$). Combining this method with the Young–Dupré equation yields Equation (1).

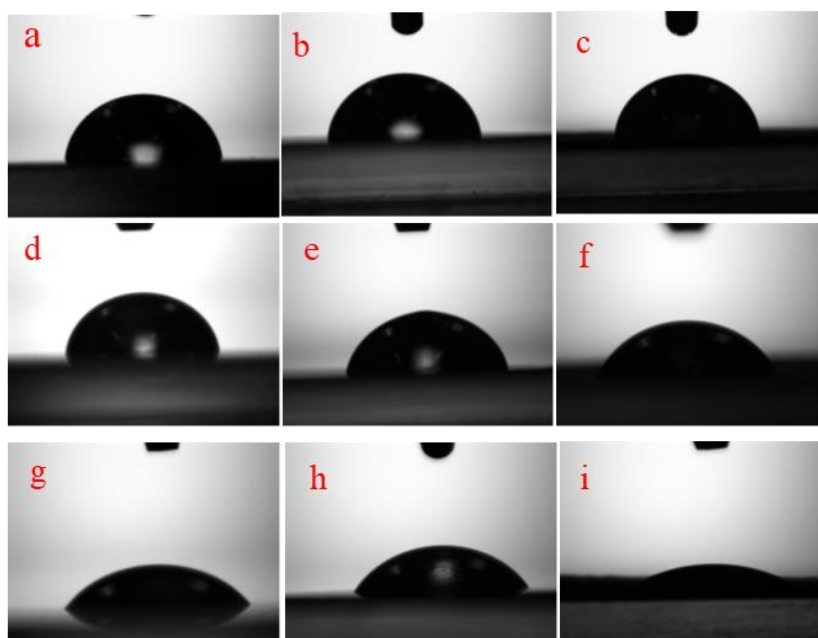


Figure 3.7. The contact angle images of samples are given in Table 3.5. (a) DI on DGEBA, (b) DI on PEI, (c) DI on HRGO, (d) GL on DGEBA, (e) GL on PEI, (f) GL on HRGO, (g) FA on DGEBA, (h) FA on PEI, (i) FA on HRGO.

Since Equation (1) contains three unknowns of the solid (γ_s^{LW} , γ_s^+ , and γ_s^-), we used three different liquids (in Table 3.5), two of which were polar. In our work, the surface tensions of DGEBA, PEI, and HRGO were calculated by Lifshitz–van der Waals approaches as shown in Table 3.6.

Table 3.5. Surface tension components and parameters and static contact angles for the test liquids DGEBA, PEI, and HRGO.

Liquid	γ_L	$\gamma_L^{LW}(\gamma_L^d)$	$\gamma_L^{AB}(\gamma_L^p)$	Contact Angle (θ)
--------	------------	-----------------------------	-----------------------------	----------------------------

	(mJ/m ²)	(mJ/m ²)	(mJ/m ²)	DGEBA	PEI	HRGO
Deionized water (DI)	72.8	21.8	51	88.4	84.2	80.5
Glycerol (GL)	64.0	34.0	30	84.3	75.0	55.0
Formamide (FA)	58.0	39.0	19	54.1	58.8	27.1

The surface tension of each component in the polyblend is considered essential for predicting the localization. From a thermodynamics perspective, the wetting coefficient (ω_a) proposed by Sumita et al. [54] was widely used to forecast the localization of nanofillers [51,63,64]. The wetting coefficient ω_a can be calculated according to Young's equation (Equation (3)) as given below:

$$\omega_a = \frac{\gamma_{\text{HRGO-B}} - \gamma_{\text{HRGO-A}}}{\gamma_{\text{A-B}}} \quad (3.3)$$

where $\gamma_{\text{HRGO-B}}$ is the interfacial tension between HRGO and the polymer B phase, $\gamma_{\text{HRGO-A}}$ is the interfacial tension between HRGO and the polymer A phase, and $\gamma_{\text{A-B}}$ is the interfacial tension between the polymer A phase and polymer B phase. The prediction is that HRGO will be distributed preferentially in the polymer B phase if $\omega_a < -1$, HRGO will be located at the interface between polymer A and polymer B if $-1 < \omega_a < 1$ and HRGO will be distributed in the polymer A phase if $\omega_a > 1$.

Table 3.6. The surface tension parameters were obtained from Table 3.5.

Materials	γ (mJ/m ²)	γ^d (mJ/m ²)	γ^p (mJ/m ²)
DGEBA	103.79	92.44	11.35
PEI	131.68	126.62	5.06
HRGO	93.99	93.67	0.32

HRGO: highly reduced graphene oxide; PEI: polyetherimide; $\gamma = \gamma^d + \gamma^p$.

The interfacial tension between the two phases of nanocomposites, $\gamma_{\text{A-B}}$, can be calculated using Wu's harmonic mean average [55] as follow:

$$\gamma_{\text{A-B}} = \gamma_A + \gamma_B - 4 \left(\frac{\gamma_A^d \gamma_B^d}{\gamma_A^d + \gamma_B^d} + \frac{\gamma_A^p \gamma_B^p}{\gamma_A^p + \gamma_B^p} \right) \quad (3.4)$$

where $\gamma_{\text{A-B}}$ is the interfacial tension between phases A and B. γ_A and γ_B are the surface tensions of phases A and B, respectively. γ_A^d and γ_B^d are the surface tensions of dispersion components A and B, respectively. γ_A^p and γ_B^p are the surface tensions of polar components A and B, respectively, for which $\gamma = \gamma^d + \gamma^p$.

In our DGEBA/PEI/HRGO polyblend system, the surface tensions of components are shown in

Table 3.6, and the interfacial tension and calculated wetting coefficient are given in Table 3.7. From these calculations $-1 < \omega_a = 0.171 < 1$, indicating that the HRGO selectively localizes at the interface in DGEBA/PEI/HRGO systems. This prediction is consistent with the OM images.

Table 3.7. The wetting coefficient (ω_a), interfacial tension (γ_{pair}), and predicted localization of HRGO in DGEBA/PEI/HRGO polyblends.

Nanocomposites	Phase A	Phase B	Component Pair	γ_{pair} (mN/m)	ω_a	Predicted Localization of HRGO
DGEBA/PEI/HRGO	DGEBA	PEI	DGEBA/PEI	7.74	$-1 < 0.171 < 1$	Interphase
			DGEBA/HRGO	10.42		
			PEI/HRGO	9.10		

3.3.6. Mechanism of HRGO Localization

Considering the final electrical properties of the ternary nanocomposites, selective localization of nanofiller in a polyblend is the key factor for controlling these properties. Introducing the electrical conductivity with very low filler content is very important. In creation of polyblend, crosslinking of DGEBA begins once the temperature increases to the curing temperature, and this is the starting point for phase separation [56, 57]. As curing continues, the spinodal downshift led to formation of a co-continuous phase structure. The HRGO nanoparticles were uniformly mixed in the polyblend (Figure 3.8). During curing of DGEBA, an island-like structure is formed and progressively increases until the dynamic forces between DGEBA and PEI are in balance. Here, HRGO nanoparticles due to double percolation formed a conductive network at the interphase of DGBEA and PEI, as represented in Figure 3.8a,b.

Figure 3.8b presents the TEM micrograph of DP25H nanocomposites in which the two phases of DGEBA and PEI are represented by yellow and orange color dots, respectively. The HRGO particles are clearly visible at the interphase of the two polymers, forming a conductive network in the polyblend at a very low concentration. Table 3.3 compares our work with previous literature, showing high electrical properties in comparison with others work. Moreover, the content ratio of nanofiller HRGO in our work is very low (only 0.5 wt.% of filler) for achieving the similar or more electrical conductivity compared to others work.

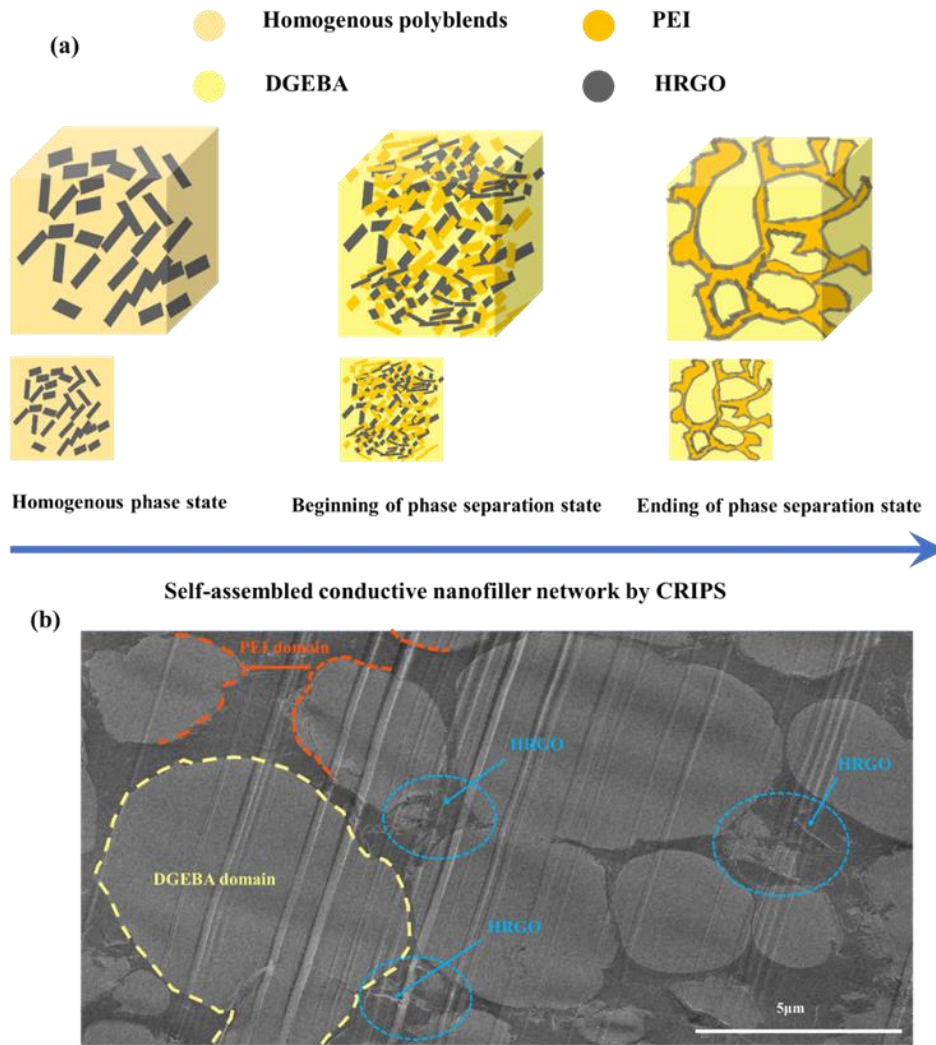


Figure 3.8. Schematic illustration: (a) structural evolution of double percolation conductive DGEBA/PEI/HRGO nanocomposites via CRIPS and (b) FETEM image of nanocomposite.

3.3.7. Dynamic Mechanical Analyses (DMA)

The viscoelastic behavior of HRGO-reinforced polyblends and selective localization of HRGOs in nanocomposites have been studied using dynamic mechanical analysis (DMA). DMA provides a sinusoidal load over the clamped sample and compares this with the collected response using a linear variable differential transformer (LVDT). Specifically, the LVDT measures the amplitude of the resulting sinusoidal wave, which is the storage modulus (E') of the material, and the tangent of the phase lag between applied force and material response ($\tan \delta$) [13].

Figure 3.9a–d presents the storage modulus versus temperature curve of the DGEBA/PEI polyblend with various phr of PEI and that of the DGEBA/PEI/HRGO nanocomposite with various phr of PEI and a fixed concentration of HRGO (0.5 wt.%).

Figure 3.9a presents the storage modulus of a polyblend without HRGO. The storage modulus of neat DGEBA is 1536 MPa in the glassy region (measured at 30 °C) and 14.2 in the rubbery region (measured at $T_g + 30$ °C). The storage modulus increased with PEI and reached maximum values of 1660 MPa and 68 MPa in the glassy and rubbery regions, respectively, for 25 phr PEI. The storage modulus of DP25 was higher for the entire working temperature range (30–180 °C), which suggests that the restriction of polymer chains in the polyblend is primarily due to phase separation but also to arrested motion of the thermoplastic monomer chain between DGEBA-rich zones. Figure 3.9b shows curves of the storage modulus in the temperature range of 80–130 °C, and it clearly indicates the restriction of polymer chain motion at the beginning of the transition zone (glassy to rubbery). Ultimately, the immiscible polymer blending resulted in a binary polymer system that is capable of withstanding higher temperatures than that of DGEBA alone.

Figure 3.9c and Table 3.8 show the effect of reinforcement of HRGO on the thermomechanical properties of DGEBA/PEI/HRGO nanocomposites with different phr fractions of PEI and a fixed weight ratio of HRGO. The storage moduli of ternary polyblend nanocomposites increased with increasing PEI concentration. The storage modulus of DP25H reached 1915 MPa and 64.8 MPa in the glassy and rubbery regions, respectively, and showed an overall improvement of ~14% and ~222% over the baseline DGEBA nanocomposite (i.e., without polyblend DP0H). The HRGO reinforcement in polyblend played a crucial role in improving the thermomechanical properties, as depicted in Figure 3.9d. Although the storage modulus is high for the entire temperature range in DP25H, the effect is more prominent at the beginning of transition (i.e., 80–130 °C), where there was a significant difference in the storage.

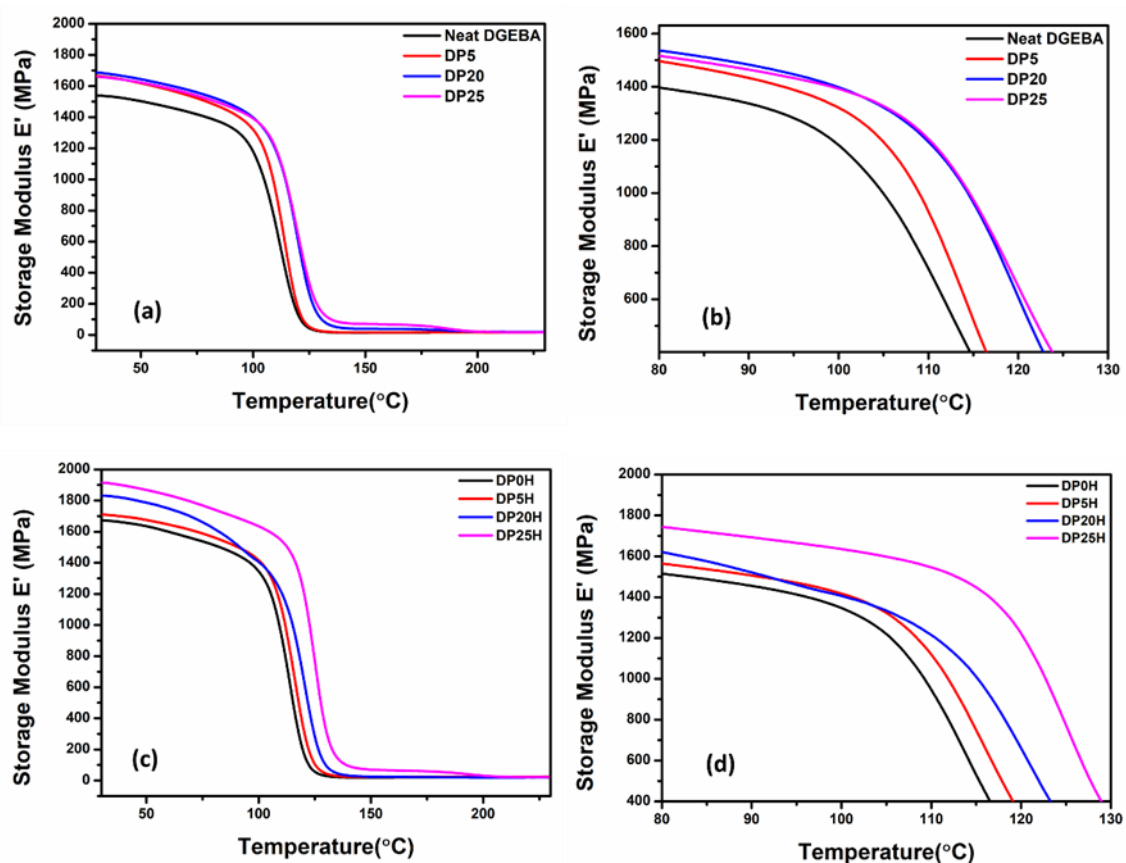


Figure 3.9. The storage modulus versus temperature of DGEBA/PEI polyblend (a) at 30–230 °C and (b) a magnified view of the beginning of the transition (80–130 °C). Storage modulus versus temperature curves for DGEBA/PEI/HRGO nanocomposites with 0.5 wt.% HRGO at (c) 30–230 °C and (d) 80–130 °C.

Tan δ versus temperature curves of DGEBA/PEI polyblend and DGEBA/PEI/HRGO nanocomposites are given in Figure 3.10. The curves in Figure 3.10a–c demonstrate that the glass transition temperature (T_g) increased with blending concentration of PEI. The T_g of base DGEBA was 123.1 °C. After blending with PEI, it increased to 133.8 °C for DP25, an improvement of 10.7 degrees (T_{g1} in Table 3.8). On the other hand, the T_g of neat PEI was 217 °C, which was reduced after blending with DGEBA (T_{g2} in Table 3.8). The T_{g2} of the DP25 was 192 °C. When HRGO was added to the polyblend, the T_{g2} showed similar results (Figure 3.10d–f). The T_{g1} of DP25H reached 131.6 °C, which is close to the T_{g1} of DP25 but higher than that of DGEBA/0.5HRGO (123.3 °C). The T_{g2} of DP25H was 198.2 °C, higher than that of DP25 (192.0 °C). This implies that addition of HRGO in the polyblend restricts polymer chain motion of both DGEBA and PEI. However, it is more prominent for PEI, as it exists only at the narrow zones between the large islands of DGEBA created during phase separation. The decrease in peak

height of $\tan \delta$ in polyblend (Figure 3.10b) and nanocomposite (Figure 3.10e) indicates the change in internal energy due to restriction of molecular mobility caused by the increase in viscosity due to PEI and HRGO fillers, respectively [58, 59].

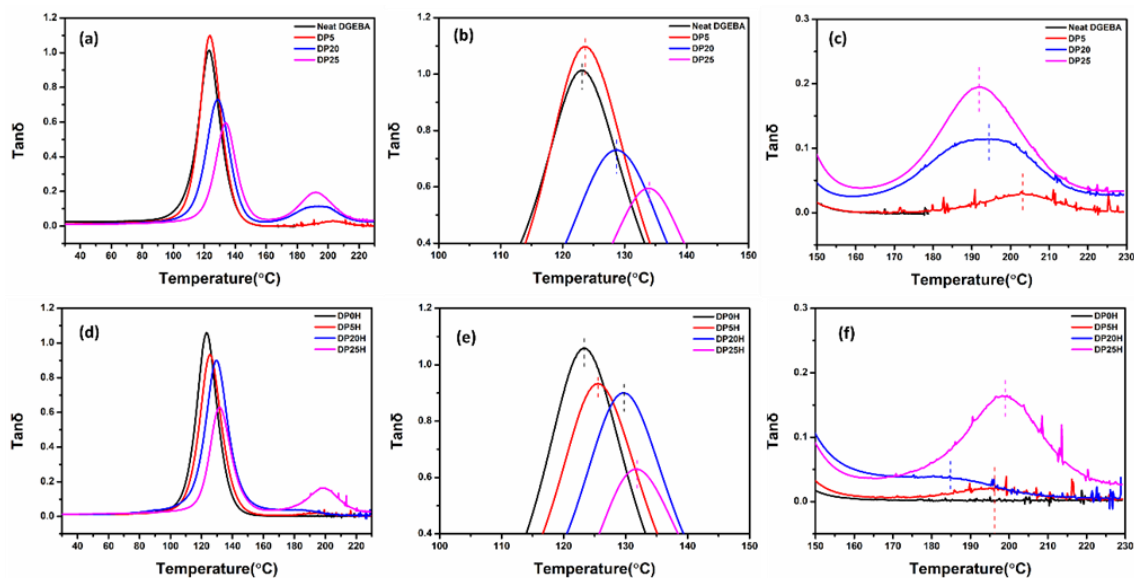


Figure 3.10. $\tan \delta$ versus temperature curve for DGEBA/PEI polyblend: (a) 30–230 °C, (b) 100–150 °C for T_{g1} , (c) 150–230 °C for T_{g2} , and $\tan \delta$ versus temperature curve for DGEBA/PEI/HRGO nanocomposites: (d) 30–230 °C, (e) 100–150 °C for T_{g1} , (f) 150–230 °C for T_{g2} .

Table 3.8. The storage, rubbery modulus, and T_g (from $\tan \delta$) of samples.

Materials	Storage Modulus E' (MPa)	Rubbery Modulus (MPa)	Glass Transition Temperature (°C)	
			T_{g1}	T_{g2}
Neat DGEBA	1536	14.2		123.1
DP5	1664	16.1	123.4	202.8
DP20	1687	38.8	128.8	194.1
DP25	1660	68.0	133.8	192.0
DP0H	1673	20.1		123.3
DP5H	1709	22.4	125.6	196.5
DP20H	1831	23.5	129.7	184.7
DP25H	1915	64.8	131.6	198.2

Neat PEI's T_g : 217 °C.

Further, to investigate the response of polyblends for heating, the DSC measurements was also conducted. Figure 3.11 represents the DSC thermograms of DGEBA/PEI and DGEBA/PEI/HRGO polyblends which confirms the HRGO accelerating the curing reaction process.

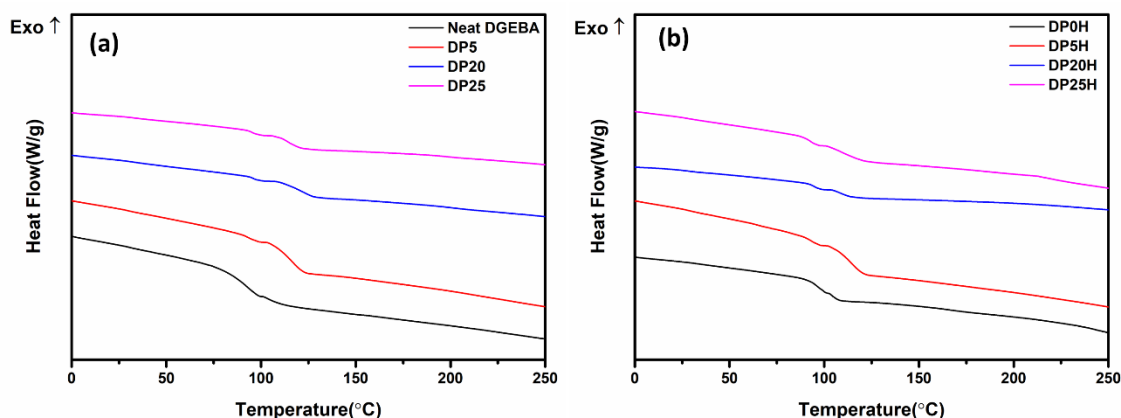


Figure 3.11. The differential scanning calorimeter (DSC) curves of (a) DGEBA/PEI polyblends and (b) DGEBA/PEI/HRGO polyblends.

3.4. Conclusions

In summary, we developed a three-dimensional double-percolation network of a DGEBA/PEI/HRGO ternary system using a low content of 0.5 wt.% HRGO with the assistance of CRIPS. The results confirmed our prediction that a unique ternary nanocomposite can be fabricated by controlling the location of the conductive filler HRGO at the interface. Furthermore, the electrical conductivity of polyblends increased by almost 16 orders of magnitude at a low content of 0.5 wt.% HRGO. The dynamic mechanical analyses demonstrated that the storage modulus was continuously enhanced by increasing PEI content and was enhanced by 15.4% with addition of 0.5 wt.% HRGO. The glass transition temperature (T_g) also increased with addition of PEI. Therefore, the DGEBA/PEI/HRGO nanocomposites have significant potential for various engineering applications such as electronic packaging, EMI shielding, electrostatic discharge, etc.

References

- [1] Shi X, Nguyen TA, Suo Z, Liu Y, Avci R. Effect of nanoparticles on the anticorrosion and mechanical properties of epoxy coating. *Surface and Coatings Technology*. 2009;204:237-45.
- [2] Yang X, Zhang Y, Chen Z, Yang Y, Jing H, Sun Z, et al. Preparation of epoxypropyl functionalized graphene oxide and its anticorrosion properties complexed with epoxy resin. *Korean Journal of Chemical Engineering*. 2020:1-11.
- [3] Aliakbari M, Jazani OM, Sohrabian M, Jouyandeh M, Saeb MR. Multi-nationality epoxy adhesives on trial for future nanocomposite developments. *Progress in Organic Coatings*. 2019;133:376-86.

- [4] Williams JC, Starke Jr EA. Progress in structural materials for aerospace systems. *Acta Materialia*. 2003;51:5775-99.
- [5] Johnson RW, Evans JL, Jacobsen P, Thompson JRR, Christopher M. The Changing Automotive Environment: High-Temperature Electronics. *IEEE transactions on electronics packaging manufacturing*. 2004;27:164-76.
- [6] Liang J, Wang Y, Huang Y, Ma Y, Liu Z, Cai J, et al. Electromagnetic interference shielding of graphene/epoxy composites. *Carbon*. 2009;47:922-5.
- [7] Jin F-L, Li X, Park S-J. Synthesis and application of epoxy resins: A review. *Journal of Industrial and Engineering Chemistry*. 2015;29:1-11.
- [8] Wetzell B, Rosso P, Hauptert F, Friedrich K. Epoxy nanocomposites – fracture and toughening mechanisms. *Engineering fracture mechanics*. 2006;73:2375-98.
- [9] Pearson RA, Yee AF. Toughening mechanisms in thermoplastic-modified epoxies: 1. Modification using poly (phenylene oxide). *Polymer*. 1993;34:3658-70.
- [10] Kunz S, Sayre J, Assink R. Morphology and toughness characterization of epoxy resins modified with amine and carboxyl terminated rubbers. *Polymer*. 1982;23:1897-906.
- [11] Chruściel JJ, Leśniak E. Modification of epoxy resins with functional silanes, polysiloxanes, silsesquioxanes, silica and silicates. *Progress in Polymer Science*. 2015;41:67-121.
- [12] Guan L-Z, Gong L-X, Tang L-C, Wu L-B, Jiang J-X, Lai G-Q. Mechanical properties and fracture behaviors of epoxy composites with phase-separation formed liquid rubber and preformed powdered rubber nanoparticles: A comparative study. *Polymer Composites*. 2015;36:785-99.
- [13] Sharma S, Singh BP, Chauhan SS, Jyoti J, Arya AK, Dhakate SR, et al. Enhanced thermomechanical and electrical properties of multiwalled carbon nanotube paper reinforced epoxy laminar composites. *Composites Part A: Applied Science and Manufacturing*. 2018;104:129-38.
- [14] Pathak AK, Kumar V, Sharma S, Yokozeki T, Dhakate SR. Improved thermomechanical and electrical properties of reduced graphene oxide reinforced polyaniline - dodecylbenzenesulfonic acid/divinylbenzene nanocomposites. *J Colloid Interface Sci*. 2019;533:548-60.

- [15] Aïssa B, Sinopoli A, Ali A, Zakaria Y, Zekri A, Helal M, et al. Nanoelectromagnetic of a highly conductive 2D transition metal carbide (MXene)/Graphene nanoplatelets composite in the EHF M-band frequency. *Carbon*. 2021;173:528-39.
- [16] Gaddam SK, Pothu R, Boddula R. Graphitic carbon nitride (g - C₃N₄) reinforced polymer nanocomposite systems—A review. *Polymer Composites*. 2020;41:430-42.
- [17] Gioti S, Stavropoulos SG, Sanida A, Psarras GC. A comparative study on the thermomechanical and electrical properties of carbide/or graphite/epoxy-reinforced composites. *Journal of Thermal Analysis and Calorimetry*. 2020;142:1649-57.
- [18] Sharma S, Rawal J, Dhakate SR, Singh BP. Synergistic bridging effects of graphene oxide and carbon nanotube on mechanical properties of aramid fiber reinforced polycarbonate composite tape. *Composites Science and Technology*. 2020;199:108370.
- [19] Yao S-S, Ma C-L, Jin F-L, Park S-J. Fracture toughness enhancement of epoxy resin reinforced with graphene nanoplatelets and carbon nanotubes. *Korean Journal of Chemical Engineering*. 2020;37:2075-83.
- [20] Li C, Thostenson ET, Chou T-W. Dominant role of tunneling resistance in the electrical conductivity of carbon nanotube-based composites. *Applied Physics Letters*. 2007;91.
- [21] Wang Y, Wu J, Wei F. A treatment method to give separated multi-walled carbon nanotubes with high purity, high crystallization and a large aspect ratio. *Carbon*. 2003;41:2939-48.
- [22] Jiang Y, Liu Y, Min P, Sui G. BN@PPS core-shell structure particles and their 3D segregated architecture composites with high thermal conductivities. *Composites Science and Technology*. 2017;144:63-9.
- [23] Cui C-h, Yan D-x, Pang H, Jia L-c, Bao Y, Jiang X, et al. Towards efficient electromagnetic interference shielding performance for polyethylene composites by structuring segregated carbon black/graphite networks. *Chinese Journal of Polymer Science*. 2016;34:1490-9.
- [24] Wu K, Lei C, Huang R, Yang W, Chai S, Geng C, et al. Design and Preparation of a Unique Segregated Double Network with Excellent Thermal Conductive Property. *ACS Appl Mater Interfaces*. 2017;9:7637-47.
- [25] Sharma S, Kumar V, Pathak AK, Yokozeki T, Yadav SK, Singh VN, et al. Design of MWCNT

bucky paper reinforced PANI–DBSA–DVB composites with superior electrical and mechanical properties. *Journal of Materials Chemistry C*. 2018;6:12396-406.

[26] Zhang F, Feng Y, Qin M, Gao L, Li Z, Zhao F, et al. Stress Controllability in Thermal and Electrical Conductivity of 3D Elastic Graphene - Crosslinked Carbon Nanotube Sponge/Polyimide Nanocomposite. *Advanced Functional Materials*. 2019;29:1901383.

[27] Zhong J, Zhou G-X, He P-G, Yang Z-H, Jia D-C. 3D printing strong and conductive geopolymer nanocomposite structures modified by graphene oxide. *Carbon*. 2017;117:421-6.

[28] Huang J, Mao C, Zhu Y, Jiang W, Yang X. Control of carbon nanotubes at the interface of a co-continuous immiscible polymer blend to fabricate conductive composites with ultralow percolation thresholds. *Carbon*. 2014;73:267-74.

[29] Mao C, Zhu Y, Jiang W. Design of electrical conductive composites: tuning the morphology to improve the electrical properties of graphene filled immiscible polymer blends. *ACS Appl Mater Interfaces*. 2012;4:5281-6.

[30] Chen J, Cui X, Zhu Y, Jiang W, Sui K. Design of superior conductive polymer composite with precisely controlling carbon nanotubes at the interface of a co-continuous polymer blend via a balance of π - π interactions and dipole-dipole interactions. *Carbon*. 2017;114:441-8.

[31] Sumita a, Sakata K, Hayakawa Y, Asai S, Miyasaka K, Tanemura M. Double percolation effect on the electrical conductivity of conductive particles filled polymer blends. *Colloid and Polymer Science*. 1992;270:134-9.

[32] Monti M, Rallini M, Puglia D, Peponi L, Torre L, Kenny JM. Morphology and electrical properties of graphene–epoxy nanocomposites obtained by different solvent assisted processing methods. *Composites Part A: Applied Science and Manufacturing*. 2013;46:166-72.

[33] Nasti G, Gentile G, Cerruti P, Carfagna C, Ambrogi V. Double percolation of multiwalled carbon nanotubes in polystyrene/polylactic acid blends. *Polymer*. 2016;99:193-203.

[34] Thongruang W, Spontak RJ, Balik CM. Bridged double percolation in conductive polymer composites: an electrical conductivity, morphology and mechanical property study. *Polymer*. 2002;43:3717-25.

[35] Rabek JF. Experimental methods in polymer chemistry. *Journal of Polymer Science: Polymer*

Letters Edition. 1980:34-5.

[36] Zhang H, Heng Z, Zhou J, Shi Y, Chen Y, Zou H, et al. In-situ co-continuous conductive network induced by carbon nanotubes in epoxy composites with enhanced electromagnetic interference shielding performance. *Chemical Engineering Journal*. 2020;398:125559.

[37] Salzano de Luna M, Filippone G. Effects of nanoparticles on the morphology of immiscible polymer blends – Challenges and opportunities. *European Polymer Journal*. 2016;79:198-218.

[38] Macosko CW. Morphology development and control in immiscible polymer blends. *Macromolecular Symposia* 2000. p. 171-84.

[39] Chen J, Du X-C, Zhang W-B, Yang J-H, Zhang N, Huang T, et al. Synergistic effect of carbon nanotubes and carbon black on electrical conductivity of PA6/ABS blend. *Composites Science and Technology*. 2013;81:1-8.

[40] Chen J, Shi Y-y, Yang J-h, Zhang N, Huang T, Chen C, et al. A simple strategy to achieve very low percolation threshold via the selective distribution of carbon nanotubes at the interface of polymer blends. *Journal of Materials Chemistry*. 2012;22:22398-404.

[41] Deng H, Lin L, Ji M, Zhang S, Yang M, Fu Q. Progress on the morphological control of conductive network in conductive polymer composites and the use as electroactive multifunctional materials. *Progress in Polymer Science*. 2014;39:627-55.

[42] Li W, Xia Z, Li A, Ling Y, Wang B, Gan W. Effect of SiO₂ nanoparticles on the reaction-induced phase separation in dynamically asymmetric epoxy/PEI blends. *RSC Advances*. 2015;5:8471-8.

[43] Xia Z, Li W, Ding J, Li A, Gan W. Effect of PS-b-PCL block copolymer on reaction-induced phase separation in epoxy/PEI blend. *Journal of Polymer Science Part B: Polymer Physics*. 2014;52:1395-402.

[44] Araki T, Tanaka H. Three-dimensional numerical simulations of viscoelastic phase separation: Morphological characteristics. *Macromolecules*. 2001;34:1953-63.

[45] Dang TT, Pham VH, Hur SH, Kim EJ, Kong BS, Chung JS. Superior dispersion of highly reduced graphene oxide in N,N-dimethylformamide. *J Colloid Interface Sci*. 2012;376:91-6.

[46] Wan H-M, Ma C-G, Xi D-Y, Pan Y-L, Shi Q, Tao P-Y. Effect of Carbon-based Nanofillers

on Electrical Properties of Epoxy/Polyetherimide Composites. *ADVANCED MATERIAL SCIENCE AND ENGINEERING AMSE2016*: World Scientific; 2016. p. 19-24.

[47] Ma CG, Xi DY, Liu M. Epoxy resin/polyetherimide/carbon black conductive polymer composites with a double percolation structure by reaction-induced phase separation. *Journal of Composite Materials*. 2013;47:1153-60.

[48] Wang X, Li W, Zhang Z, Chen K, Gan W. Selective localization of multi-walled carbon nanotubes in epoxy/polyetherimide system and properties of the conductive composites. *Journal of Applied Polymer Science*. 2019;136:47911.

[49] Liu Y, Yang X, Yue L, Li W, Gan W, Chen K. Selective dispersion of silver nanowires in epoxy/polyetherimide binary composites with enhanced electrical conductivity: a study of curing kinetics and morphology. *Polymer Composites*. 2019;40:4390-401.

[50] Guo L, Xiao C, Wang H, Chen L, Zhang X, Zheng K, et al. Thermally conductive polystyrene/epoxy nanocomposites fabricated by selective localization of hybrid fillers. *Colloid and Polymer Science*. 2016;294:901-10.

[51] White KL, Sue HJ. Electrical conductivity and fracture behavior of epoxy/polyamide - 12/multiwalled carbon nanotube composites. *Polymer Engineering & Science*. 2011;51:2245-53.

[52] Van Oss C, Good R, Chaudhury M. The role of van der Waals forces and hydrogen bonds in "hydrophobic interactions" between biopolymers and low energy surfaces. *Journal of colloid and Interface Science*. 1986;111:378-90.

[53] Li Z, Giese R, Van Oss C, Yvon J, Cases J. The surface thermodynamic properties of talc treated with octadecylamine. *Journal of colloid and Interface Science*. 1993;156:279-84.

[54] Sumita M, Sakata K, Asai S, Miyasaka K, Nakagawa H. Dispersion of fillers and the electrical conductivity of polymer blends filled with carbon black. *Polymer bulletin*. 1991;25:265-71.

[55] Wu S. Surface tension and polarity of solid polymers. *Polymer interface and adhesion*: Routledge; 2017. p. 169-214.

[56] Mimura K, Ito H, Fujioka H. Improvement of thermal and mechanical properties by control of morphologies in PES-modified epoxy resins. *Polymer*. 2000;41:4451-9.

- [57] Yamanaka K, Inoue T. Structure development in epoxy resin modified with poly (ether sulphone). *Polymer*. 1989;30:662-7.
- [58] Krause B, Pötschke P, Häußler L. Influence of small scale melt mixing conditions on electrical resistivity of carbon nanotube-polyamide composites. *Composites Science and Technology*. 2009;69:1505-15.
- [59] Jin X, Li W, Liu Y, Gan W. Self-constructing thermal conductive filler network via reaction-induced phase separation in BNNSs/epoxy/polyetherimide composites. *Composites Part A: Applied Science and Manufacturing*. 2020;130:105727.

CHAPTER 4 Enhanced EMI shielding and electrical conductivity properties in DGEBA/PEI/RGO ternary system

4.1.Introduction

Multifunctional polymer nanocomposites are progressively replacing metallic parts because of their superior properties, such as low density, excellent mechanical properties, low cost, and chemical stability, etc. However, commercial polymers are electrically insulating in nature and usually require highly conducting fillers to come in the category of conducting nanocomposites. The introduction of electrically conducting nanofiller at high concentration was one of the most efficient approaches for developing conducting polymer composites (CPCs). Therefore, many efforts have aimed to develop this strategy to achieve desired electrical conductivity. These include the introduction of electrically conducting fillers such as carbon nanotubes (CNT) [1], carbon dots [2], graphene [3], and their derivatives for CPCs [4].

With the rapid development of communications and internet technologies, electromagnetic interference (EMI) has emerged as a serious threat to the stable functioning of electronic devices [5-8]. The application of CPCs with nanofillers is one of the solutions. The addition of electrically conducting nanofillers increases the shielding properties of material via various mechanisms, such as conductive losses, destructive interference, hysteresis losses, and heating losses, etc. Zhang et al. prepared laminar structures of polyethylene oxide(PEO)/ CNT (as shielding layer) and cellulose (as a supporting substrate) with high loading of nanofiller CNT at 40 wt.%, which yielded shielding effectiveness of 30-40 dB in the X band [9]. Zeng et al. successfully prepared a reinforced waterborne polyurethane (WPU) film with 61.5 wt.% of multi-walled carbon nanotubes (MWCNT) and its shielding effectiveness reached 35 dB [10]. Liang et al. fabricated epoxy/graphene nanocomposites with ~15 wt.% filler loading and obtained shielding effectiveness of 21 dB [11]. Wang et al. reported the 35 dB shielding effectiveness with the incorporation of hierarchical MWCNT-Fe₃O₄/Ag nanofiller (15 wt. %) [12]. It is obvious from these studies that CPCs with higher loadings of nanofillers from 15 to 61.5 wt.% have obtained greater shielding properties. However, achieving homogeneous nanofillers dispersion in a polymer matrix with hydrodynamics and viscoelastic properties to contend with is difficult. In

addition, the mechanical properties of a polymer matrix may deteriorate with high filler loading. Therefore, it is very challenging to obtain effective EMI shielding properties in polymer nanocomposites by loading low content of nanofillers.

Recently, the combination of multiphase polyblend has been adopted to develop electrically conducting nanocomposites with low filler content, overcoming the problems of poor processability and deteriorating mechanical properties. In these polyblends, different phase structures with different filler localization can be possible, which is used to construct electrically conductive networks with low nanofiller loading. To form conductive networks with low percolation, it is necessary that the nanofiller be localized at the interface of the separated polymer phases in co-continuous or phase inversion polyblend with the balanced mechanical properties of two integrated polymers [13]. When the polyblend system contains a thermosetting polymer like diglycidyl ether of bisphenol A (DGEBA), the curing reaction can control the localization of the nanofiller at the interface of two immiscible polymers [14]. Other than the thermodynamics of curing reaction, various kinetic and rheological factors also influence the final phase structure of the polyblend and preferential localization of fillers.

In the past few years, there have been various reports on selective localization of nanofiller in the co-continuous polyblend of epoxy and other amphiphilic block co-polymer [15, 16] that is simply controlled by curing reaction induced phase separation (CRIPS) [17-20]. However, fewer reported regarding using phase-separated structures to synthesize materials with low loadings of selectively localized conductive fillers to achieve favorable EMI shielding properties [21, 22]. The preparation of rigid nanofiller foam which can withstand the hydrodynamic forces of resin infusion is not an easy task and further practical applicability for complex geometries is very difficult. Hence, a simple processing technology to develop thermosetting resin-based effective EMI shielding materials with low loading of conducting filler is extremely important.

In this chapter, DGEBA/ polyetherimide (PEI) polyblend system was prepared. The CRIPS technique facilitated reduced graphene oxide (RGO) selectively localized at the interface of two immiscible phases. The resultant double-percolated conductive networks of RGO in co-continuous or inversion phase structure of DGEBA/PEI polyblends helped to improve the

electrical conductivity of nanocomposites at a very low concentration of RGO. Furthermore, the effects of blending and selective localization of RGO on the thermomechanical and EMI shielding properties of nanocomposites are investigated. This study provides an interesting technique for developing low nanofiller loading polyblend nanocomposites with balanced electrical, thermomechanical, and EMI shielding properties. These multifunctional properties contribute novel three-dimensional DGEBA/PEI/RGO nanocomposites for effective aerospace structural materials and microelectronics applications.

4.2. Experimental section

4.2.1. Synthesis of RGO

The preparation of RGO was according to a previous publication [14]. The RGO suspension was then filtered and washed by DMF for three times to remove the unreacted reducing agent (i.e., hydrazine). Finally, the RGO flakes were dried in the vacuum oven at 150 °C for 24 h to evaporate the residual solvent completely. These free-standing RGO papers were thus obtained for morphological and X-ray photoelectron spectroscopy (XPS) analysis.

4.2.2. Fabrication of DGEBA/RGO/PEI nanocomposites

The nanocomposites with RGO were prepared using the solvent casting technique. Initially, PEI was dissolved in CH₂Cl₂ with magnetic stirring. A homogeneous suspension of RGO (0.4 mg/mL) was then added into PEI solution and stirred at room temperature. Subsequently, DGEBA oligomer was added into the PEI/RGO mixture. The mixture was stirred at 90 °C for 2 h to remove most of the solvent and degassed in the vacuum oven at 120 °C for 12 h to completely remove the residual solvent. Finally, a crosslinking solution of DMBA and Me-THPA was added to the degassed polyblend (DGEBA: crosslinking solution= 1:0.8) and stirred at 110 °C. After pouring into the moulds, the polyblend was then pre-cured at 150 °C for 5 h and post-cured at 200 °C for 2 h. The compositions of DGEBA, RGO, and PEI were given in Table 4.1. The DGEBA/PEI/RGO nanocomposites were designated as DP_{n₁}/R_{n₂} where D, P, *n₁*, R, and *n₂* represent DGEBA, PEI, the weight percentage of PEI in DGEBA, the RGO, and the weight percentage of RGO in the DGEBA/PEI/RGO nanocomposites, respectively. For comparison, samples including neat DGEBA, nanocomposites DR1, DR1.5, DR2, DR2.5, DR3, DP25, and DP30 were prepared using

a similar casting technique. A schematic of the fabrication process is shown in Figure 4.1.

Table 4.1. Formulation of samples.

Samples	DGEBA	PEI (phr) ¹	RGO (wt.%)	C-A solution
DGEBA	100	0	0	80
DR1	100	0	$x / (100+0+x) = 1.0\%$	80
DR1.5	100	0	$x / (100+0+x) = 1.5\%$	80
DR2	100	0	$x / (100+0+x) = 2.0\%$	80
DR2.5	100	0	$x / (100+0+x) = 2.5\%$	80
DR3	100	0	$x / (100+0+x) = 3.0\%$	80
DP25	100	25	0	80
DP30	100	30	0	80
DP5R3	100	5	$x / (100+5+x) = 3.0\%$	80
DP25R1	100	25	$x / (100+25+x) = 1.0\%$	80
DP25R1.5	100	25	$x / (100+25+x) = 1.5\%$	80
DP25R2	100	25	$x / (100+25+x) = 2.0\%$	80
DP25R2.5	100	25	$x / (100+25+x) = 2.5\%$	80
DP25R3	100	25	$x / (100+25+x) = 3.0\%$	80
DP30R1	100	30	$x / (100+30+x) = 1.0\%$	80
DP30R1.5	100	30	$x / (100+30+x) = 1.5\%$	80
DP30R2	100	30	$x / (100+30+x) = 2.0\%$	80
DP30R2.5	100	30	$x / (100+30+x) = 2.5\%$	80
DP30R3	100	30	$x / (100 + 30+x) = 3.0\%$	80

¹phr: parts per hundred in the DGEBA, x: RGO (phr), C-A solution: a solution of Me-THPA and DMBA.

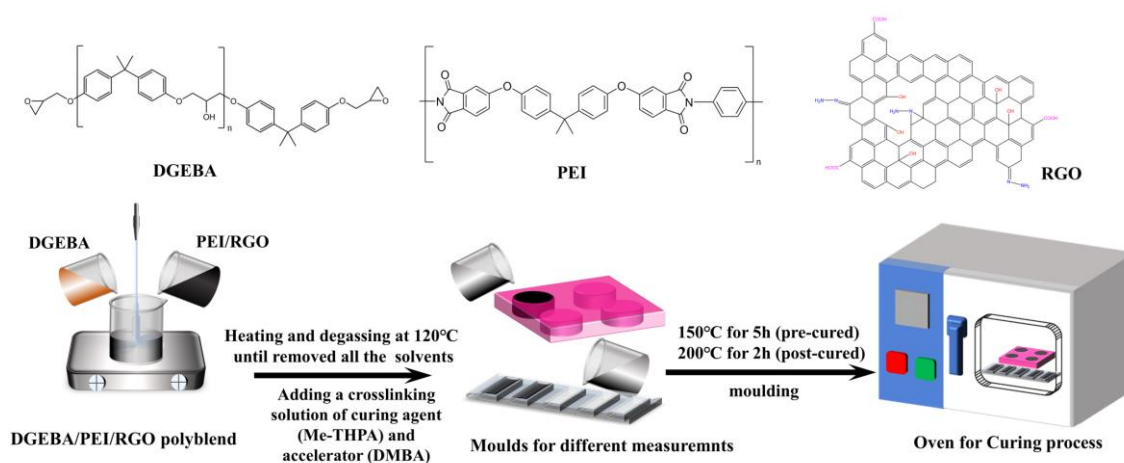


Figure 4.1. Schematic of the fabrication of DGEBA/PEI/RGO nanocomposites.

4.2.3. Measurement and characterization

Transmission electron microscope (TEM, H-8100, Hitachi High-Tech Co., USA) and scanning electron microscope (SEM, S-3400N, Hitachi High-Tech Co., USA) analyses were to

observe the morphology of the fillers. FETEM measurements were performed by using a FETEM (Tecnai G² F20 X-Twin, FEI Co., USA) operated at an accelerating voltage of 200 kV. Ultrathin films (thickness: 100-200 nm) of the nanocomposite samples were prepared using an ultramicrotome (RMC CR-X, Boeckeler Instruments Co., USA) equipped with a glass knife for FETEM observation. Raman spectra were performed by a Raman spectrometer (DXR™ 3, Thermo Fisher Scientific Inc., USA). XPS analysis was performed on an ESCALAB 250XI (Thermo Fisher Scientific Inc., USA) system using a monochromatic Al-K α X-ray source (K α 1486.6 keV) and a CLAM-2 hemispherical analyzer for electron detection. Fourier transform infrared (FT-IR) spectra were recorded using an FT-IR (Nicolet™ iS™ 5, Thermo Fisher Scientific Inc., USA) and attenuated total reflectance (ATR) accessory in the range of 4000-400 cm⁻¹ at room temperature. The specimens were prepared in disk-shaped silicone moulds with 40 mm in diameter and 2 mm in thickness of the specimens and measured by using the four-point probe equipment (CMT-100MP, AIT Co., Korea) for electrical properties measurement. The thermomechanical properties of the specimens were attained by DMA (Q800, TA Instruments Co., USA) in the single cantilever mode at a frequency of 1 Hz. The temperature ranges applied were from 30 to 180 °C for neat DGEBA and from 30 to 230 °C for other nanocomposites at a heating rate of 3 °C/min. The samples were cast in 45 mm × 10 mm × 3 mm rectangular aluminum moulds for DMA analysis. The contact angle (CA) measurements were conducted by a Phoenix 300 (SEO Co., Korea) using the sessile drop method at room temperature with 15–17 μ L of deionized water (DI), glycerol (GL), and formamide (FA), respectively. Thermogravimetric analysis (TGA, Q50, TA Instruments Co., USA) was carried out under a nitrogen atmosphere at a heating rate of 10 °C/min. Differential scanning calorimeter (DSC, Q20 V24.10, TA Instruments Co., USA) measurements were performed under a constant nitrogen flow of 50 mL/min and at a heating rate of 20 °C/min. The EMI shielding effectiveness (SE) parameters of nanocomposites were measured by a vector network analyzer (E5071C Agilent Inc., USA) in the frequency range of 8.2–12.4 GHz (X-band) at room temperature. The samples in 2 mm thickness were cut into rectangle plates of 22.9 mm × 10.2 mm to fit the waveguide sample holder.

4.3. Results and discussion

4.3.1. Morphological properties of RGO

SEM micrographs of GO and RGO flakes are shown in Figure 4.2a-b and 4.2d-e, respectively. Figure 4.2a-b shows that the pristine GO is randomly aggregated in wide size distribution. Figure 4.2d-e illustrates that RGO has many wrinkles and crumples after hydrazine reduction, and they are entangled with each other. TEM micrographs of GO and RGO are shown in Figure 4.2c and 4.2f. TEM micrographs of GO and RGO represent the wrinkled structure with a few layers stacking, and Raman, FT-IR, and XPS analyses were also conducted to estimate the actual structural changes between GO and RGO before RGO was introduced into polyblends to prepare nanocomposites.

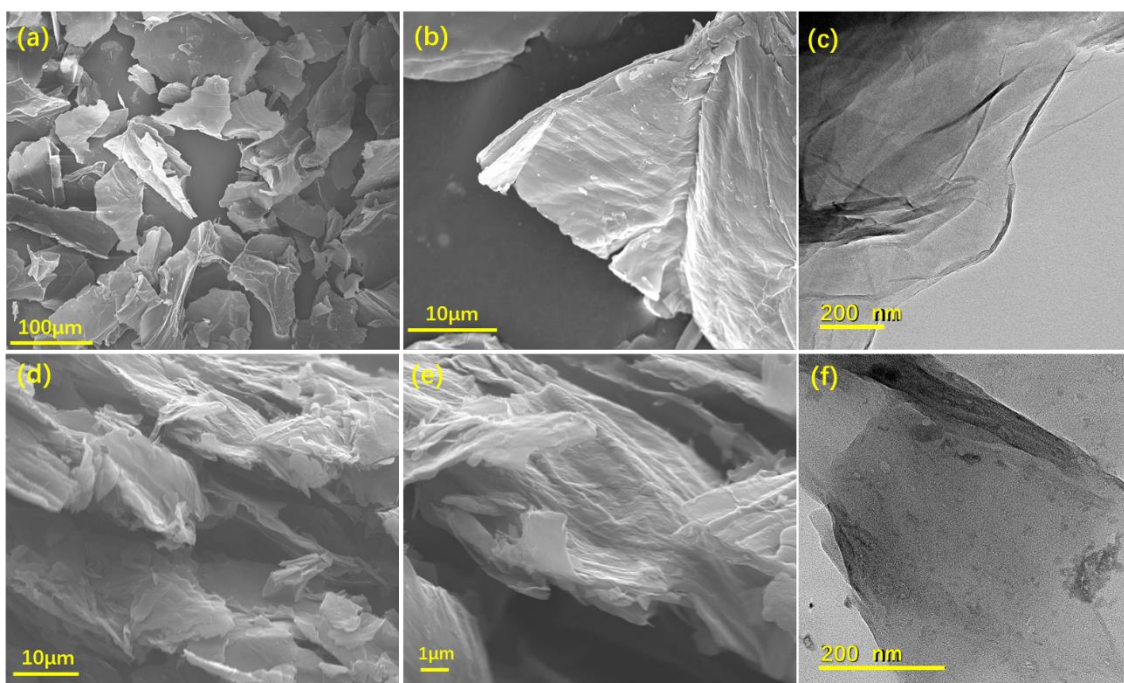


Figure 4.2. SEM micrographs of pristine GO at (a) low and (b) high magnification, (c) TEM micrograph of GO, SEM micrographs of RGO flakes at (d) low and (e) high magnification, (f) TEM micrograph of RGO.

4.3.2. Physical and chemical properties of RGO

Raman analysis provides information regarding the inelastic scattering by molecules irradiated by the monochromatic excitation source, thereby elucidating the structural properties of a material. Figure 4.3a represents the Raman spectra of pristine GO and RGO. Two fundamental vibrations can be observed between 1200 and 1600 cm^{-1} from both GO and RGO. The first D vibration band which is associated with κ -point photon breathing mode of A_{1g}

symmetry of GO and RGO appears at 1350.7 and 1345.9 cm^{-1} , respectively. The G vibration band which is associated with E_{2g} phonons of sp^2 hybridized carbon of GO and RGO are found at 1586.9 and 1578.3 cm^{-1} , respectively [23, 24]. the intensity ratio of the D band and G band (I_D/I_G) increases from 0.909 to 1.045 after hydrazine reduction of GO, due to the sp^2 carbon cluster. The higher intensity of RGO suggests the reduction of oxygenated groups and the presence of more isolated graphene domains compared to GO [25]. Due to the multilayer structure, the Lorentzian peaks of the 2D band for GO and RGO appear at 2692.9 cm^{-1} and 2675.6 cm^{-1} , respectively. Moreover, the increased intensity of the 2D band with a slight shift to lower frequencies in RGO suggests inhibited stacking due to the reduction of oxygenated functional groups.

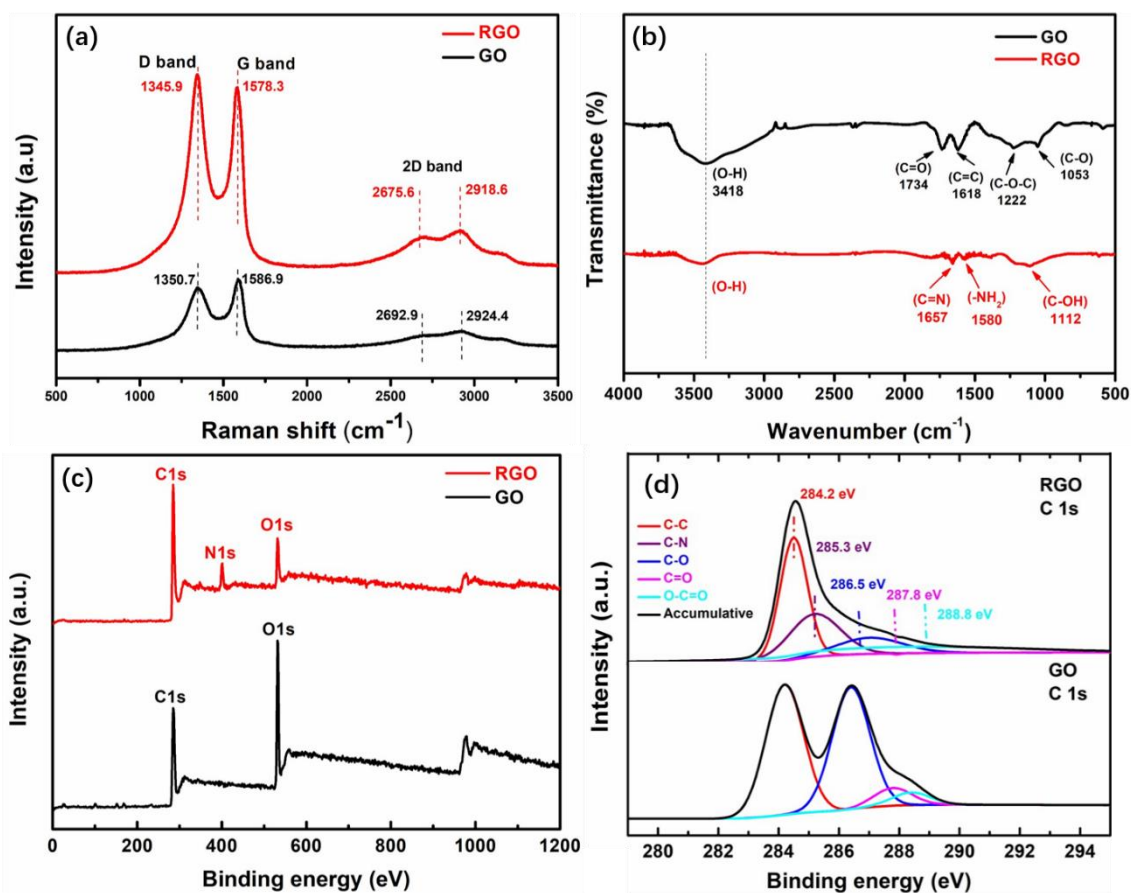


Figure 4.3. (a) Raman and (b) FT-IR spectra of RGO flakes and GO. (c) Wide-scan, and (d) C 1s high-resolution core-level of XPS spectra for GO and RGO flakes.

Figure 4.3b shows the FT-IR spectra of GO and RGO. The presence of intense peaks at 1734 cm^{-1} (from C=O stretching), 1222 cm^{-1} (from C–O–C stretching), 1053 cm^{-1} (from C–O stretching) and a broad band at ~ 3418 cm^{-1} (from hydroxyl groups) imply the presence of oxygenated functional groups in GO [26, 27]. The disappearance of oxygenous moieties along with the

resultant nitrogenous groups from hydrazine treatment clearly indicates the successful reduction of pristine GO.

XPS analysis can provide information based on X-ray induced photoemission. In the case of RGO, a new peak appears at ~ 400 eV, which corresponds to the N1s component [28] that results from the hydrazine reduction of GO (Figure 4.3c). Furthermore, after reduction, the intensity ratio of peaks C1s/O1s for GO increases abruptly from 1.2 to 10.4, which is related to the quantitative information of the reduction of GO. In Figure 4.3d, GO contains a wide range of oxygenated functional groups, such as epoxide, carbonyl, and carboxyl groups [29, 30] which are assigned at 286.5 eV, 287.8 eV, and 288.8 eV, respectively. In comparison with GO, peaks corresponding to oxygen-containing functional groups are significantly decreased in RGO after hydrazine reduction indicates that most of the oxygenated functional groups were removed [29, 31]. Additionally, a new peak appears at 285.3 eV in RGO, which is the C-N bond ascribed to the hydrazine reduction [32, 33]. A high-resolution core-level of the N1s spectrum shows the -C-NH₂ bond at 399.9 eV, as shown in Figure 4.4. Additionally, the absence of the peak at ~ 398 eV corresponding to the N-N bond shows that the residual hydrazine (NH₂-NH₂) is below the detection limit of XPS. Therefore, the XPS results are consistent with those from FT-IR analysis, indicating that the reduction of GO into RGO is successful.

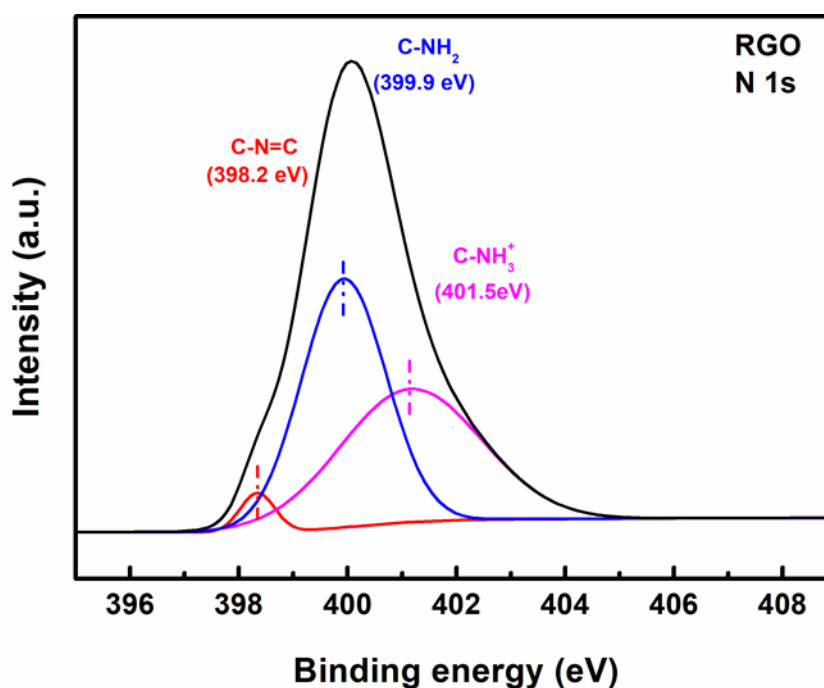


Figure 4.4. XPS spectra of RGO flakes of N 1s high-resolution core-level.

4.3.3. Morphologies and chemical properties of DGEBA/PEI/RGO nanocomposites

The morphologies of the DP_{n_1} polyblends and the localization of RGO in $DP_{n_1}R_{n_2}$ nanocomposites were observed by FETEM.

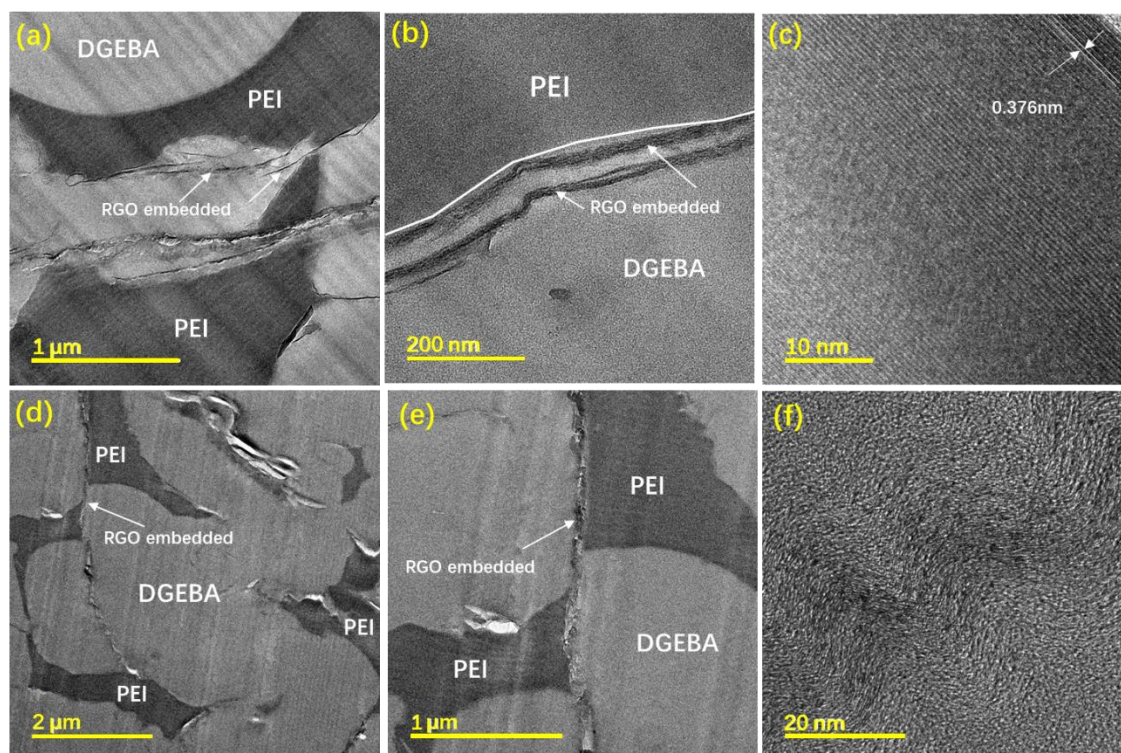


Figure 4.5. The FETEM micrographs of the DP25R3 nanocomposite at (a) lower and (b) higher magnification, (c) HRTEM micrograph of RGO in DP25R3, (d-e) DP30R3 nanocomposite with inversion morphology, and (f) HRTEM micrograph of RGO in DP30R3.

Figure 4.5a and d represent the inversion phase structure of DP25R3 and DP30R3, respectively. The phase structure of DP25R3 is changed from the co-continuous phase morphology of DP25 to the inversion phase morphology [14]. This change may be caused by the amino groups from RGO which stimulate the CRIPS [19]. Figure 4.5b shows a double-percolated structure of DP25R3 formed by RGO selective localization at the interface and close to the DGEBA domain. The presence of RGO at the interface is confirmed by the HRTEM of DP25R3 with the fringe pattern at the interface. The d-spacing value of RGO flakes is 0.376 nm in Figure 4.5c. Figure 4.5e shows that most of the crumpled surfaces of RGO flakes distribute selectively at the interface between DGEBA-rich and PEI-rich domains for nanocomposite DP30R3. Figure 4.5f exhibits the wavy fringe pattern structure of RGO that is observed at the interface of the

magnified micrograph [34, 35]. Figure 4.6 exhibits FETEM micrographs of DP30, in which white and dark domains represent the DGEBA-rich and PEI-rich phases, respectively. The PEI-rich phase forms an inversion continuous network, while DGEBA appears like a small iso-island in the PEI-rich network. The size of PEI-rich ligaments lies in the range of 50 to 400 nm. But size distribution indicates average size of ~ 55 nm which is very narrow for developing the conducting RGO network in a polyblend system.

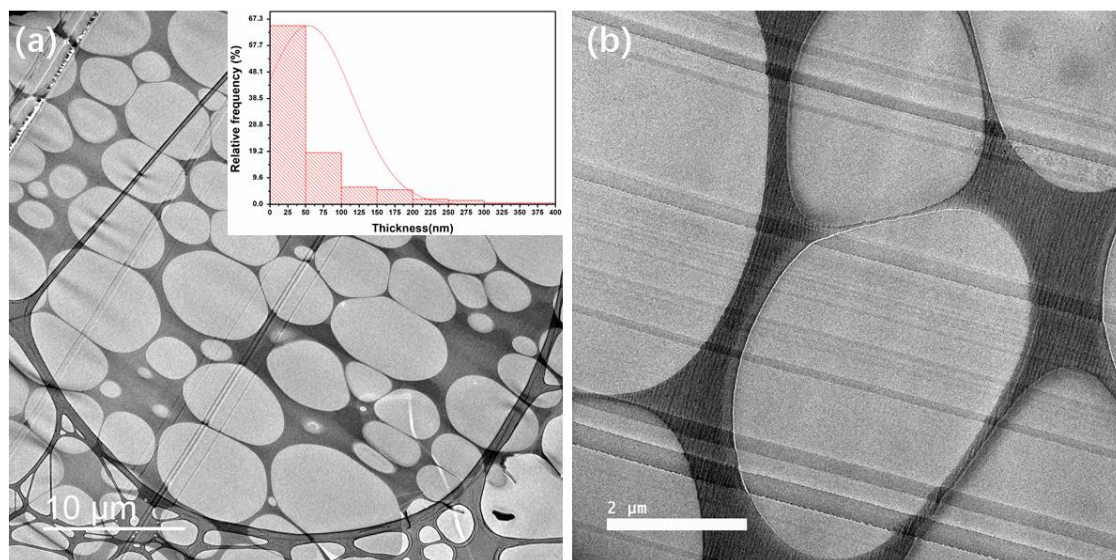


Figure 4.6. FETEM images of (a) DP30 in low magnification and the histogram of the relative frequency verse the PEI thickness to exhibit the PEI thickness distribution in the figure(inset), (b) DP30 in high magnification in which the dark domains are PEI-rich phases and bright domains are DGEBA-rich phases, respectively.

FT-IR analysis was conducted on neat DGEBA, polyblend DP30, nanocomposites DR3 and DP3OR3, respectively, and this spectral information is presented in Figure 4.7. The peaks of neat DGEBA at ~ 2964 cm^{-1} , 2873 cm^{-1} , 1608 cm^{-1} , 1510 cm^{-1} , 912 cm^{-1} , and 830 cm^{-1} correspond to the C-H stretching of CH_2 , C-H stretching of aromatic and aliphatic, C=C stretching of aromatic rings, C-C stretching of aromatic, C-O stretching of oxirane group, and O-C-O stretching of oxirane group, respectively [36, 37]. Meanwhile, the peaks at ~ 1245 cm^{-1} , 1183 cm^{-1} , and 1036 cm^{-1} belong to different aliphatic and aromatic C-H vibrations [38].

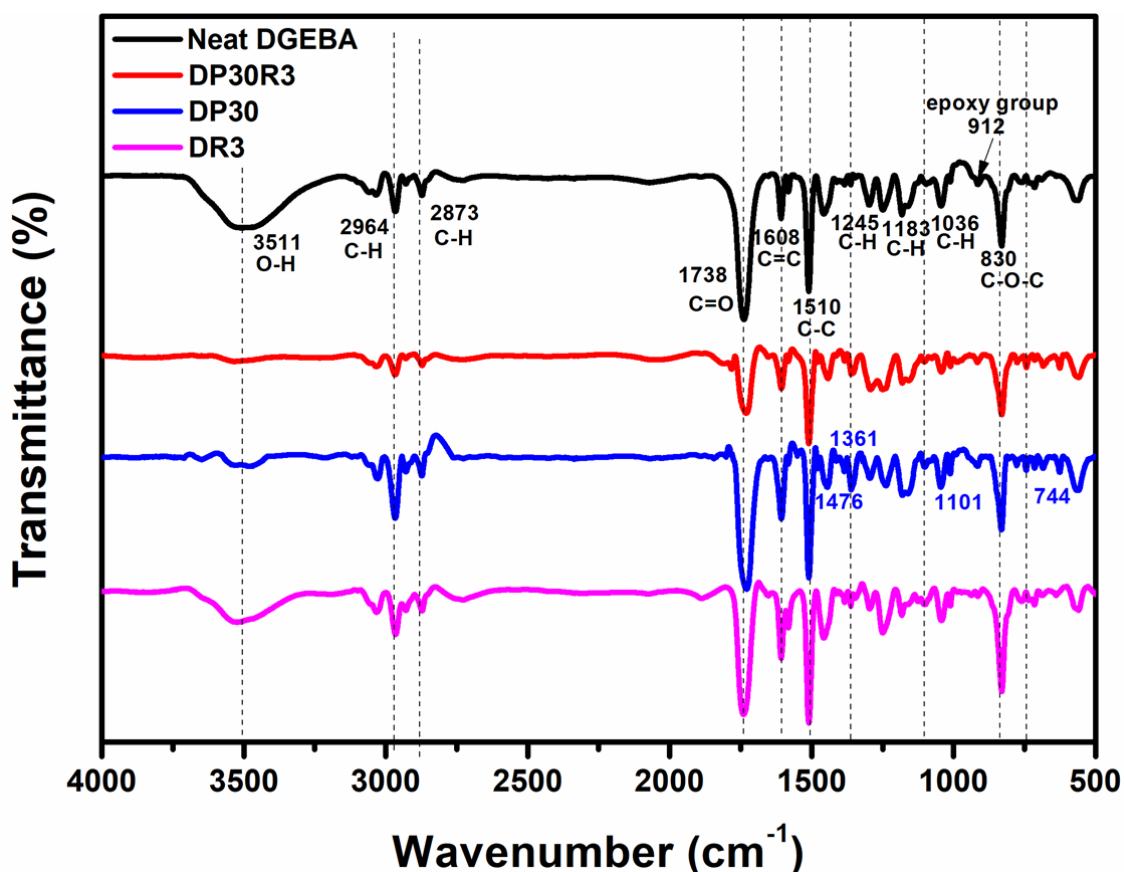


Figure 4.7. The FT-IR spectra of DR3, DP30, DP30R3, and neat DGEBA.

The peaks of DP30 at $\sim 1476\text{ cm}^{-1}$, 1361 cm^{-1} , 1101 cm^{-1} , and 744 cm^{-1} correspond to aromatic ring stretching, C–N stretching (in phthalimide rings), Ar–O–Ar stretching, and C–N bending (in phthalimide rings) vibrations, respectively [39, 40], which are not visible in neat DGEBA or DR3. In comparison with DP30, however, DP30R3 does not show a significant decrement in the peak intensities at $\sim 1658\text{ cm}^{-1}$ and 1573 cm^{-1} , which are associated with C=N and -NH₂ stretching, respectively, and are formed by hydrazine reduction of RGO [14], due to the low content of RGO in the polyblend. The PEI chains might more efficiently interact with RGO through non-bonding interactions such as electrostatic, dipole, and π - π stacking interactions between PEI and RGO basal plane [41].

4.3.4. Prediction for selective localization of RGO

Several studies used different complex parameters to solve the selective localization of a kind of nanofiller in an immiscible polyblend. Even if the analysis of localization involves many factors, such as the thermodynamics, kinetics, fluid dynamics, viscosity ratio, and phase separation [42-44]. Considering the wettability parameter is still an efficient approach to estimate

it.

To assess the surface tension of components, CA measurements with the Geometrical mean (GM) method [45] was conducted and then calculated the surface tension using the Owens-Wendt equation combined with the Young equation [46] as follows:

$$\gamma_L(1 + \cos \theta) = 2\sqrt{\gamma_S^d \gamma_L^d} + 2\sqrt{\gamma_S^p \gamma_L^p} \quad (4.1)$$

where γ_S and γ_L are the surface tensions of the solid and liquid compound, respectively, and d and p are the dispersive and polar portions of surface tension, respectively.

Figures of the contact angles are shown in Figure 4.8. The interfacial tension (γ_{A-B}) can be calculated by the Harmonic mean (HM) equation (2) [45] and the GM equation (3) [46] as follows:

$$\gamma_{A-B} = \gamma_A + \gamma_B - 2\left(\sqrt{\gamma_A^d \gamma_B^d} + \sqrt{\gamma_A^p \gamma_B^p}\right) \quad (4.2)$$

$$\gamma_{A-B} = \gamma_A + \gamma_B - 4\left(\gamma_A^d \gamma_B^d / (\gamma_A^d + \gamma_B^d) + \gamma_A^p \gamma_B^p / (\gamma_A^p + \gamma_B^p)\right) \quad (4.3)$$

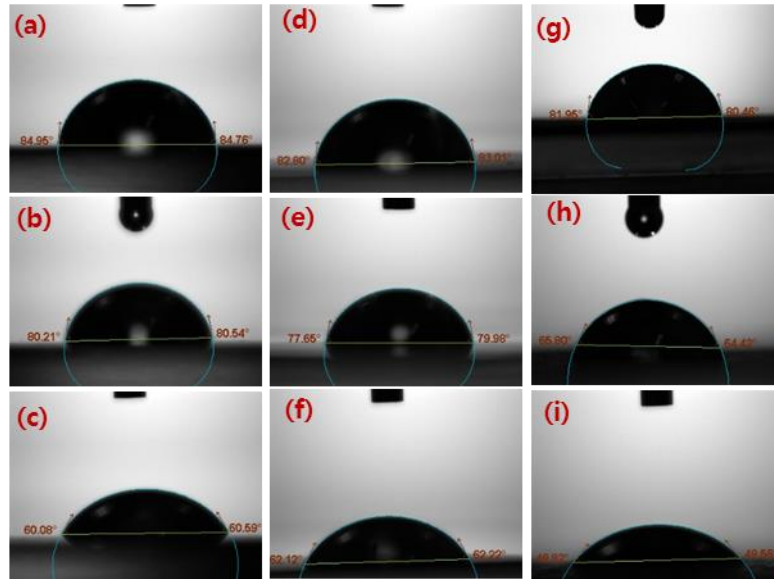


Figure 4.8. The contact angle images of samples: (a) DI on DGEBA, (b) DI on PEI, (c) DI on RGO, (d) GL on DGEBA, (e) GL on PEI, (f) GL on RGO, (g) FA on DGEBA, (h) FA on PEI, (i) FA on RGO.

The wetting coefficient (ω_a) first proposed by Sumita et al. [47] is generally applied for predicting fillers localization [48-50]. The ω_a can be calculated by Young's equation:

$$\omega_a = \gamma_{R-P} - \gamma_{R-D} / (\gamma_{D-P}) \quad (4.4)$$

where γ_{R-P} , γ_{R-D} , and γ_{D-P} are the interfacial tensions between the RGO and PEI phase,

between the RGO and DGEBA phase, and between the DGEBA and PEI phase, respectively. The prediction is based on the value of ω_a . RGO will localize in the PEI phase preferentially if $\omega_a < -1$, or at the interface between DGEBA and PEI if $-1 < \omega_a < 1$, or even in the DGEBA phase if $\omega_a > 1$.

Table 4.2. The γ_{pair} and ω_a were obtained by different methods.

Nanocomposites	Component pair	$\gamma_{\text{pair}}(\text{mN/m})$	$\gamma_{\text{pair}}(\text{mN/m})$	ω_a	Predicted localization of RGO
		Harmonic	Geometric		
DGEBA/PEI/RGO	DGEBA/PEI	3.14	1.63	$-1 < 0.998 < 1$	Interface (HM)
	DGEBA/RGO	4.42	2.37	$1.060 > 1$	DGEBA phase (GM)
	PEI/RGO	1.28	0.65		

The interfacial tension and wetting coefficients for nanocomposites DGEBA/PEI/RGO were calculated using the HM and GM methods (Table 4.2). The wetting coefficients are found to be $-1 < \omega_a = 0.998 < 1$ using the HM method and $\omega_a = 1.060 > 1$ using the GM method, which indicates that the RGO may localize selectively at the interface and have an affinity toward the DGEBA phase in DGEBA/PEI/RGO systems. The values of ω_a from both the harmonic and geometric methods are close to 1, indicating the two possibilities of selective localization for RGO according to different RGO content. In our previous work with 0.5 wt.% RGO in nanocomposites [14], the prediction using the harmonic method showed that RGO selectively localized at the interface. However, increasing the content of RGO to 3 wt.% in this work, a few RGO enter the DGEBA phase close to the interface, as predicted by the geometric method, due to the limitation of interface and the strong interfacial tension of DGEBA. This prediction is consistent with the FETEM micrographs presented in Figure 4.5.

4.3.5. Electrical properties of nanocomposites

Figure 4.9a and b show the electrical properties of nanocomposites DRn_2 and DPn_1Rn_2 , respectively. Compared to DRn_2 , the DPn_1Rn_2 have higher electrical conductivity per RGO content, as shown in Figure 4.9b. The electrical conductivity of nanocomposite DP30R3 reaches 366.3 S/m, which is almost 26 times that of nanocomposite DR3 (14.1 S/m). It has been reported that the selective localization of nanofiller would play a crucial role in the electrical properties of nanocomposites [51, 52]. When a conductive nanofiller is selectively localized at the interface of an immiscible two polymers system, it facilitates the formation of a conductive pathway in the polyblend at minimal nanofiller content. From the electrical conductivity difference between

DP30R3 and DR3, it is evident that the PEI in nanocomposite DP30R3 facilitates the selective localization of RGO at the interface and the formation of conductive networks. FETEM observations (Figure 4.5) show the morphology of DP30R3 polyblends with an inversion phase structure that is different from the morphologies of nanocomposites without PEI. The simultaneous curing reaction of DGEBA and phase separation between DPn_1 according to the spinodal decomposition mechanism allows the formation of a double-percolation RGO network structure. It is this double-percolation RGO network localizing at the interface between DGEBA and PEI that may cause significantly improved electrical conductivity.

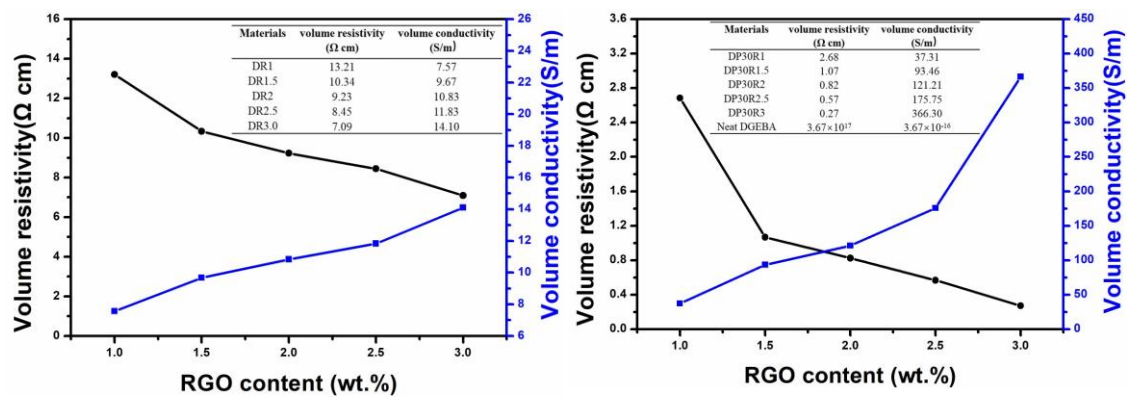


Figure 4.9. The volume resistivity and volume conductivity of (a) DRn_2 and (b) $DP30Rn_2$ nanocomposites with varying RGO content.

From the electrical conductivity measurement of nanocomposites with different RGO contents, it has been seen that a high content of RGO is required to form the conductive networks. Moreover, in comparison with DR3, DP30R1 possesses a higher volume conductivity despite its lower RGO content (1 wt.%). This difference is likely caused by the incorporation of PEI in DGEBA, leading to a double percolation conductive RGO network formed at their interface. In other words, only a small amount of RGO is needed to form conductive pathways at the continuous interface and enough to achieve the insulator/conductor transition. Further, among the DPn_1/Rn_2 nanocomposites, DP30R3 exhibits the highest electrical conductivity (366.3 S/m), which is higher than those of other reported polyblends networks, even though it has a lower RGO loading (Table 4.3).

Table 4.3. Comparison of electrical properties of previously published filler ternary polyblend systems with those of the systems in the current work.

Samples	Polymer	Polymer	Filler	Volume	Volume	[Ref]
---------	---------	---------	--------	--------	--------	-------

	A	B	Loading (wt. %)	Resistivity (Ω cm)	Conductivity (S/m)	
EP/PEI/GnPs	DGEBA	PEI	2	5.7×10^5	—	[53]
PUF@GF/Epoxy	DGEBA	PU foam	8.04 vol%	—	10^{-9}	[54]
MWCNT+GNP/Epoxy	DGEBA	—	2+3	3.1×10^{-3}	3.1×10^{-3}	[55]
EP/35PEI/GnPs	DGEBA	PEI	2	$\approx 10^7$	$\approx 10^{-5}$	[56]
EP/PEI/CB	DGEBA	PEI	1	$\approx 10^3$	—	[49]
DGEBA/PEI/MWCN Ts	DGEBA	PEI	2	3.86×10^6	—	[37]
DGEBA/PEI/AgNWs	DGEBA	PEI	3	9.6×10^5 Ω (surface R)	—	[57]
DGEBA/PEI/RGO	DGEBA	PEI	1	2.68	37.31	This work
			2	0.82	121.21	
			3	0.27	366.3	

GF: graphene fluoride, GnPs: graphene nanoplatelets, CB: carbon black, MWCNTs: multiwall carbon nanotubes.

4.3.6. Thermal and thermomechanical properties of nanocomposites

The chemical changes and the thermal degradation/stability of GO and RGO were investigated by TGA. Figure 4.10a represents the TGA and derivative thermogravimetric (DTG) curves of GO and RGO. RGO exhibits higher thermal stability than pristine GO over the entire temperature range of the measurement. The evaporation of water adsorbed to the very hydrophilic surface of the GO sheets causes the DTG of GO with mass loss below 100 °C. [58]. GO shows two-step degradation, the initial mass loss of GO at around 207 °C is ascribed to the decomposition of the labile oxygenous groups, such as epoxy, hydroxyl, and carbonyl [59]. The second step of the degradation (285–645 °C) is associated with the pyrolysis of residual oxygenous groups. RGO exhibits only ~12% weight loss up to 285 °C which is much lower than GO in a similar temperature range. Finally, GO at 800 °C is only 19.9 wt.% left. After chemical reduction, the residue of RGO at 800 °C is significantly increased to 69.5 wt.%, which is much higher than that of pristine GO.

Figure 4.10b represents the TGA spectra of neat DGEBA along with nanocomposites. DP25R3 and DP30R3 exhibit two-stage degradation, whereas neat DGEBA, nanocomposite DR3 and DP5R3 with low PEI content (5 wt.%) all exhibit only one-stage degradation. For nanocomposites DP25R3 and DP30R3, the first stage of weight loss of ~ 77% happens from 200 °C to 457 °C and is ascribed to the decomposition of DGEBA and the non-aromatic part of PEI [60]. The second stage of weight loss around 12% occurs from 475 °C to 675 °C due to the decomposition of the aromatic part of PEI. The TGA data of samples are also summarized in

Table 4.4.

Table 4.4. The TGA spectra of samples under N₂ atmosphere.

Sample	Temperature range (°C)	Assignment	Residues at 800 °C (wt.%)	Specific RGO loading in the composite (wt.%)
GO	<100	(~16.9 %) The loss of physisorbed water molecules	19.9	—
	145-285	(~31.5 %) The decomposition of oxygen-containing functional groups		
	285-645	(~15 %) The pyrolysis of less stable (CO, CO ₂)		
RGO	<145	(~2.2 %) The release of water molecules	69.5	—
	145-285	(~9.3 %) The decomposition of oxygen-containing functional groups		
	285-645	(~13.4 %) The pyrolysis of less stable (CO, CO ₂)		
Neat DGEBA	200-475	(~90.6 %) The decomposition of DGEBA	2.9	—
	475-675	(~6.5%) The decomposition of few DGEBA		
DR3	200-475	(~90.6 %) The decomposition of DGEBA	5.5	2.60
	475-675	(~3.9%) The decomposition of few DGEBA		
DP5R3	200-475	(~86.3 %) The decomposition of DGEBA and non-aromatic part of PEI	8.3	2.63
	475-675	(~5.4 %) The decomposition of aromatic part of PEI		
DP25R3	200-475	(~76.8 %) The decomposition of DGEBA and non-aromatic part of PEI	11.0	2.83
	475-675	(~12.2 %) The decomposition of aromatic part of PEI		
DP30R3	200-475	(~77.9 %) The decomposition of DGEBA and non-aromatic part of PEI	10.1	2.80
	475-675	(~12 %) The decomposition of aromatic part of PEI		

The thermal and thermomechanical properties of the nanocomposites were analyzed using the DSC and DMA. The effects of selective localization of nanofillers in the nanocomposites on physical properties were studied.

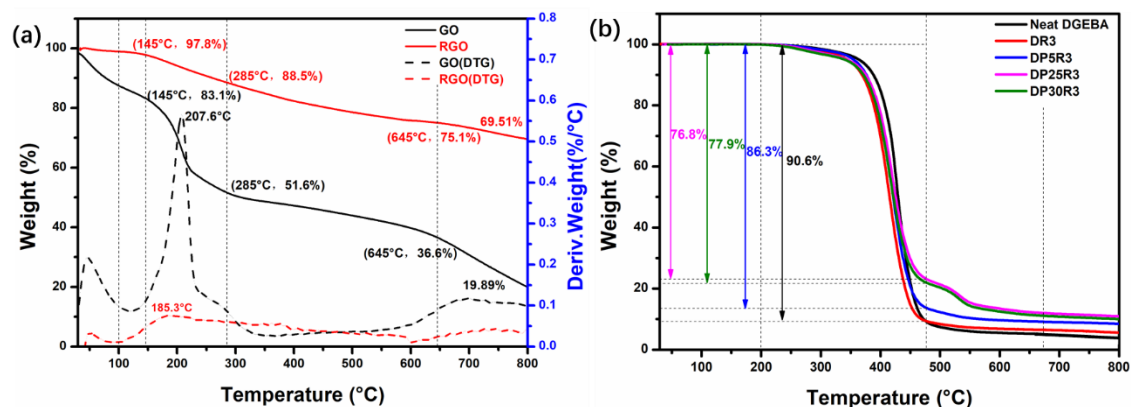


Figure 4.10. The TGA spectra of (a) GO and RGO, and (b) neat DGEBA, DR3, DP5R3, DP25R3, and DP30R3 under N₂ atmosphere.

The DSC analyses provide heat flow as a function of temperature. Figure 4.11a and 4.11b show the effect of RGO content on the thermal properties of nanocomposites DR_{n2} and DP30R_{n2}. It indicates that the T_g increases with increasing RGO content. The value of T_g increases from 93.3 °C for neat DGEBA to 97.2 °C for DR3, and to 110.9 °C for DP30R3. The increased T_g of DR3 is due to inhibition of the motion of DGEBA segments. For DP30R3, the change in internal energy of the nanocomposite due to the thermoplastic polymer PEI and nanofiller RGO is primarily responsible for the improved T_g [19]. In addition, the value of T_g for PEI is nearly 217 °C, which is much higher than that of DGEBA. Continuous PEI ligaments in the inversion phase structure will restrict the movement of DGEBA chains at elevated temperatures, which improves the T_g . The values of T_g are summarized in Table 4.5. Further, some PEI dissolves in DGEBA, leading to the higher T_g . These improvements in T_g are further confirmed by DMA.

Table 4.5. The glass transition temperature T_g (taken as the intersection of the extrapolation of baseline with the extrapolation of the inflexion) of samples.

Materials	Glass transition temperature T_g (°C)
DR1	94.0
DR1.5	95.1
DR2	95.6
DR2.5	96.7
DR3	97.2
DP30R1	95.7
DP30R1.5	97.3
DP30R2	103.6
DP30R2.5	105.1
DP30R3	110.9

DMA provides phase angle and deformation data (for calculation of storage modulus and $\tan \delta$) by applying stress or strain to specimens and analyzing the response. DMA can also reveal information about the viscoelastic behavior and thermomechanical properties of the nanocomposites. Compared to DP_{n1} polyblends and DR_{n2} nanocomposites, DP _{n1}R _{n2} nanocomposites have a higher storage modulus at the same PEI content, as shown in Figure 4.11c, indicating that the synergistic effect of PEI and RGO provides a higher reinforcement. The highest value of E' for DP30R3 reaches 2917 MPa in the glassy region and 1366 MPa in the rubbery region, which is an overall improvement of ~15% and ~1101% in comparison with that of neat

DGEBA, and an improvement of ~10% and ~1041% over the corresponding values for DR3. The rubbery modulus increases with the addition of RGO nanofiller, indicating that the crosslinking densities of DPn_1Rn_2 nanocomposites increase with RGO nanofiller content. The values of storage modulus and $\tan \delta$ are summarized in Table 4.6.

Table 4.6. The storage modulus and T_g of various samples.

Samples	Glassy modulus E' (MPa)	Rubbery modulus (MPa)	Glass transition temperature (°C)	
			T_{g1}	T_{g2}
Neat DGEBA	2532	11	116.1	
DR3	2650	12	117.1	
DP25	2666	79	125.6	193.6
DP25R3	2686	37	127.5	190.1
DP30	2687	75	121.1	186.5
DP30R3	2917	136	126.2	201.2

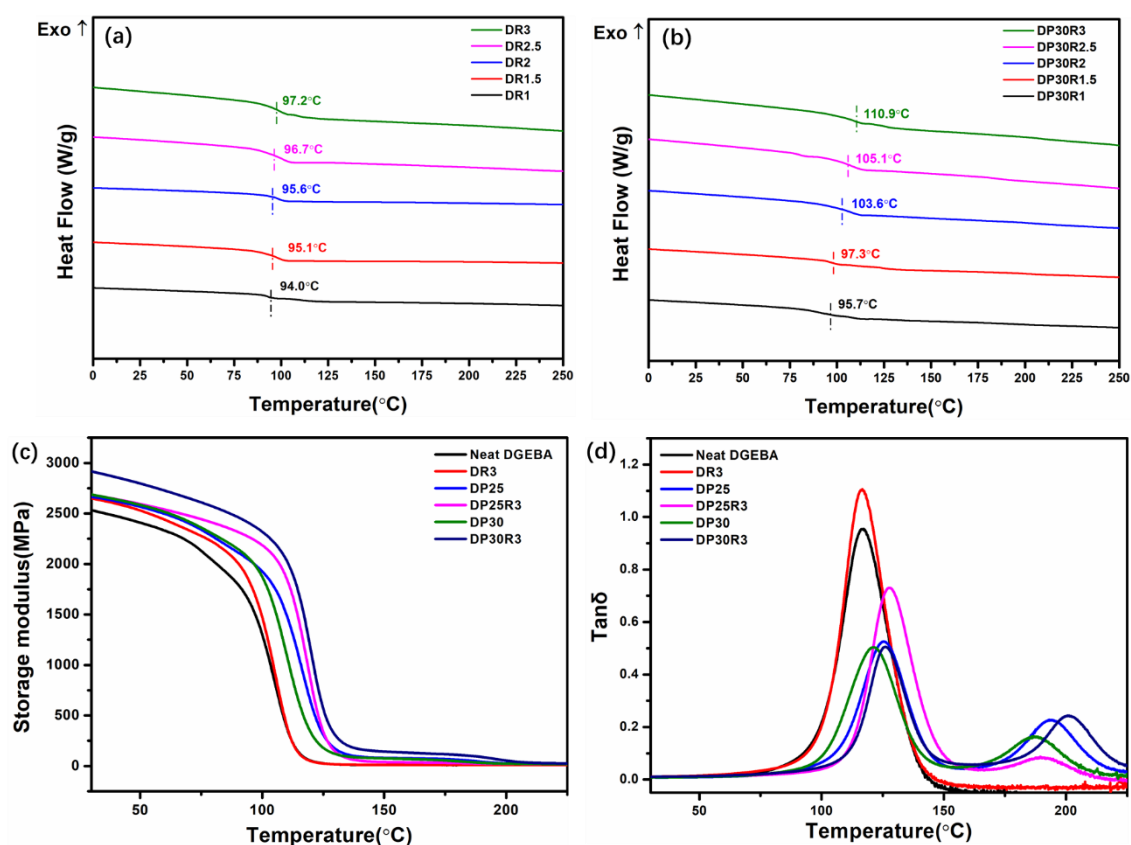


Figure 4.11. The DSC curves of (a) DRn_2 and (b) $DP30Rn_2$. The DMA measurements of (c) storage modulus and (d) $\tan \delta$ of the nanocomposites as a function of temperature.

A plot of $\tan \delta$ versus temperature for DPn_1 , DRn_2 , and DPn_1Rn_2 nanocomposites is shown in Figure 4.11d. Unlike the results of DSC, both DPn_1 and DPn_1Rn_2 show two transition peaks associated with the T_g of the DGEBA-rich phase (T_{g1}) and the PEI-rich phase (T_{g2}). The increasing

trend of T_{gI} is consistent with that from DSC measurements. In comparison with the T_g of neat DGEBA (116.1 °C), the increase in T_{gI} for DR3, DP30, and DP30R3 is 1, 5, and 10.1 °C, respectively.

4.3.7.EMI shielding properties of nanocomposites

A material that attenuates the intensity of an electromagnetic (EM) wave and inhibits its transmission is referred to as an EMI shielding material, and its abilities are quantified as a SE. Generally, there are three basic waves involved in the shielding of EM waves, reflection, absorption, and multiple reflections [61]. the SE_T of EMI shielding material can be represented as follow [62]:

$$SE_T = SE_A + SE_R + SE_M \quad (4.5)$$

where SE_A , SE_R , SE_M , and SE_T are the absorption loss, reflection loss, multi-reflection loss, and total shielding effectiveness, respectively. The SE_M of EMI shielding material can be expressed as follow:

$$SE_M = 10 \log[1 - 2 \times 10^{0.1SE_A} \cos(0.235SE_A) + 10^{-0.25SE_A}] \quad (4.6)$$

Equation (6) illustrates that SE_M is closely related to SE_A , and it can be neglected when SE_A is > 15 dB [63, 64]. Thus, two main types of loss, SE_A and SE_R , are considered in attenuating the incident electromagnetic radiation for EMI shielding material. SE_T , SE_A , and SE_R can be obtained by the scattering parameters (S_{21} and S_{11}) measured by a vector network analyzer through the equations (7-9) [65]:

$$SE_T = -10 \log|S_{21}|^2 \quad (4.7)$$

$$SE_R = -10 \log(1 - |S_{11}|^2) \quad (4.8)$$

$$SE_A = -10 \log(1 - |S_{11}|^2) \quad (4.9)$$

Here, S_{11} and S_{21} denote the response at port 1 in response to a signal at port 1 and the response at port 2 in response to a signal at port 1, respectively.

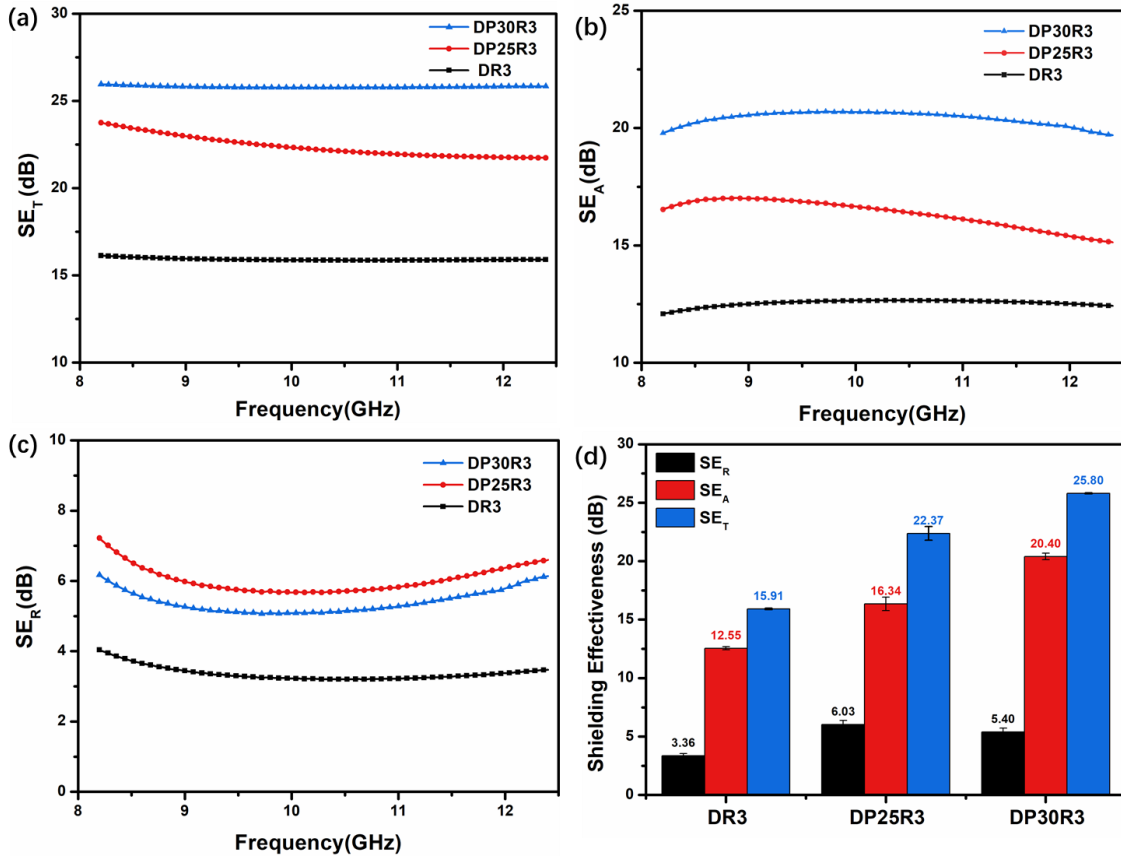


Figure 4.12. The EMI shielding effectiveness of DR3, DP25R3, and DP30R3 in the 8.2–12.4 GHz frequency range, (a) SE_T , (b) SE_A , (c) SE_R , and (d) the average SE_T , SE_A , and SE_R in the X band.

In polymer nanocomposites, EMI shielding properties can be achieved by various means, such as introducing the conducting nanofillers, using a conducting polymer matrix, or a combination of both. For polyblend shielding materials, phase structure is very important. In particular, the continuous phase can play a crucial role in developing electrically conductive networks for the attenuation of electromagnetic waves. Figure 4.12a-d shows the EMI shielding effectiveness of DR3, DP25R3, and DP30R3. The SE_T of DR3 reaches ~15.9 dB, which is lower than those commercially adopted shielding materials (i.e., 20 dB). This indicates the inability of the low nanofiller content of 3 wt.% to develop uniform networks in the DGEBA matrix. When PEI is blended with DGEBA, a significant increase in shielding properties is observed. The average SE_T of DP25R3 in the inversion phase structure reaches ~22.4 dB with the help of RGO nanofiller in the frequency range of 8.2–12.4 GHz. In this inversion phase structure, DGEBA-rich islands disperse in the thin continuous PEI-rich phase. Further, the selective localization of RGO at the interface improves the conducting losses and hence the overall shielding effectiveness.

When the PEI reaches to 30 wt.%, the average SE_T of DP30R3 reaches the highest value of 25.8 dB in the same frequency range. The improved shielding effectiveness is due to the continuous phase of the PEI-rich phase, which provides more intensive nanofiller networks at the interface. The formation of the selectively localized RGO network can be further confirmed by comparing the absorption and reflection properties of DP25R3 and DP30R3. For nanocomposite DP30R3 (Figure 4.12b-d), the shielding effectiveness due to absorption (SE_A) is about 20.4 dB, which is ~25% higher than that of nanocomposite DP25R3. In contrast, the shielding effectiveness due to reflection (SE_R) for nanocomposite DP30R3 reaches 5.4 dB, which is 10% lower than that of nanocomposite DP25R3. This result may be caused by the decreased skin depth [66] due to the increase in the electrically conducting networks in DPn_1Rn_2 nanocomposites and the high conductive losses induced by RGO.

To highlight the advantage of the CRIPS-based selective localization of conductive nanofiller for the preparation of low load nanocomposites for EMI shielding, a summary of previously reported EMI shielding composites is presented in Table 4.7. In comparison to the materials in other studies, DPn_1Rn_2 (i.e., DP30R3) ternary nanocomposites present better shielding properties with lower filler loading. Additionally, the development of a double-percolated conductive network improves the absorption properties, which ultimately facilitates in improving the shielding effectiveness.

Table 4.7. Comparison of EMI shielding performance with other composites.

Samples	Filler content (wt.%)	Thickness (mm)	Frequency (GHz)	EMI SE (dB)	[Ref]
PS/EMA/VCB	10	1	8.2-12.4	20.1	[67]
Epoxy/RGO	15	2	8.2-12.4	21	[11]
Epoxy/MWCNT	3	2.8	13-18	7.1	[68]
Epoxy/RGO/Fe ₃ O ₄	8.97	2	8.2-12.4	13.5	[69]
PEI/graphene	10	2.3	8.2-12.4	13	[70]
PMMA/Fe ₃ O ₄ @MWCNTs	7	2.5	8-12	13.1	[71]
PEI/Graphene@Fe ₃ O ₄	10	2.5	8-12	17	[72]
EP/GNPs/rGO	7.9	3	8.2-12.4	~25	[73]
epoxy/rGO/carbonyl iron	—	3	8.2-12.4	~20	[74]
DGEBA/PEI/RGO	3	2	8.2-12.4	25.9	This work

4.4.Mechanism

Conventional polymers such as DGEBA and PEI are non-conductive and transparent to radiation. However, conductive nanofillers with good electromagnetic reflection and absorption

properties will effectively enhance the shielding properties of composite materials when they are incorporated into a polymer matrix. For $DP_{n_1}R_{n_2}$ nanocomposites, not only does the combination of intrinsic electrical conductivity and absorption properties of RGO enhance EMI shielding, but also the self-assembly RGO networks via selective localization at the interface of polyblend DP_{n_1} by CRIPS mechanism contributes to EMI shielding properties (Figure 4.13). Figure 4.13a shows the CRIPS mechanism of the $DP_{n_1}R_{n_2}$ nanocomposites. DGEBA oligomers begin with linear growth of the chains and then proceed with branching reactions by increasing the temperature. When their molecular weight reaches a critical value, phase separation occurs. At the beginning of phase separation, the DGEBA did not form the crosslinking network. As the reaction continued, and the temperature crossed the T_g of DGEBA and crosslinking density reached to a critical value, the cross-linked DGEBA were formed in the DGEBA/PEI polyblend [75]. Meanwhile, the crosslinking degree of DGEBA increased [76]. For 25 wt.% and 30 wt.% PEI in the presence of 3 wt.% RGO, an inversion phase structure forms according to spinodal decomposition behavior. PEI surrounds DGEBA oligomers with RGO selectively localized at the interface. The DP_{n_1} polyblend system also helps RGO to construct a double percolation structure at much lower RGO content than has been demonstrated in other ternary polyblend nanocomposites.

Figure 4.13b shows the incident electromagnetic waves entering the $DP_{n_1}R_{n_2}$ nanocomposites divided into four wave pathways: the reflected wave, absorbed wave, transmitted wave, and waves repeatedly reflected and scattered between inner interfaces. EMI shielding includes mainly the reflection and absorption mechanisms [65]. The reflection mechanism is caused by mobile charge carriers such as electrons or holes bouncing off the shielding material, whereas the absorption mechanism is due to the absorption of radiation by electric and/or magnetic dipoles with a high dielectric constant. In these nanocomposites, the incident waves were absorbed due to destructive interference of EM waves, the closed cell network of RGO, conducting losses, and thermal losses by RGO, as shown in Figure 4.13b. These double-percolated conductive networks of RGO in $DP_{n_1}I$ polyblend form closed cell structures that produce superior absorption losses, which is consistent with the EMI shielding measurements of $DP_{n_1}R_{n_2}$ nanocomposites.

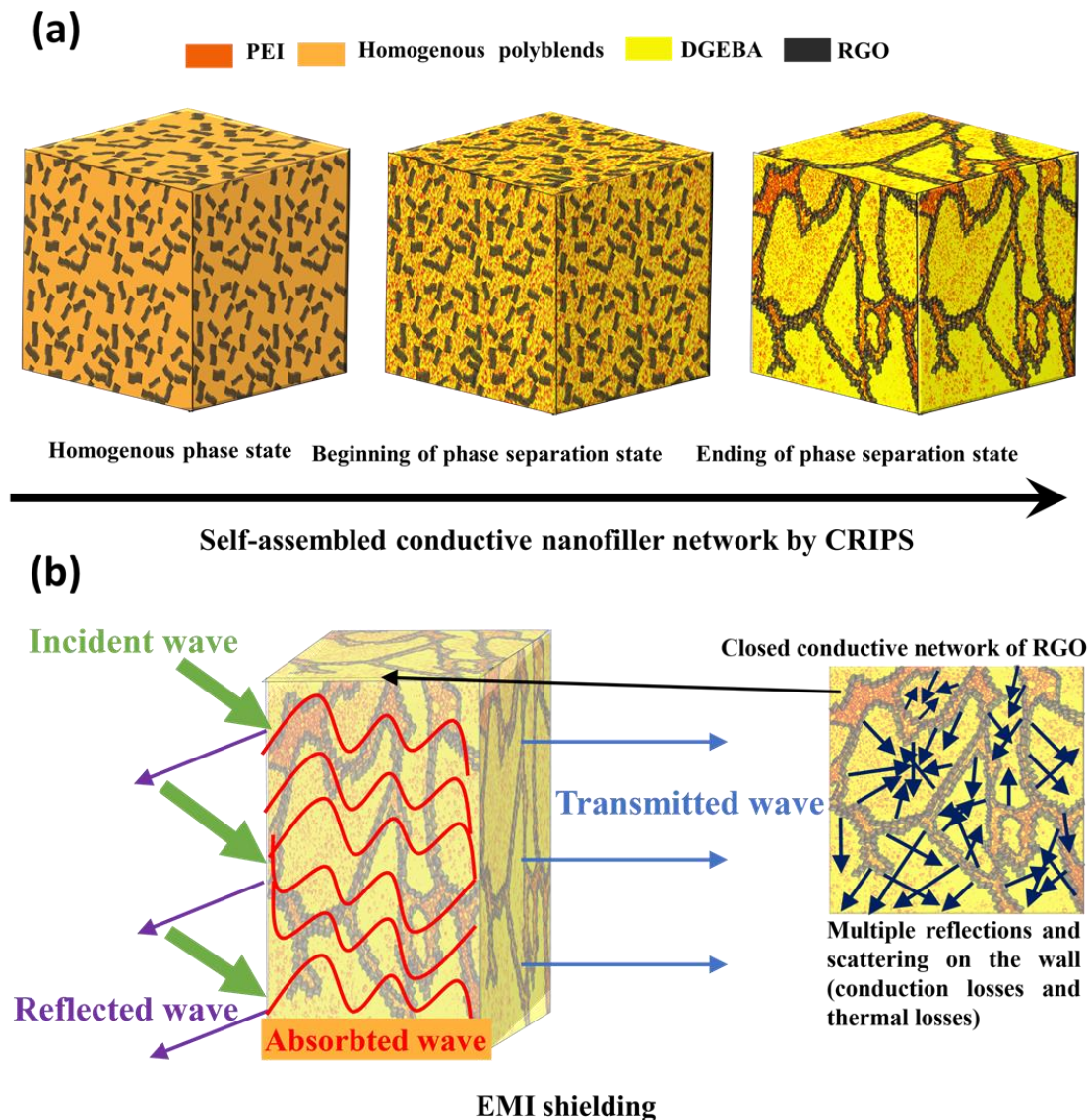


Figure 4.13. Schematic of (a) morphological evolution of double percolation, conductive $DP_{n_1}R_{n_2}$ nanocomposites and (b) the EMI shielding mechanism of $DP_{n_1}R_{n_2}$ nanocomposites.

4.5. Conclusions

In summary, DGEBA/PEI/RGO ternary nanocomposites were successfully fabricated using a solution blending followed by the casting technique. The successful reduction of pristine GO into RGO was confirmed by Raman, FT-IR, XPS, SEM, and TEM. The decomposition of DGEBA/PEI/RGO followed a CRIPS mechanism. Polyblend DP30 and nanocomposite DP30R3 formed the inversion phase structure with separated DGEBA-rich phase surrounded by the continuous PEI-rich phase. The introduction of RGO facilitated the formation of the inversion phase structure in nanocomposite DP25R3 from the co-continuous phase structure of polyblend DP25. For both nanocomposites DP30R3 and DP25R3, RGO selectively localized at the interface

between DGEBA and PEI, which was consistent with predictions from harmonic and geometric methods.

The maximum electrical conductivity of the optimized DP30R3 nanocomposite reached ~366 S/m, which is superior to that of DR3 (~ 14 S/m). This result clearly implies that only 3 wt.% of RGO is sufficient for developing a well-established conducting filler network in a polyblend nanocomposite, which would be not possible in a matrix of only DGEBA. This nanofiller network not only improved the inherent electrical properties of the polyblend but also improved the thermal and thermomechanical properties, which were confirmed by TGA, DSC, and DMA analysis. From the DSC and DMA measurements, the T_g of the DGEBA-rich phase for nanocomposites DP30R3 was found to be almost 13.7 °C (DSC) or 9 °C (DMA) higher than that of polyblend DR3, clearly suggesting the restricted motion of chain segments at the interface of the two immiscible polymers. Finally, the applicability of these electrically conducting DGEBA/PEI/RGO nanocomposites for EMI shielding was analyzed under the X band frequency range. It was found that the effective EMI shielding of DGEBA/PEI/RGO reached 25.8 dB, of which ~80% was absorbed as conduction losses, thermal losses, and destructive interference losses. Therefore, these multifunctional RGO nanocomposites with very low conductive filler loading provided a possibility in acting as effective aerospace structural materials.

References

- [1] Lu Y, Sun D, Qi X, Lei Y, Yang J, Wang Y. Achieving ultrahigh synergistic effect in enhancing conductive properties of polymer composites through constructing the hybrid network of ‘rigid’ submicron vapor grown carbon fibers and ‘reelable’ carbon nanotubes. *Composites Science and Technology*. 2020;193:108141.
- [2] Zhai Y, Wang P, Zhang X, Liu S, Li J, Chen Z, et al. Carbon dots confined in 3D polymer network: Producing robust room temperature phosphorescence with tunable lifetimes. *Chinese Chemical Letters*. 2021.
- [3] Mazaheri M, Payandehpeyman J, Khamsehchi M. A developed theoretical model for effective electrical conductivity and percolation behavior of polymer-graphene nanocomposites with various exfoliated filleted nanoplatelets. *Carbon*. 2020;169:264-75.

- [4] Samy MM, Mohamed MG, Kuo S-W. Pyrene-functionalized tetraphenylethylene polybenzoxazine for dispersing single-walled carbon nanotubes and energy storage. *Composites Science and Technology*. 2020;199:108360.
- [5] Ayub S, Guan BH, Ahmad F, Oluwatobi YA, Nisa ZU, Javed MF, et al. Graphene and Iron Reinforced Polymer Composite Electromagnetic Shielding Applications: A Review. *Polymers*. 2021;13:2580.
- [6] Koo MY, Shin HC, Suhr J, Lee GW. A Suggested Vacuum Bagging Process for the Fabrication of Single-Walled Carbon Nanotube/Epoxy Composites That Maximize Electromagnetic Interference Shielding Effectiveness. *Polymers*. 2021;13:1867.
- [7] Mohamed MG, Kuo SW. Functional Silica and Carbon Nanocomposites Based on Polybenzoxazines. *Macromolecular Chemistry and Physics*. 2019;220:1800306.
- [8] Poothanari MA, Abraham J, Kalarikkal N, Thomas S. Excellent Electromagnetic Interference Shielding and High Electrical Conductivity of Compatibilized Polycarbonate/Polypropylene Carbon Nanotube Blend Nanocomposites. *Industrial & Engineering Chemistry Research*. 2018;57:4287-97.
- [9] Zhang L, Yang B, Teng J, Lei J, Yan D, Zhong G, et al. Tunable electromagnetic interference shielding effectiveness via multilayer assembly of regenerated cellulose as a supporting substrate and carbon nanotubes/polymer as a functional layer. *Journal of Materials Chemistry C*. 2017;5:3130-8.
- [10] Zeng Z, Chen M, Jin H, Li W, Xue X, Zhou L, et al. Thin and flexible multi-walled carbon nanotube/waterborne polyurethane composites with high-performance electromagnetic interference shielding. *Carbon*. 2016;96:768-77.
- [11] Liang J, Wang Y, Huang Y, Ma Y, Liu Z, Cai J, et al. Electromagnetic interference shielding of graphene/epoxy composites. *Carbon*. 2009;47:922-5.
- [12] Wang L, Qiu H, Liang C, Song P, Han Y, Han Y, et al. Electromagnetic interference shielding MWCNT-Fe₃O₄@ Ag/epoxy nanocomposites with satisfactory thermal conductivity and high thermal stability. *Carbon*. 2019;141:506-14.
- [13] de Luna MS, Filippone G. Effects of nanoparticles on the morphology of immiscible polymer

- blends—challenges and opportunities. *European Polymer Journal*. 2016;79:198-218.
- [14] Meng Y, Sharma S, Gan W, Hur SH, Choi WM, Chung JS. Construction and Mechanism Analysis of a Self-Assembled Conductive Network in DGEBA/PEI/HRGO Nanocomposites by Controlling Filler Selective Localization. *Nanomaterials*. 2021;11:228.
- [15] Joy J, Winkler K, Joseph K, Anas S, Thomas S. Epoxy/methyl methacrylate acrylonitrile butadiene styrene (MABS) copolymer blends: Reaction-induced viscoelastic phase separation, morphology development and mechanical properties. *New Journal of Chemistry*. 2019;43:9216-25.
- [16] Heng Z, Zhang X, Chen Y, Zou H, Liang M. In-situ construction of “octopus”-like nanostructure to achieve high performance epoxy thermosets. *Chemical Engineering Journal*. 2019;360:542-52.
- [17] Pan Y, Ma C, Wan H, Tao P, Shi Q, Huang D, et al. Effect of Graphene Nanoplates on Phase Structure and Electrical Properties of Epoxy/Polyetherimide Composite. 4th 2016 International Conference on Material Science and Engineering (ICMSE 2016): Atlantis Press; 2016. p. 485-90.
- [18] Zhang J, Lin T, Cheung SC, Wang CH. The effect of carbon nanofibres on self-healing epoxy/poly (ϵ -caprolactone) blends. *Composites Science and Technology*. 2012;72:1952-9.
- [19] Jin X, Li W, Liu Y, Gan W. Self-constructing thermal conductive filler network via reaction-induced phase separation in BNNSs/epoxy/polyetherimide composites. *Composites Part A: Applied Science and Manufacturing*. 2020;130:105727.
- [20] Gao C, Zhu Z, Shen Y, Wang T, Xiang D. Efficient construction of boron nitride network in epoxy composites combining reaction-induced phase separation and three-roll milling. *Composites Part B: Engineering*. 2020;198:108232.
- [21] Tambe P, Lakshmi N, Vivek R. Polymeric blends as EMI shielding materials. *Materials for Potential EMI Shielding Applications*: Elsevier; 2020. p. 145-64.
- [22] Liu Y, He H, Tian G, Wang Y, Gao J, Wang C, et al. Morphology evolution to form double percolation polylactide/polycaprolactone/MWCNTs nanocomposites with ultralow percolation threshold and excellent EMI shielding. *Composites Science and Technology*. 2021;214:108956.
- [23] Ferrari AC. Raman spectroscopy of graphene and graphite: Disorder, electron–phonon

- coupling, doping and nonadiabatic effects. *Solid state communications*. 2007;143:47-57.
- [24] Thakur S, Karak N. Green reduction of graphene oxide by aqueous phytoextracts. *Carbon*. 2012;50:5331-9.
- [25] Cui P, Lee J, Hwang E, Lee H. One-pot reduction of graphene oxide at subzero temperatures. *Chemical Communications*. 2011;47:12370-2.
- [26] Acik M, Lee G, Mattevi C, Pirkle A, Wallace RM, Chhowalla M, et al. The role of oxygen during thermal reduction of graphene oxide studied by infrared absorption spectroscopy. *The Journal of Physical Chemistry C*. 2011;115:19761-81.
- [27] Stankovich S, Piner RD, Nguyen ST, Ruoff RS. Synthesis and exfoliation of isocyanate-treated graphene oxide nanoplatelets. *Carbon*. 2006;44:3342-7.
- [28] Yang D, Velamakanni A, Bozoklu G, Park S, Stoller M, Piner RD, et al. Chemical analysis of graphene oxide films after heat and chemical treatments by X-ray photoelectron and Micro-Raman spectroscopy. *Carbon*. 2009;47:145-52.
- [29] Cai W, Piner RD, Stadermann FJ, Park S, Shaibat MA, Ishii Y, et al. Synthesis and solid-state NMR structural characterization of ¹³C-labeled graphite oxide. *Science*. 2008;321:1815-7.
- [30] Ederer J, Janoš P, Ecorchard P, Tolasz J, Štengl V, Beneš H, et al. Determination of amino groups on functionalized graphene oxide for polyurethane nanomaterials: XPS quantitation vs. functional speciation. *RSC Advances*. 2017;7:12464-73.
- [31] Moon IK, Lee J, Ruoff RS, Lee H. Reduced graphene oxide by chemical graphitization. *Nature Communications*. 2010;1:73.
- [32] Park S, Lee K-S, Bozoklu G, Cai W, Nguyen ST, Ruoff RS. Graphene Oxide Papers Modified by Divalent Ions—Enhancing Mechanical Properties via Chemical Cross-Linking. *ACS Nano*. 2008;2:572-8.
- [33] Dang TT, Pham VH, Hur SH, Kim EJ, Kong B-S, Chung JS. Superior dispersion of highly reduced graphene oxide in N,N-dimethylformamide. *Journal of colloid and Interface Science*. 2012;376:91-6.
- [34] Tan Y, Fang L, Xiao J, Song Y, Zheng Q. Grafting of copolymers onto graphene by miniemulsion polymerization for conductive polymer composites: improved electrical

conductivity and compatibility induced by interfacial distribution of graphene. *Polymer Chemistry*. 2013;4:2939-44.

[35] TK BS, Nair AB, Abraham BT, Beegum PS, Thachil ET. Microwave exfoliated reduced graphene oxide epoxy nanocomposites for high performance applications. *Polymer*. 2014;55:3614-27.

[36] González MG, Cabanelas JC, Baselga J. Applications of FTIR on epoxy resins-identification, monitoring the curing process, phase separation and water uptake. *Infrared Spectroscopy-Materials Science, Engineering and Technology*. 2012;2:261-84.

[37] Wang X, Li W, Zhang Z, Chen K, Gan W. Selective localization of multi - walled carbon nanotubes in epoxy/polyetherimide system and properties of the conductive composites. *Journal of Applied Polymer Science*. 2019;136:47911.

[38] Zhang W, Fina A, Ferraro G, Yang R. FTIR and GCMS analysis of epoxy resin decomposition products feeding the flame during UL 94 standard flammability test. Application to the understanding of the blowing-out effect in epoxy/polyhedral silsesquioxane formulations. *Journal of analytical and applied pyrolysis*. 2018;135:271-80.

[39] AmancioFilho S, Roeder J, Nunes S, Dos Santos J, Beckmann F. Thermal degradation of polyetherimide joined by friction riveting (FricRiveting). Part I: Influence of rotation speed. *Polymer degradation and stability*. 2008;93:1529-38.

[40] Rajagopalan M, Jeon J, Oh I. Electric-stimuli-responsive bending actuator based on sulfonated polyetherimide. *Sensors and Actuators B: Chemical*. 2010;151:198-204.

[41] Ahmad MW, Dey B, ALMezeni A, Choudhury A. Chemically-reduced graphene reinforced polyetherimide nanocomposites: dielectric behavior, thermal stability and mechanical properties. *Materials Research Express*. 2019;6:115316.

[42] Göldel A, Marmur A, Kasaliwal GR, Pötschke P, Heinrich G. Shape-Dependent Localization of Carbon Nanotubes and Carbon Black in an Immiscible Polymer Blend during Melt Mixing. *Macromolecules*. 2011;44:6094-102.

[43] Li Y, Wang S, Zhang Y, Zhang Y. Carbon black-filled immiscible polypropylene/epoxy blends. *Journal of Applied Polymer Science*. 2006;99:461-71.

- [44] Plattier J, Benyahia L, Dorget M, Niepceon F, Tassin J-F. Viscosity-induced filler localisation in immiscible polymer blends. *Polymer*. 2015;59:260-9.
- [45] Wu S. Calculation of interfacial tension in polymer systems. *Journal of Polymer Science Part C: Polymer Symposia*. 1971;34:19-30.
- [46] Owens DK, Wendt R. Estimation of the surface free energy of polymers. *Journal of Applied Polymer Science*. 1969;13:1741-7.
- [47] Sumita M, Sakata K, Asai S, Miyasaka K, Nakagawa H. Dispersion of fillers and the electrical conductivity of polymer blends filled with carbon black. *Polymer bulletin*. 1991;25:265-71.
- [48] Huang J, Zhu Y, Xu L, Chen J, Jiang W, Nie X. Massive enhancement in the thermal conductivity of polymer composites by trapping graphene at the interface of a polymer blend. *Composites Science and Technology*. 2016;129:160-5.
- [49] Ma CG, Xi DY, Liu M. Epoxy resin/polyetherimide/carbon black conductive polymer composites with a double percolation structure by reaction-induced phase separation. *Journal of Composite Materials*. 2013;47:1153-60.
- [50] Liu C, Ma F, Zhang Z, Yang J, Wang Y, Zhou Z. Selective localization of organic montmorillonite in poly (l-lactide)/poly (ethylene vinyl acetate) blends and the resultant properties. *Composites Part B: Engineering*. 2017;123:1-9.
- [51] Zhou L, Tian Y, Xu P, Wei H, Li Y, Peng H-X, et al. Effect of the selective localization of carbon nanotubes and phase domain in immiscible blends on tunable microwave dielectric properties. *Composites Science and Technology*. 2021;213:108919.
- [52] Sivanjineyulu V, Behera K, Chang Y-H, Chiu F-C. Selective localization of carbon nanotube and organoclay in biodegradable poly (butylene succinate)/polylactide blend-based nanocomposites with enhanced rigidity, toughness and electrical conductivity. *Composites Part A: Applied Science and Manufacturing*. 2018;114:30-9.
- [53] Pan Y-L, Ma C-G, Wan H-M, Tao P-Y, Shi Q, Huang D-S, et al. Effect of Graphene Nanoplates on Phase Structure and Electrical Properties of Epoxy/Polyetherimide Composite. 2016.

- [54] Mani D, Vu MC, Jeong T-H, Kim J-B, Lim C-S, Lim J-H, et al. 3D structured graphene fluoride-based epoxy composites with high thermal conductivity and electrical insulation. *Composites Part A: Applied Science and Manufacturing*. 2021;149:106585.
- [55] Rajan JS. Effective use of nano-carbons in controlling the electrical conductivity of epoxy composites. *Composites Science and Technology*. 2021;202:108554.
- [56] Wan H-M, Ma C-G, Xi D-Y, Pan Y-L, Shi Q, Tao P-Y. Effect of Carbon-based Nanofillers on Electrical Properties of Epoxy/Polyetherimide Composites. *ADVANCED MATERIAL SCIENCE AND ENGINEERING AMSE2016*: World Scientific; 2016. p. 19-24.
- [57] Liu Y, Yang X, Yue L, Li W, Gan W, Chen K. Selective dispersion of silver nanowires in epoxy/polyetherimide binary composites with enhanced electrical conductivity: a study of curing kinetics and morphology. *Polymer Composites*. 2019;40:4390-401.
- [58] Park S, An J, Jung I, Piner RD, An SJ, Li X, et al. Colloidal suspensions of highly reduced graphene oxide in a wide variety of organic solvents. *Nano letters*. 2009;9:1593-7.
- [59] Villar-Rodil S, Paredes JI, Martínez-Alonso A, Tascón JM. Preparation of graphene dispersions and graphene-polymer composites in organic media. *Journal of Materials Chemistry*. 2009;19:3591-3.
- [60] Abbasi H, Antunes M, Velasco J. Graphene nanoplatelets-reinforced polyetherimide foams prepared by water vapor-induced phase separation. *Express Polymer Letters*. 2015;9:412-23.
- [61] Naeem S, Baheti V, Tunakova V, Militky J, Karthik D, Tomkova B. Development of porous and electrically conductive activated carbon web for effective EMI shielding applications. *Carbon*. 2017;111:439-47.
- [62] Lyu L, Liu J, Liu H, Liu C, Lu Y, Sun K, et al. An overview of electrically conductive polymer nanocomposites toward electromagnetic interference shielding. *Engineered Science*. 2018;2:26-42.
- [63] Panahi-Sarmad M, Noroozi M, Abrisham M, Eghbalinia S, Teimoury F, Bahramian AR, et al. A comprehensive review on carbon-based polymer nanocomposite foams as electromagnetic interference shields and piezoresistive sensors. *ACS Applied Electronic Materials*. 2020;2:2318-50.

- [64] Ravindren R, Mondal S, Nath K, Das NC. Prediction of electrical conductivity, double percolation limit and electromagnetic interference shielding effectiveness of copper nanowire filled flexible polymer blend nanocomposites. *Composites Part B: Engineering*. 2019;164:559-69.
- [65] Chung DD. Materials for electromagnetic interference shielding. *Materials Chemistry and Physics*. 2020;255:123587.
- [66] Gupta T, Singh B, Teotia S, Katyal V, Dhakate S, Mathur R. Designing of multiwalled carbon nanotubes reinforced polyurethane composites as electromagnetic interference shielding materials. *Journal of Polymer Research*. 2013;20:1-7.
- [67] Ghosh SK, Das TK, Ghosh S, Remanan S, Nath K, Das P, et al. Selective distribution of conductive carbonaceous inclusion in thermoplastic elastomer: A wet chemical approach of promoting dual percolation and inhibiting radiation pollution in X-band. *Composites Science and Technology*. 2021;210:108800.
- [68] Li J, Zhang G, Ma Z, Fan X, Fan X, Qin J, et al. Morphologies and electromagnetic interference shielding performances of microcellular epoxy/multi-wall carbon nanotube nanocomposite foams. *Composites Science and Technology*. 2016;129:70-8.
- [69] Liu Y, Lu M, Wu K, Yao S, Du X, Chen G, et al. Anisotropic thermal conductivity and electromagnetic interference shielding of epoxy nanocomposites based on magnetic driving reduced graphene oxide@ Fe₃O₄. *Composites Science and Technology*. 2019;174:1-10.
- [70] Ling J, Zhai W, Feng W, Shen B, Zhang J, Zheng WG. Facile preparation of lightweight microcellular polyetherimide/graphene composite foams for electromagnetic interference shielding. *ACS applied materials & interfaces*. 2013;5:2677-84.
- [71] Zhang H, Zhang G, Li J, Fan X, Jing Z, Li J, et al. Lightweight, multifunctional microcellular PMMA/Fe₃O₄@ MWCNTs nanocomposite foams with efficient electromagnetic interference shielding. *Composites Part A: Applied Science and Manufacturing*. 2017;100:128-38.
- [72] Shen B, Zhai W, Tao M, Ling J, Zheng W. Lightweight, multifunctional polyetherimide/graphene@ Fe₃O₄ composite foams for shielding of electromagnetic pollution. *ACS applied materials & interfaces*. 2013;5:11383-91.

- [73] Liang C, Qiu H, Han Y, Gu H, Song P, Wang L, et al. Superior electromagnetic interference shielding 3D graphene nanoplatelets/reduced graphene oxide foam/epoxy nanocomposites with high thermal conductivity. *Journal of Materials Chemistry C*. 2019;7:2725-33.
- [74] Chen Y, Zhang H-B, Huang Y, Jiang Y, Zheng W-G, Yu Z-Z. Magnetic and electrically conductive epoxy/graphene/carbonyl iron nanocomposites for efficient electromagnetic interference shielding. *Composites Science and Technology*. 2015;118:178-85.
- [75] Utracki LA. *Thermodynamics and Kinetics of Phase Separation. Interpenetrating Polymer Networks*: American Chemical Society; 1994. p. 77-123.
- [76] Yang X, Wan Y, Wang X, Fu Y, Huang Z, Xie Q. Molecular dynamics studies of the mechanical behaviors and thermal conductivity of the DGEBA/MTHPA/CNB composites. *Composites Part B: Engineering*. 2019;164:659-66.

CHAPTER 5 Construction of One-Step, Aluminium Nanowires on Hexylamine Functionalized Graphene Template Conductive Network in DGEBA/PEI Nanocomposites

5.1.Introduction

The upcoming down-scaled electronic devices increasingly call for the development of multifunctional materials possessing combined improved properties such as excellent heat dissipation, good mechanical performance, high electrical resistivity [1-3] or optimum electrical conductivity for effective shielding against electromagnetic radiations [4, 5], and high resistance to fire [6-8]. This can be achieved by the addition of nanofillers having novel functional characteristics into the polymer matrix. However, there was barely any literature that reported the high electrical conductivity of graphene/metallic nanowires as the nanofiller to reinforced epoxy matrix based nanocomposites. Therefore, the three-dimensional (3D) binary conductive network nanofiller reinforced epoxy that consists of two-dimensional (2D) hexylamine functionalized reduced graphene oxide (FRG) and one-dimensional (1D) aluminium nanowires (AlNWs) was discussed in this chapter.

In this chapter, the research focused on introducing a facile technique to synthesize catalysts-free single-crystal AlNWs on FRG substrate to construct 3D binary conductive networks via a high temperature treatment in epoxy matrix nanocomposites.

5.2.Experimental section

5.2.1.Synthesis of RFG-AlNWs film

Micro-sized Al powder dissolved in ethanol with 2mg/mL and graphene oxide (GO) powder dissolved in DI water with 2mg/mL by sonication treatment 3h, respectively, mixing them to form a uniform GO-Al suspension. Then, GO-Al suspension was diluted to 0.75mg/mL, transferred to a filter by vacuum assistance, and flowing a 506 mg hexylamine solution in ethanol (50mL) through wet GO-Al film for 6 h, washed by flowing ethanol through the film over 1h. The FG-Al wet cake was dried at room

temperature for 12h to obtain FG-Al film that detached from the membrane naturally.

The as-obtained FG-Al film was transferred to a tube furnace under argon atmosphere and was annealed at 300 °C held 10min then increased to 1000°C with 5°C/min for 1h continuously. Finally, obtain the target product RFG-AINWs film.

5.2.2. Fabrication of DGEBA/PEI/RFG-AINWs nanocomposites

The nanocomposites with RFG-AINWs were prepared using the solvent casting technique. Initially, PEI was dissolved in CH₂Cl₂ with magnetic stirring. A homogeneous suspension of RFG-AINWs (0.4 mg/mL) in ethanol was then added into PEI solution and stirred at room temperature. Subsequently, DGEBA oligomer was added into the PEI/RGO mixture. The mixture was stirred at 90 °C for 2 h to remove most of the solvent and degassed in the vacuum oven at 120 °C for 12 h to completely remove the residual solvent. Finally, a crosslinking solution of DMBA and Me-THPA was added to the degassed polyblend (DGEBA: crosslinking solution= 1:0.8) and stirred at 110 °C. After pouring into the moulds, the polyblend was then pre-cured at 150 °C for 5 h and post-cured at 200 °C for 2 h. A schematic of the fabrication process is shown in Figure 5.1.

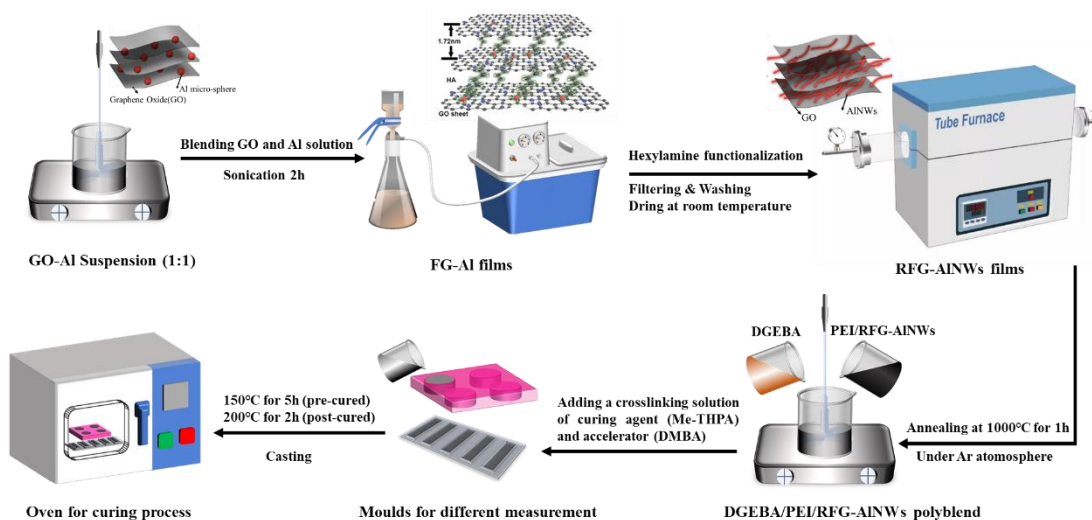


Figure 5.1. Schematic of the fabrication of DGEBA/PEI/RFG-AINWs nanocomposites.

5.2.3. Measurement and characterization

Scanning electron microscope (SEM, S-3400N, Hitachi High-Tech Co., USA) analyses were to observe the morphology of the nanofillers. Optical microscopy measurements to observe the morphology of the polyblend (OM, WT-1000GM, China) Fourier transform infrared (FT-IR) spectra were recorded using an FT-IR (Nicolet™ iS™ 5, Thermo Fisher Scientific Inc., USA) and attenuated total reflectance (ATR) accessory in the range of 4000-400 cm⁻¹ at room temperature.

The specimens were prepared in disk-shaped silicone moulds of 40 mm in diameter and 2 mm in thickness of the specimens and measured by using the four-point probe equipment (ST2263, Suzhou, China) for electrical properties measurement. The thermomechanical properties of the specimens were attained by DMA (Q800, TA Instruments Co., USA) in the single cantilever mode at a frequency of 1 Hz. The temperature ranges applied were from 30 to 180 °C for neat DGEBA and from 30 to 230 °C for other nanocomposites at a heating rate of 3 °C/min. The samples were cast in 45 mm × 10 mm × 3 mm rectangular aluminium moulds for DMA analysis. The contact angle (CA) measurements were conducted by a Phoenix 300 using the sessile drop method at room temperature with 15–17 µL of deionized water (DI), glycerol (GL), and formamide (FA), respectively. Thermogravimetric analysis (TGA, Q50, TA Instruments Co., USA) was carried out under a nitrogen atmosphere at a heating rate of 10 °C/min. Differential scanning calorimeter (DSC, Q20 V24.10, TA Instruments Co., USA) measurements were performed under a constant nitrogen flow of 50 mL/min and at a heating rate of 20 °C/min. The EMI shielding effectiveness (SE) parameters of nanocomposites were measured by a vector network analyzer (E5071C Agilent Inc., USA) in the frequency range of 8.2–12.4 GHz (X-band) at room temperature. The samples in 2 mm thickness were cut into rectangle plates of 22.9 mm × 10.2 mm to fit the waveguide sample holder.

5.3. Results and discussion

5.3.1. Morphological properties of RFG-AINWs

To characterize the dimensional evolution, scanning electron microscopy (SEM) was conducted. Viewed from the top view of the film surface, the pristine commercial micro-Al spheres that are held tightly by the hexylamine functionalized graphene oxide (FG) matrix have a typical spherical morphology with an average diameter of 1 µm, and the micro-Al spheres were dispersed well in the FG substrate were shown in the Figure 5.1a and b.

The micro-Al spheres disappeared after 1 h high temperature annealing at 1000 °C in an argon atmosphere, and the RGO film is filled by nanowires with an average length of 500 nm-1 µm in the Figure 5.1c and d.

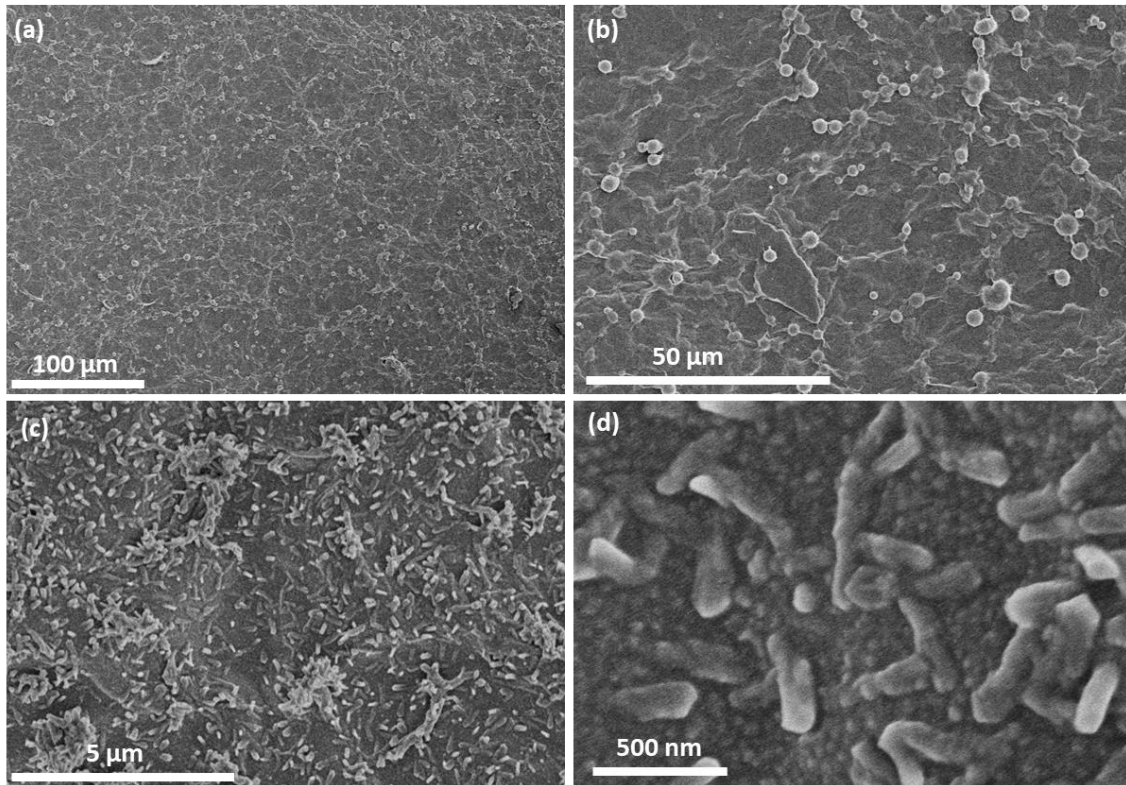


Figure 5.2 SEM micrographs of FG/Al micro-particles at (a) low and (b) high magnification, SEM micrographs of RFG-AINWs at (c) low and (d) high magnification.

The evolution of nanofiller is also conducted by optical microscopy (OM) measurements. There was a clear difference in the morphological structure between GO, FG-Al, and RFG-AINWs based on their OM images. In comparison, the morphology of GO shows rough surface with many wrinkles and ripples in the Figure 5.3a, FG-Al exhibits many bright Al-like particles dispersed on the GO substrate randomly in the Figure 5.3b, and the bright Al-like particles disappeared shows in Figure 5.3c that consisted with the result of SEM.

The dark area represents the RFG-AINWs sheets. The bright region represents the DGEBA matrix in Figure 5.3d, it shows a clear dispersion of RFG-AINWs in the DGEBA matrix.

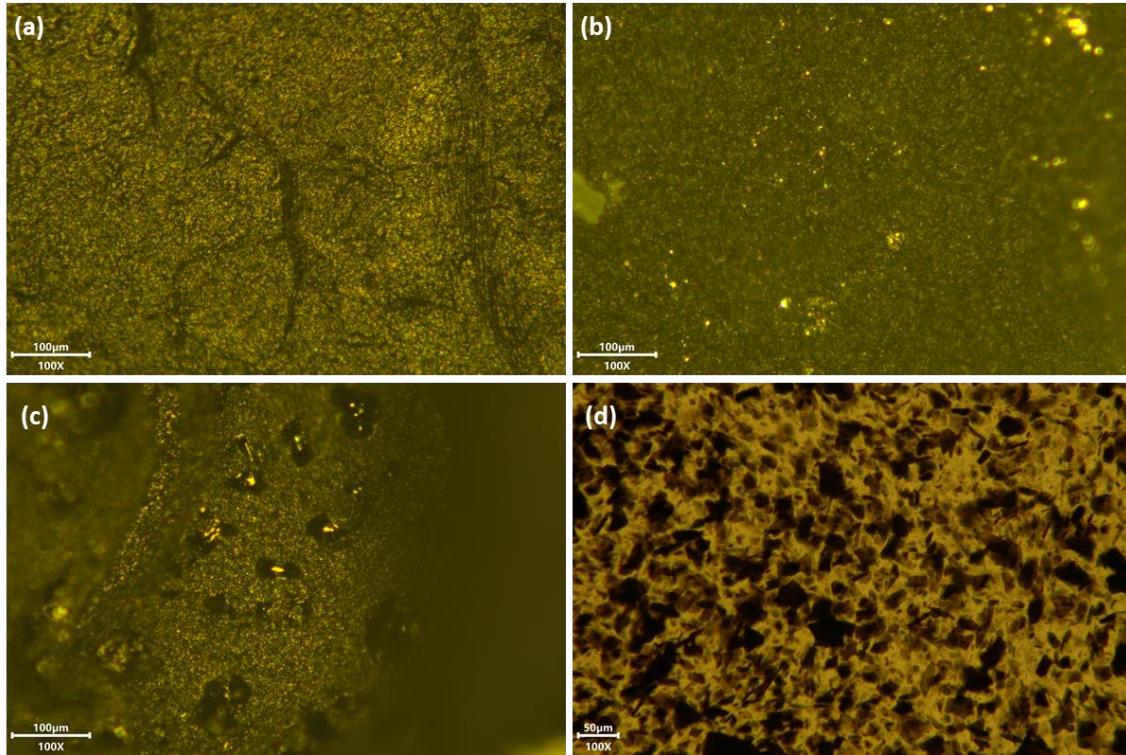


Figure 5.3. OM micrographs of (a) GO, (b) FG-Al (c) RFG-AINWs, and (d) DGEBA/RFG-AINWs.

5.3.2. Physical properties of RFG-AINWs

To characterize the functional groups of nanofiller evolution during high temperature treatment, Fourier transform infrared spectroscopy (FT-IR). Figure 5.4 shows the FT-IR spectrum of pure GO, which exhibits a broad peak for -OH stretching around 3298 cm^{-1} due to the presence of a large number of carboxyl (-COOH) and hydroxyl (-OH) groups. The other peaks of GO typically appeared at 1726 , 1618 , 1375 and 1072 cm^{-1} , corresponding to the presence of carboxyl, C=C , C-O-C , and C-O , respectively [9, 10]. In the case of RFG-AINWs, the new peaks at 1588 cm^{-1} (N-H stretching vibration) indicated the formation of -C-NH-C- bonds due to the reaction between the epoxide group of GO and the amine group of hexylamine [10, 11]. The -C=O stretching vibration at 1753 cm^{-1} of GO completely disappeared in RFG-AINWs by comparing with FG-AINWs. In comparison, the O-H stretching of GO appeared at 3398 cm^{-1} and the N-H stretching of FG-Al for hexylamine appeared at 1588 cm^{-1} , the RFG-AINWs showed a broad peak around 3350 cm^{-1} . This was attributed to the hydrogen bonding between N-H and O-H groups in RFG-AINWs.

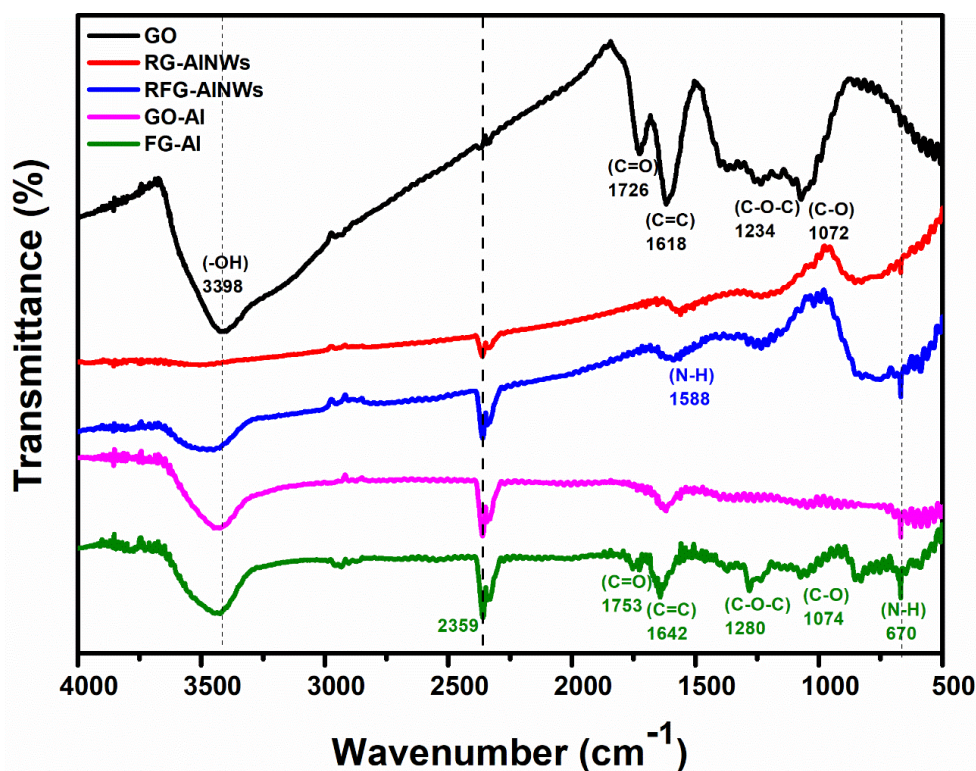


Figure 5.4. FT-IR spectra of samples

In comparison, the -OH stretching vibration at 3410 cm^{-1} of GO-AI completely disappeared in RG-AINWs due to the thermal reduction of GO. The uniform dispersion of nanofiller in the DGEBA/PEI polyblend strongly depends on the interfacial interactions. A strong interaction between RFG-AINWs and DGEBA/PEI is expected due to the presence of polar groups in the DGEBA and PEI repeat unit and the remnant oxygenated and secondary amine groups of RFG-AINWs.

5.4.Future work

The electrical, thermal, thermomechanical, and EMI shielding properties of RFG-AINWs and its nanocomposites, as well as the selective localization of hybrid RFG-AINWs nanofiller in the DGEBA/PEI will be discussed. Meanwhile, the mechanism of the construction of 3D RFG-AINWs nanofiller in DGEBA/PEI polyblend also will be discussed.

References

[1] Shtein M, Nadiv R, Buzaglo M, Regev O. Graphene-Based Hybrid Composites for Efficient Thermal Management of Electronic Devices. *ACS applied materials & interfaces*. 2015;7:23725-

30.

- [2] Cui W, Du F, Zhao J, Zhang W, Yang Y, Xie X, et al. Improving thermal conductivity while retaining high electrical resistivity of epoxy composites by incorporating silica-coated multi-walled carbon nanotubes. *Carbon*. 2011;49:495-500.
- [3] He J, Wang H, Su Z, Guo Y, Tian X, Qu Q, et al. Thermal conductivity and electrical insulation of epoxy composites with graphene-SiC nanowires and BaTiO₃. *Composites Part A: Applied Science and Manufacturing*. 2019;117:287-98.
- [4] Liang L, Xu P, Wang Y, Shang Y, Ma J, Su F, et al. Flexible polyvinylidene fluoride film with alternating oriented graphene/Ni nanochains for electromagnetic interference shielding and thermal management. *Chemical Engineering Journal*. 2020;395:125209.
- [5] Wang L, Qiu H, Liang C, Song P, Han Y, Han Y, et al. Electromagnetic interference shielding MWCNT-Fe₃O₄@ Ag/epoxy nanocomposites with satisfactory thermal conductivity and high thermal stability. *Carbon*. 2019;141:506-14.
- [6] Feng Y, Han G, Wang B, Zhou X, Ma J, Ye Y, et al. Multiple synergistic effects of graphene-based hybrid and hexagonal boron nitride in enhancing thermal conductivity and flame retardancy of epoxy. *Chemical Engineering Journal*. 2020;379:122402.
- [7] Feng Y, Hu J, Xue Y, He C, Zhou X, Xie X, et al. Simultaneous improvement in the flame resistance and thermal conductivity of epoxy/Al₂O₃ composites by incorporating polymeric flame retardant-functionalized graphene. *Journal of Materials Chemistry A*. 2017;5:13544-56.
- [8] Feng Y, Li X, Zhao X, Ye Y, Zhou X, Liu H, et al. Synergetic improvement in thermal conductivity and flame retardancy of epoxy/silver nanowires composites by incorporating “branch-like” flame-retardant functionalized graphene. *ACS applied materials & interfaces*. 2018;10:21628-41.
- [9] Nair R, Wu H, Jayaram P, Grigorieva I, Geim A. Unimpeded permeation of water through helium-leak-tight graphene-based membranes. *Science*. 2012;335:442-4.
- [10] Roy S, Tang X, Das T, Zhang L, Li Y, Ting S, et al. Enhanced molecular level dispersion and interface bonding at low loading of modified graphene oxide to fabricate super nylon 12 composites. *ACS applied materials & interfaces*. 2015;7:3142-51.

[11] Yang X, Mei T, Yang J, Zhang C, Lv M, Wang X. Synthesis and characterization of alkylamine-functionalized graphene for polyolefin-based nanocomposites. *Applied Surface Science*. 2014;305:725-31.

Summary and Future Work

In this dissertation, the multifunctional applications of graphene based network (HRGO, RGO, RFG-AlNWs) nanofillers in DGEBA/PEI polymer nanocomposites, such as electrical conductivity and electromagnetic interference (EMI) shielding, were investigated.

In chapter 2, the relationship and role of graphene based nanofiller in the DGEBA/PEI polyblend and their selective localization properties in the DGEBA/PEI, the influence of interfacial tension between nanofiller and DGEBA/PEI polyblend were concluded.

In chapter 3, optimizing and analysis of graphene based network in different content of DGEBA/PEI polyblends that a three-dimensional double-percolation network of a DGEBA/PEI/HRGO ternary system using a low content of 0.5 wt.% HRGO with the assistance of CRIPS. The results confirmed our prediction that a unique ternary nanocomposite can be fabricated by controlling the location of the conductive filler HRGO at the interface. Furthermore, the electrical conductivity of polyblends increased by almost 16 orders of magnitude at a low content of 0.5 wt.% HRGO. The dynamic mechanical analyses demonstrated that the storage modulus was continuously enhanced by increasing PEI content and was enhanced by 15.4% with the addition of 0.5 wt.% HRGO. The glass transition temperature (T_g) also increased with the addition of PEI.

In chapter 4, enhanced EMI shielding and electrical conductivity properties in DGEBA/PEI/RGO ternary system based on the optimal content of DGEBA/PEI from chapter 3. Polyblend DP30 and nanocomposite DP30R3 formed the inversion phase structure with separated DGEBA-rich phase surrounded by the continuous PEI-rich phase. The introduction of RGO facilitated the formation of the inversion phase structure in nanocomposite DP25R3 from the co-continuous phase structure of polyblend DP25. For both nanocomposites DP30R3 and DP25R3, RGO selectively localized at the interface between DGEBA and PEI, which was consistent with predictions from harmonic and geometric methods. The maximum electrical conductivity of the optimized DP30R3 nanocomposite reached ~366 S/m, which is superior to that of DR3 (~ 14 S/m). This result clearly implies that only 3 wt.% of RGO is sufficient for developing a well-established conducting filler network in a polyblend nanocomposite, which would be not possible

in a matrix of only DGEBA. This nanofiller network not only improved the inherent electrical properties of the polyblend but also improved the thermal and thermomechanical properties, which were confirmed by TGA, DSC, and DMA analysis. From the DSC and DMA measurements, the T_g of the DGEBA-rich phase for nanocomposites DP30R3 was found to be almost 13.7 °C (DSC) or 9 °C (DMA) higher than that of polyblend DR3, clearly suggesting the restricted motion of chain segments at the interface of the two immiscible polymers. Finally, the applicability of these electrically conducting DGEBA/PEI/RGO nanocomposites for EMI shielding was analyzed under the X band frequency range. It was found that the effective EMI shielding of DGEBA/PEI/RGO reached 25.8 dB, of which ~80% was absorbed as conduction losses, thermal losses, and destructive interference losses.

In chapter 5, a facile technique to synthesize catalysts-free single-crystal AlNWs on FRG substrate to construct 3D hybrid conductive network nanofiller via a high temperature treatment successfully. This RFG-AlNWs nanofiller exhibit processable compatibility in the DGEBA/PEI polyblend that plays a excellent role as a structure-optimized conductive nanofiller in DGEBA/PEI system and it might further construct a multifunctional DGEBA/PEI/RFG-AlNWs with low percolation threshold nanocomposites by utilizing its selective localization in DGEBA/PEI.

Overall, most polymers are electrically insulating in nature, thus typically require highly conducting fillers to qualify as conducting polymer composites (CPCs). A simple self-assembly processing technology to incorporate graphene based network (HRGO, RGO, and RFG-AlNWs) nanofillers in DGEBA/PEI polymer nanocomposites and how selective localization optimized their conductive network structures in the DGEBA/PEI polyblend were explored. By tailoring interactions of DGEBA/PEI and graphene based nanofillers both thermodynamically and kinetically, the selective localization of nanofillers in polyblends and at the interface of co-continuous polyblends can enhance the electrical conductivity at a low percolation threshold. Furthermore, these multifunctional nanocomposites with low nanofiller loading showed balanced electrical, thermomechanical, and EMI shielding properties. It provided a possibility in acting as effective electronic devices, microelectronics, and aerospace structural materials.

LIST OF PUBLICATIONS

- [1] **Meng Y**, Sharma S, Chung JS, Gan W, Hur SH, Choi WM. Enhanced Electromagnetic Interference Shielding Properties of Immiscible Polyblends with Selective Localization of Reduced Graphene Oxide Networks. *Polymers*. 2022;14.
- [2] **Meng Y**, Sharma S, Gan W, Hur SH, Choi WM, Chung JS. Construction and Mechanism Analysis of a Self-Assembled Conductive Network in DGEBA/PEI/HRGO Nanocomposites by Controlling Filler Selective Localization. *Nanomaterials*. 2021;11.
- [3] **Meng Y**, Gan W, Chung JS. Construction of One-Step, Aluminium Nanowires on Hexylamine Functionalized Graphene Template Conductive Network in DGEBA/PEI Nanocomposites. (Manuscript under preparation).